공학석사 학위논문

Effect of Process Parameters on Mechanical and Corrosion Properties of Twin-roll Cast Mg-2Y-1Zn Magnesium Alloy

공정변수에 따른 쌍롤박판주조 Mg-2Y-1Zn 마그네슘 합금의 기계적 및 부식 특성 평가

2019년 8월

서울대학교 대학원

재료공학부

윤 태 현

Effect of Process Parameters on Mechanical Properties and Corrosion Properties of Twin-roll cast Mg-2Y-1Zn Magnesium Alloy

지도교수 신 광 선

이 논문을 공학석사 학위논문으로 제출함

2019년 8월

서울대학교 대학원

재료공학부

윤 태 현

윤태현 의 석사 학위논문을 인준함

2019년 8월

위 원 장 홍 성 현 (인)

부위원장 신 광 선 (인)

위 원 정 인 호 (인)

ABSTRACT

Magnesium and its alloys have gained utmost attention as potential lightweight structural materials owing to their low density. However, the application of magnesium alloys is still limited by their low strength and poor corrosion resistance compared to aluminum alloys. Recently, Mg-RE-Zn alloys have shown good mechanical and corrosion resistance by forming long period stacking ordered (LPSO) phase. In the present study, Mg-2Y-1Zn (at. %) alloy was cast by horizontal twin-roll casting (TRC) process. The cast strips were processed through hot-rolling and analyzed for their mechanical properties and degradation behavior. The tensile behavior of the alloy showed improved mechanical property with higher preheating temperatures. Electrochemical and immersion tests indicated that the corrosion resistance was enhanced by higher preheating and annealing temperatures. The SKPM measurement revealed that the LPSO phase acts as a micro cathode to form galvanic couple with the α-Mg which dominated the corrosion mechanism. The alloy showed its unique microstructure when solution heat-treated and the corrosion resistance was greatly improved by forming dense surface film.

Keywords: Mg-Y-Zn alloy, mechanical properties, corrosion properties, LPSO, twin-roll casting

Student number: 2016-25463

Contents

List of Tables

List of Figures

Chapter 1

Introduction

In recent years, the need for research and development of lightweight material has increased in response to worldwide efforts to reduce the greenhouse gas emission. Magnesium (Mg) and its alloys are attractive materials for lightweight structural applications such as in automotive and aerospace industries owing to their low density and good specific strength. In fact, Mg alloys are the lightest structural material among commercialized metal alloys available on the market. However, application areas for magnesium alloys are still very limited due to their low absolute strength and poor corrosion resistance compared to other commercial alloys.

One way to supplement the strength of Mg alloys is to form a long-period stacking-ordered (LPSO) phase by adding rare earth (RE) elements into zinc based Mg alloys. It has been found that Mg-RE-Zn alloys exhibit excellent mechanical properties due to their unique LPSO structures. The first research on LPSO alloys was reported by Kawamura et al. [1] that Mg-2Y-1Zn (at.%) alloy processed through rapid solidification and extrusion can reach the tensile strength of 600MPa and elongation up to 5% due to the fine grains and high density of stacking faults. The excellent mechanical property and unique microstructures have drawn a considerable interest among the researchers to fully understand the formation of the LPSO phase and improve the performance of the alloys. Further studies revealed that the LPSO phases are not restricted to the Mg-Y-Zn system, but also can be found in Mg-RE-X system where RE=Y, Gd, Dy, Ho, Er, Tb or Tm and X=Zn, Cu or Ni. In

addition, the formation of LPSO phase was reported in the alloys prepared by conventional ingot casting and the alloys with subsequent thermo-mechanical processes such as extrusion, hot-rolling, and ECAP were proven to have excellent mechanical properties. These alloys have also shown to retain a reasonable strength even at elevated temperatures compared to other conventional Mg alloys such as AZ31 which makes the alloys promising candidates for future structural materials for automotive and aviation industries.

Nevertheless, Mg alloys in general are susceptible to degradation due to high electrochemical reactivity of Mg and the poor corrosion resistance is another limitation that hinders broad application of Mg alloys. The degradation behavior depends on the amount, composition and distribution of the phases within the alloys. RE elements in general are reported to have beneficial effects on corrosion resistance of Mg alloys when added up to certain amounts. However, majority of research on Mg-RE-X alloys has been focused on their mechanical properties by different processing route and the corrosion properties of these alloys have been rarely reported.

Furthermore, a development of more industry favorable casting routine is required for industrial applications of Mg-RE-Zn alloys. Twin roll casting (TRC) is one of the promising methods to mass produce Mg-alloy sheets. TRC process greatly reduces time and efforts of repeated heating and rolling procedure required for a sheet production from direct chill (DC) slab, as TRC process is capable of producing thin magnesium strips by feeding molten magnesium directly into a pair of cooling rolls. This characteristic enables high productivity of magnesium sheets and saves both cost and energy that are required by metal industries.

The primary purpose of current study is to investigate the effect of TRC casting parameter on the quality and properties of Mg-2Y-1Zn (at.%) strips. For this objective, Mg-2Y-1Zn alloy was cast by laboratory scale twin-roll caster with different casting speeds. A secondary aim is to further hot-roll the strips and analyze the effects of hot-rolling parameters on mechanical and corrosion properties of the TRC cast Mg-2Y-1Zn alloy.

Chapter 2

Background and Objective

2.1 Twin-roll casting

Twin-roll casting (TRC) is a relatively new concept of producing metal sheets which came into practice in the early 1950's for the production of aluminum alloys [2].The capability of producing thin metal strips directly from molten metals has attracted metal industries and there has been continuous research on this casting method in attempt to produce near-net-shape metal strips at low cost and with high efficiency. Figure 2.1 shows schematic diagram of conventional slab casting process and twin-roll casting process. It can be seen that twin-roll casting requires less processing steps compared to slab casting process which makes TRC more cost and energy efficient process. Also, rapid solidification rate of TRC process allows high casting speed and thus high productivity compared to conventional ingot/slab casting. However, TRC is a rather complex process that incorporates both solidification and deformation during the casting. The strip quality is significantly affected by process variables such as melt temperature, roll rotation (casting) speed, and roll separation force. The combination of these variables must be carefully considered depending on the alloy system, as an unfavorable solidification behavior leads to surface and internal defects such as cracks and centerline segregation. These defects affect the performance of the strip and also make the post cast processing and uses of the product difficult.

Due to the arising demand for light weight material from automotive industry, production of Mg alloys by TRC has been attempted in many parts of the

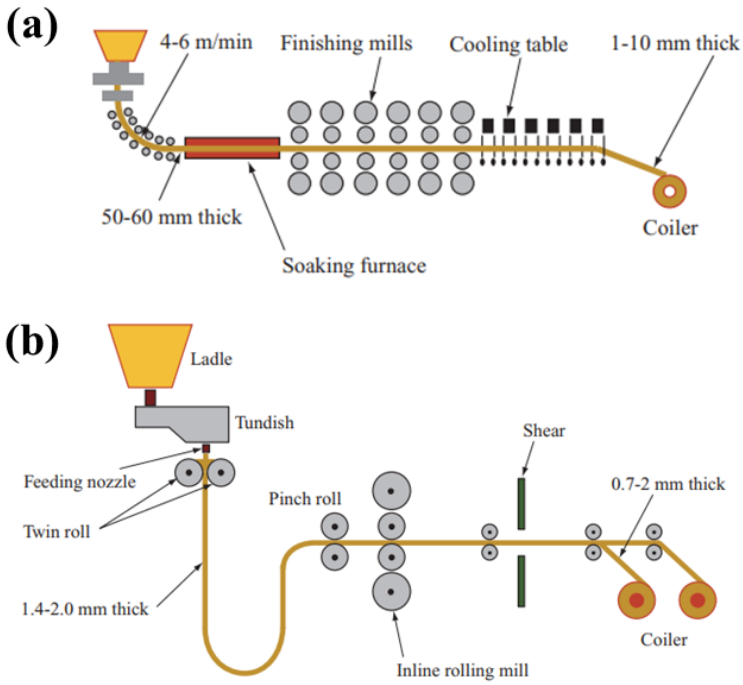

Figure 2. 1 Schematic diagram of (a) slab caster and (b) twin-roll caster [2]

world. A few Mg alloys have actually been commercialized but the market response has been rather mediocre as it lacks clear advantage over the aluminum alloys that has been successfully adopted for several decades. The main disadvantages of Mg alloys include their mechanical properties, formability, and corrosion resistance. There are some alloys that have resolved these problems and Mg-2Y-1Zn alloy is one of them. In most studies, gravity casting has been used for material preparation, followed by extrusion and ECAP for maximum mechanical properties. To the best of our knowledge, this is the first time an LPSO type alloy is processed through twin-roll casting. In that regard, one of the main focus of this study is to assess the effect of casting parameters on cast strip quality and performance; and compare with the alloys prepared by ingot casting since the majority of previous works on the LPSO type alloys adopted conventional gravity casting process. For that purpose, Mg-2Y-1Zn strips were cast with different casting speed (roll rotation speed) as it is the key process variable in industries which directly influence the productivity as well as the quality of the material.

2.2 Hot-rolling of Mg alloys

Hot-rolling is a common practice conducted on metal alloys after twin-roll casting (TRC) and usually as-cast strips are fed directly to the rolling mills. Hot-rolling is performed to reduce the strip thickness into a desired level, and control the microstructure of the strips to tailor the performance of the final product. As-TRC strips often have uneven microstructure and poor mechanical properties. Hot-rolling refines the grain size and microstructure, and enhance the mechanical properties of the cast strips during the process. The final properties of the Mg alloy sheets greatly depends on the process parameters

such as initial state of the strips, preheating temperature, reduction per pass and many other parameters. Therefore, finding the optimal rolling parameters for the selected alloys is important to alter the alloys to desired dimension and mechanical properties.

The Mg-Y-Zn alloys are known to exhibit excellent mechanical properties under appropriate thermomechanical processes which are attributed to their unique LPSO structures [3]. However, most of these alloys were gravity cast and then processed through extrusion and ECAP and there are not many reports on hot-rolled properties of Mg-Y-Zn alloys. Thus, another contribution of this study is to compare the properties of twin-roll cast and hot-rolled Mg-2Y-1Zn (at. %) alloy with the previous studies and to understand the relationship between the hot-rolling parameters and the performance. For this objective, the twin-roll cast Mg-2Y-1Zn alloy was hot-rolled and annealed at different temperatures.

2.3 Degradation of Mg

Despite many desirable properties for various applications, Mg and its alloys are susceptible to environmental degradation (corrosion) due to their electrochemical nature. Mg has the lowest negative standard electrode potential among commercial metals as can be seen from Table 1, which makes it especially vulnerable to galvanic corrosion when in contact with other metals. Just like other metals, the corrosion behavior of Mg depends on the formation of a protective surface film which inhibits the chemical attack when exposed to a corrosive, environment. However, the passive film easily breaks down in case of Mg due to its loose and porous structure and only provides limited protection especially in chloride environment.

Table 1 Standard reduction potential of metals

Reaction		Standard Reduction Potential (V)
Noble	$Au^{3+} + 3e^- = Au$	1.498
	$Pt^{2+} + 2e^- = Pt$	1.118
	$Ag^+ + e^- = Ag$	0.779
	$Fe^{3+} + e^- = Fe$	0.771
	$Cu^{2+} + 2e^- = Cu$	0.342
	$Sn^{4+} + 2e^- = Sn^{2+}$	0.15
	$Pb^{2+} + 2e^- = Pb$	-0.126
	$Sn^{2+} + 2e^- = Sn$	-0.138
	$Ni^{2+} + 2e^- = Ni$	-0.25
	$Co^{2+} + 2e^- = Co$	-0.277
	$Cd^{2+} + 2e^- = Cd$	-0.403
	$Fe^{2+} + 2e^- = Fe$	-0.447
	$Cr^{3+} + 3e^- = Cr$	-0.744
	$Zn^{2+} + 2e^- = Zn$	-0.762
	$Al^{3+} + 3e^- = Al$	-1.662
	$Mg^{2+} + 2e^- = Mg$	-2.372
	$Na^+ + e^- = Na$	-2.71
Active	$K^+ + e^- = K$	-2.931

The corrosion reaction of Mg can be expressed by following equations:

$$Mg \rightarrow Mg^{2+} + 2e^{-} \quad (1)$$

$$2H^{+} + 2e^{-} \rightarrow H_2 \quad (2)$$

$$2Mg+ + 2H_2O \rightarrow 2Mg^{2+} + 2OH^{-} + 2H_2 \quad (3)$$

$$Mg^{2+}\ 2OH^{-} \rightarrow Mg(OH)_2 \quad (4)$$

$$Mg + 2H_2O \rightarrow Mg(OH)_2 + H_2 \quad (5)$$

The corrosion sequence of Mg can be broken down in to the anodic (Eq. 1) and cathodic (Eq. 2) reactions. The evolution of hydrogen is a key cathodic reaction in corrosion of Mg. Hydrogen molecules are generated by the reduction (Eq 2) reaction as well as the reaction between Mg and water (Eq. 3). The degradation process produces a degradation layer of $Mg(OH)_2$ on the surface of magnesium by the reaction between Mg^{2+} and OH^{-} (Eq.4) but the layer could be composed of other corrosion product depending on corrosion mediums. Thus, the overall reaction of Mg degradation produces $Mg(OH)_2$ and H_2 gas (Eq. 5).

The degradation of Mg is a complex process and can be affected by interaction of various factors. It is commonly understood that the corrosion properties of Mg and its alloys largely depends on their microstructure such as grain size and secondary phase distribution. Grain refinement is an effective way of tailoring the corrosion properties as well as the mechanical properties. Liu et al. studied the effect of grain size on the corrosion properties of pure Mg prepared

by different cooling rate [4]. The study showed that the corrosion resistance increased with the decrease in grain size as a result of uniform and dense film formation on the refined grains. Similar result has also been reported by Jang et al. for AZ31B Mg alloy which showed better corrosion resistance in finer microstructure [5]. On the other hand, some studies revealed that the corrosion rate increases as the grain size decreases. Song et al. reported that the pure Mg with finer grains showed deteriorative corrosion resistance after equal channel angular pressing (ECAP) [6]. Saikrishna et al. also found that the corrosion rate increases as the grain size decreases in friction stir welded AZ31 [7]. These conflicting results suggest that it is difficult to define the contribution of grain size although it does have an impact on corrosion behavior of Mg.

The corrosion properties of Mg are also greatly influenced by alloying elements. The alloying elements react with Mg and form secondary phase which could affect the degradation process. Mg is electrochemically very reactive and forms micro galvanic cell with precipitates. Therefore, the presence of secondary phase is considered to have negative effect on corrosion properties in general. In case of single element addition, Mn, Er, Ce, La and Nd are reported to improve the corrosion resistance whereas Ca, Zn, Zr and Sr could either enhance or deteriorate depending on its concentration. The addition of multiple elements and its effect on corrosion behavior is much more complex as various secondary phases may form. The volume fraction, distribution and electrochemical potential of the secondary phase and their interaction are all critical factors which affect the corrosion properties.

The corrosion properties of LPSO containing alloys also have been a great interest among the researchers as much as their mechanical properties. Similar

to other precipitates, the LPSO phases are known to affect the corrosion properties of Mg by their types, volume fraction and distribution. Zhang et al. studied the effect of LPSO phases on the corrosion properties of Mg-Y-Zn alloying containing different amount of LPSO and found the galvanic corrosion took place in the junction of LPSO and α-Mg [8]. Li et al. also reported that the LPSO phase accelerated the corrosion rate in Mg-Y-Zn system due to different localized potential between the secondary phase and the α-Mg [9]. However, most studies on corrosion behavior of the LPSO alloys were conducted for the gravity cast alloys and the degradation behavior of twin-roll cast Mg-2Y-1Zn (at .%) alloy has not been investigated so far. Thus, the corrosion properties of twin-roll cast Mg-2Y-1Zn (at. %) alloy are explored in as-cast and hot-rolled condition.

Chapter 3

Experimental procedure

3.1 Twin-roll casting

The magnesium alloy with nominal composition of Mg-2Y-1Zn was subjected to TRC process on a laboratory scale using a horizontal TRC caster shown in Fig. 3.1 (a,b). The alloy was melted in a form of pure Mg, Zn and Mg-40Y master alloy at 720-730 °C in a boron nitride coated steel crucible under a gas mixture of SF_6 and CO_2 to protect molten metals from oxidation. The melt was held at 735 ^{o}C for 20min to stabilize the melt temperature and ensure all the alloying elements were dissolved and homogenized. After complete dissolution of the elements, the melt was transferred into a calcium silicate nozzle preheated to 650 °C and then fed in to the water cooled copper-beryllium rolls (diameter=150 mm and face width=200 mm) set to a roll gap of 2 mm for casting. The water flow through the rolls was set to 11 L/min per roll. During the casting, all the casting parameters except the casting speed were set constant. The strips were cast at 2.6, 3.3, 4.0 and 4.7 m/min in each individual casting process. No lubricant was applied on the surfaces of the rolls during the casting. The rolls were fixed at one end and the other side was supported by springs to control the roll separation force. The roll separation load was initially set to 1000 kg measured by a load cell and then set to 3000 kg once the melt passed the rolls and the strips started to come out. The thickness of the cast strips were in range of approximately 2.5-4.5 mm depending on the casting speeds and the width was in range of 55-60 mm. The actual chemical composition of the cast strips were determined by ICP spectrometer and are

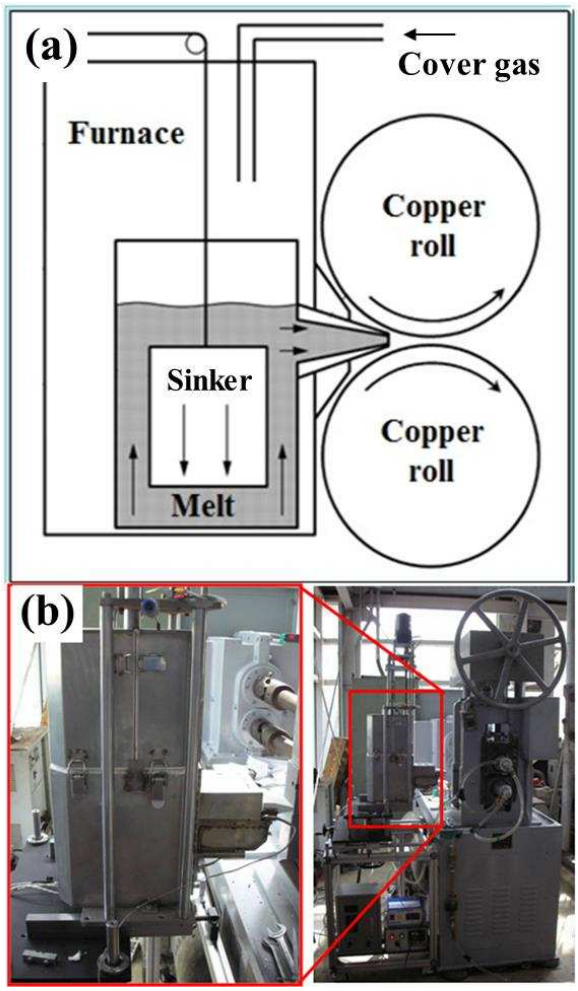

Figure 3. 1 (a) Schematic diagram of laboratory scale twin-roll caster and (b) photograph of the twin-roll caster.

listed in Table 2 with the dimensions of the strips. .

3.2 Hot-rolling of TRC strips

The cast strips were cut to 50 mm in length and homogenized at 400 °C for 24 h for more refined and uniform microstructure. A relatively low homogenization temperature was selected initially to preserve the as-TRC structure and see the effect on mechanical and corrosion properties. The homogenized strips were hot rolled at the roll temperature of 300 ^{o}C for three passes with a reduction rate of 20-30% per pass until the thickness of 1.3-1.4mm, depending on the initial thickness. The roll speed was set to 1.0 m/min and the preheating temperatures were 350, 400, 450, 500 and 550 ^{o}C (P350, P400, P450, P500, P550) respectively and the strips were reheated to the preheating temperature for 10 min between each passes. During this stage, the strips preheated to 350 ^{o}C were cracked and strips preheated to 550 ^{o}C experienced hot tearing and further processing was impossible. Other samples were put into intermediate annealing at 400 ^{o}C for 1 h and subjected to the final pass of hot rolling at each preheating temperatures using the reduction ratio of 30 %. The final thicknesses of the strips were approximately 1.0 mm. The rolled sheets were then annealed at 350, 500 and 550 ^{o}C (A350, A500, A550) for 1 h.

For the strip cast at 3.3 m/min, hot-rolling through the alternative route was also conducted, starting from a solution heat treatment of the as-cast strips at 540 ^{o}C for 24 h, followed by the furnace cooling at 0.5 ^{o}C/min. After the heat treatment, the strips followed the same hot-rolling procedure as the homogenized strips but preheated at 500 ^{o}C only. The rolled sheets were then annealed at 350 ^{o}C (A350) for 1 h.

Table 2 Chemical composition and thickness of twin-roll cast strips.

Casting speed (m/min)	Composition (wt. % / at. %)			Thickness (mm)
	Y	Zn	Mg	
2.6	6.21 / 1.81	2.51 / 0.99	Bal.	4.54
3.3	6.40 / 1.87	2.48 / 0.98	Bal.	3.62
4.0	6.37 / 1.86	2.61 / 1.04	Bal.	2.93
4.7	6.14 / 1.79	2.70 / 1.07	Bal.	2.52

3.3 Characterization of hot-rolled sheets

Microstructures of as-cast and rolled samples were observed by an optical microscope. The samples were polished to 4000 grid abrasive papers and etched with acetic-picral solution and natal solution. For better understanding of the microstructure, scanning electron microscope (SEM) equipped with energy dispersion spectroscopy (EDS) were also utilized. The phases of the alloys were also confirmed by X-ray diffractometry (XRD). Tensile tests were performed for the as-cast strips and hot-rolled sheets with a strain rate of 2×10^{-4}/sec according to the ASTM standard B557M with the loading axis being parallel to the casting and rolling direction.

The as-cast strips and hot-rolled sheets were prepared for the corrosion test by polishing up to 2000 grid abrasive paper followed by ultra-sonication in ethanol. The samples were immersed in 3.5 wt.% NaCl solution saturated with $Mg(OH)_2$ for 5-10 h at room temperature ($25\pm1^{o}C$). The samples were hung by fishing line and suspended vertically so that the entire surface get exposed to the solution. Hydrogen was collected during the immersion test with inverted funnel and the corrosion rate was determined by hydrogen evolution (P_H) and weight loss (P_W) methods after removing the corrosion products by dipping the samples into 200 g/L CrO_3 solution containing 10g/L of $AgNO_3$. Electrochemical studies were also conducted using the potentiostat. The working electrode was the samples with exposed area of 1 cm^2, platinum (Pt) and Ag/AgCl (saturated KCl) were used for counter and reference electrodes, respectively. Open circuit potential (OCP) was measured as a function of time for 30 min and potentiodynamic polarization measurement was conducted with a scan rate of 1.0 mV/s between the range of ±250 mV respect to the OCP.

Corrosion morphologies after the immersion test were also observed using optical microscope and SEM.

Chapter 4

Results and Discussion

4.1 Twin-roll casting

4.1.1 Casting of Mg-2Y-1Zn strips

Prior to twin-roll casting, thermodynamic simulation on Mg-2Y-1Zn alloy was carried out using JMatPro software to predict solidification behavior and find suitable process condition. Figure 4.1 shows predicted solidification sequence and second phase fraction according to the temperature. The Scheil (non-equilibrium) cooling mode was selected for the calculation considering a rapid solidification behavior during TRC as the diffusion in the solid phase is very limited. The simulation results show that α-Mg starts to solidify first at 628^{o}C, followed by the formation of $Mg_3Y_2Zn_3$ (W-phase) at 570^{o}C. Right after that, $Mg_{12}YZn$ (X-phase LPSO) starts to precipitate at 562^{o}C and finally $Mg_{24}Y_5$ forms at 556^{o}C. Major precipitates are $Mg_{12}YZn$, so called the X-phase LPSO, suggesting that centerline segregation of the strip would consist mostly of α-Mg and $Mg_{12}YZn$, although $Mg_{24}Y_5$ is the last solid predicted to form. Also, it is noticeable that the solidification is complete in a fairly short range of 71.1^{o}C considering the amount of alloying elements contained, as the alloy mainly consists of high melting point phases. The melt temperature was carefully selected based on our previous studies. Insufficient melt temperature leads to partial or complete clogging of feeding nozzle as the melt solidifies inside the nozzle which hinders uniform feeding of the melt. Inconsistent melt delivery and unstable contact condition between the melt and the roll surface could cause surface dent on the cast strip which affects the appearance and quality of

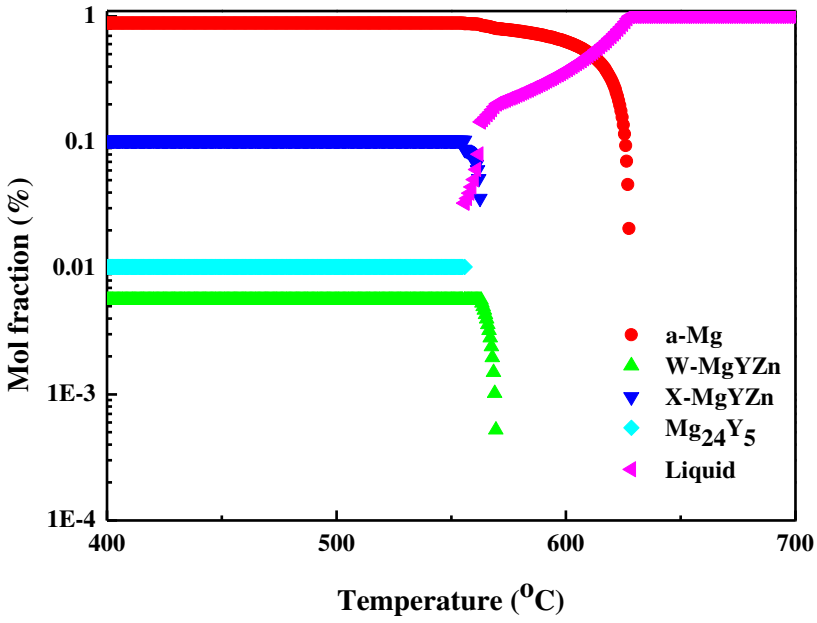

Figure 4. 1 Solidification diagram of Mg-2Y-1Zn (at. %) alloy.

the strips. On the contrary, overheated melt leads to other types of surface and internal defects such as heat-line and centerline segregation which have negative effect on strip quality and performance. To see the effect of casting speed on strip quality, other process variables were set constant in all casting trials.

4.1.2 Microstructure of cast strips

Figure 4.2 shows the surface appearance of the as-cast TRC strips cast at each casting speed from 2.6 to 4.7 m/min. The strip cast at 2.6 m/min showed continuous ripple like pattern across the transverse direction as shown in Fig 4.2 (a) which can be often seen from the strips with insufficient cooling and inhomogeneous solidification. The strip cast at 3.3 m/min had a sound surface appearance without noticeable surface defect as can be seen from Fig 4.2 (b). As the casting speed is further increased, cracks begin to appear at the edge of the strips as shown in Fig 4.2 (d). All of the cast strips had purple colored oxidation band at the edge of the strips and the band thickness decreased and became less apparent as the casting speed was increased. The cast strips had different thickness in accordance with casting speed as listed in Table 2. The thickness was inversely proportional to the casting speed and the strip cast at 2.6 m/min was the thickest with the thickness of 4.54 mm and the thinnest strip was found at the casting speed of 4.7 m/min which had the thickness of 2.52 mm. As one side of the rolls was fixed by the force of the spring, the slower roll rotation led to larger amount of melt passing between the rolls which lifted up the roll and consequently resulted in thicker strips. Similarly, the width of the strips also changed with the casting speeds and the strip cast at slower speed were wider although the change in width was not as large as the change

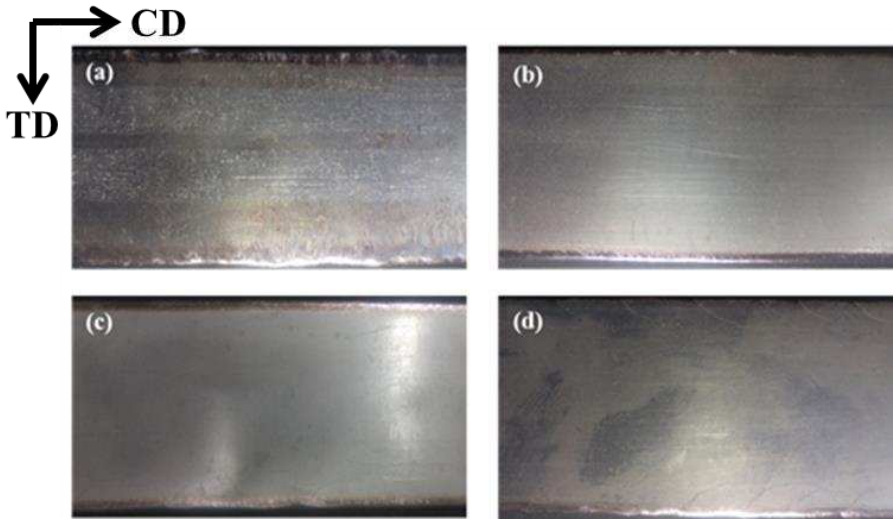

Figure 4. 2 Surface appearance of the as-cast trip; (a) 2.6 m/min, (b) 3.3 m/min, (c) 4.0 m/min and (d) 4.7 m/min.

in thickness.

Figure 4.3 depicts the dendritic structure of the as-cast strips from the transverse direction. It is apparent that centerline segregation is formed near the center of the strips at all casting speeds along the casting direction due to the large freezing range of the remaining solute enriched liquids. Also, the strips showed quite homogeneous microstructure with equiaxed dendritic structures throughout the thickness of the strips. This is most likely due to the low superheat and consequently low temperature gradient which hindered dendritic growth. Figure 4.4 shows the SEM images of as-cast strips from the transverse direction and it can be seen that the strip cast at 2.6 m/min (Fig. 4.4(a)) had a thick band of segregation layer suggesting that it had the slowest solidification rate. Other strips (Fig. 4.4 (b, c, d)) also had segregation at the center but the width and amount of segregation decreased as the casting speed was increased which also indicates the increase in cooling rate in response to the increasing casting speed. A close-up image of centerline segregation for the strip cast at 2.6 m/min is illustrated in Fig. 4.5. The segregation layer mainly consisted of two phases and the EDS results of each phases are given in Fig. 4.5 (c,d,e). The gray colored network like phase in the segregation region turned out to be X-phase LPSO ($Mg_{12}YZn$) as expected from thermodynamic simulation result. The brighter phase that spreads over the LPSO phase had more concentrations of Y and Zn as the solutes migrate to the remaining liquid during the solidification. Fig. 4.6 presents the optical micrographs of the as-cast strips at the central part taken from the normal direction. As can be seen, the surface had a unique maze like dendritic structure for all casting speeds.

The dendrite structure became finer and dense as the casting speed is increased.

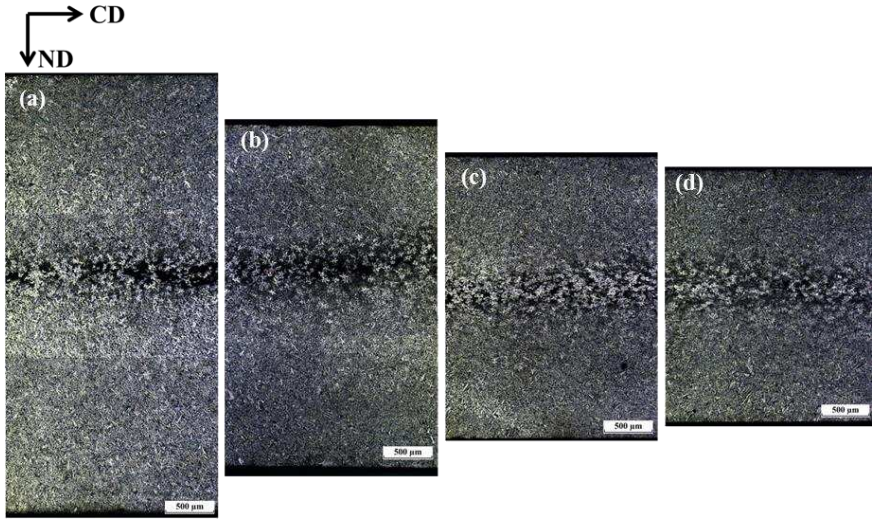

Figure 4. 3 Optical micrographs of the as-cast strips from transverse direction; (a) 2.6 m/min.

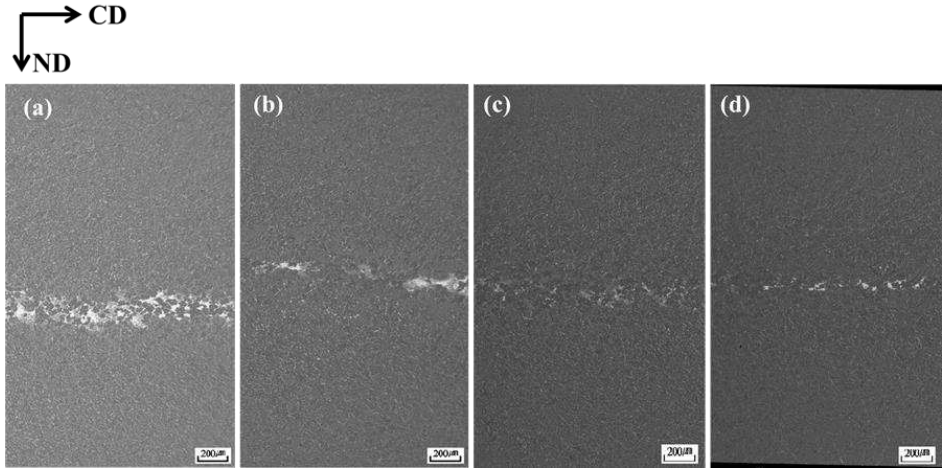

Figure 4. 4 SEM-BSE images of the as-cast strips from transverse direction; (a) 2.6 m/min, (b) 3.3 m/min, (c) 4.0 m/min and (d) 4.7 m/min.

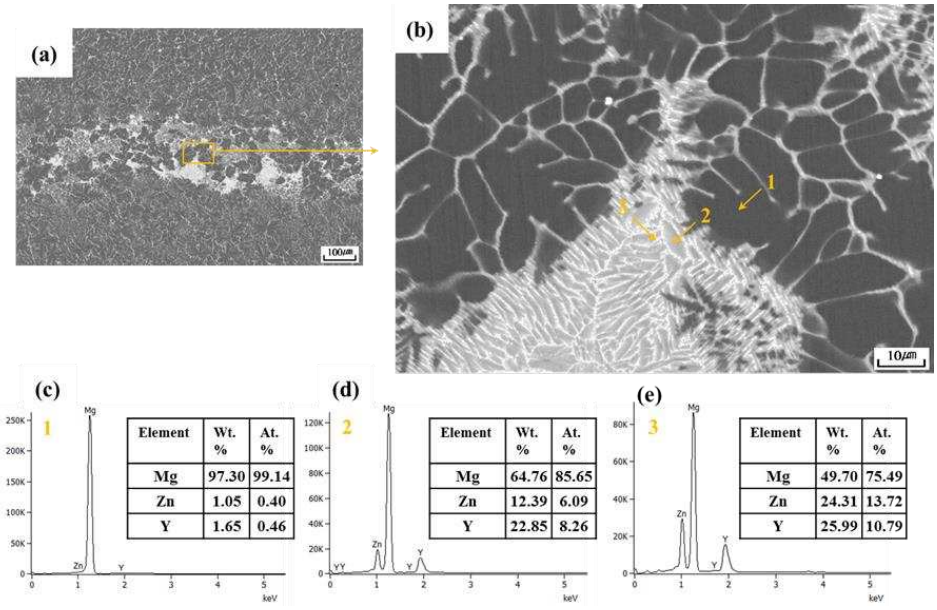

Figure 4. 5 (a, b) SEM-BSE images of center line region of the strips cast at 2.6 m/min and (c,d,e) EDS analysis.

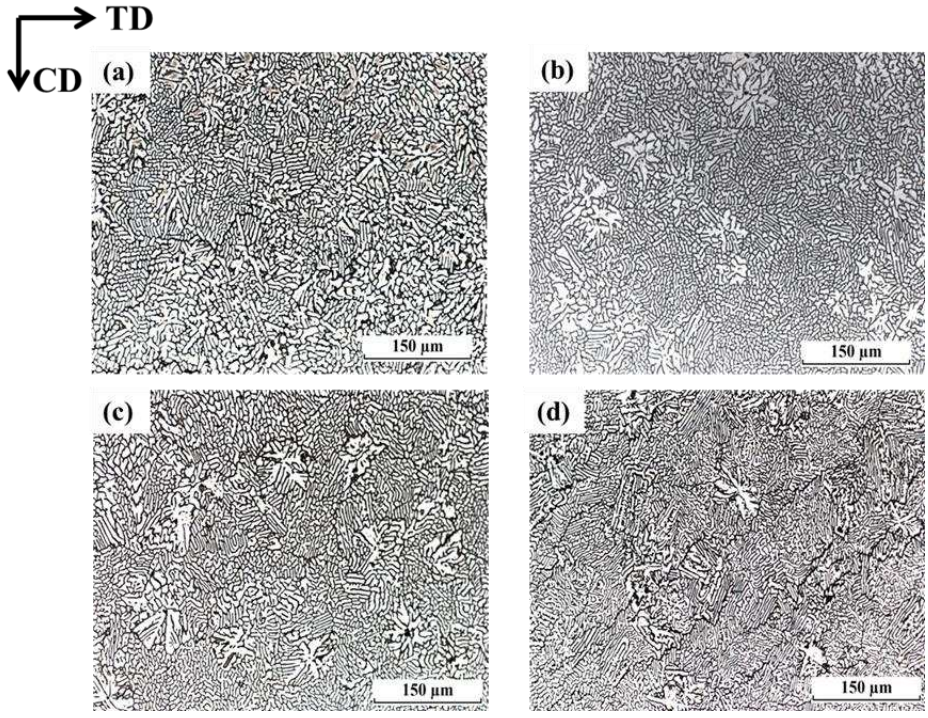

Figure 4. 6 Optical micrographs of as-cast strips from normal direction; (a) 2.6 m/min, (b) 3.3 m/min, (c) 4.0 m/min and (d) 4.7 m/min.

The dendrite structure became finer and dense as the casting speed is increased. The dendrite spacing was measured using an image analyzing software with a calibration factor of 0.35μm/pixel and the result is shown in Table 3. It was observed that the dendrite spacing of the alloy decreased with increasing casting speed indicating that the strip cast at 2.6 m/min had the slowest solidification rate. It is normally understood that slower roll rotation and longer residence time of melt between the rolls provide faster cooling. However, it seems that the reduction in strip thickness was more effective than the longer contact time of melt between the rolls in this case. Figure 4.7 shows the optical micrographs of as-cast strips from transverse direction under polarized light. All of the strips had similar microstructure in terms of grain size but there was a difference in the degree of deformation. The strip cast at 2.6 m/min had the least degree of deformation whereas the strip cast at 4.7 m/min showed the most deformed structure. It is most likely that this resulted from the difference in strip thickness and width as all the strips were cast with same roll separation force and the roll separation force and roll torque were not enough to deform the thicker and wider strips. Another possible reason is that the solidification fronts were formed further away from the nozzle in case of the thicker strips which resulted in shorter deformation region.

To observe the change in microstructure after the homogenization, optical micrographs of the as-cast strips homogenized at 400 ^{o}C taken from the transverse direction are shown in Fig. 4.8. The centerline segregation regions are still noticeable at all casting speeds. Although the segregation region area decreased compared to the as-cast state, removing the centerline segregation completely was not possible due to the high thermal stability of $Mg_{12}YZn$

Table 3 Average dendrite spacing of as-cast strips.

Casting speed (m/min)	Dendrite spacing (μm)
2.6	5.71
3.3	4.44
4.0	3.99
4.7	3.26

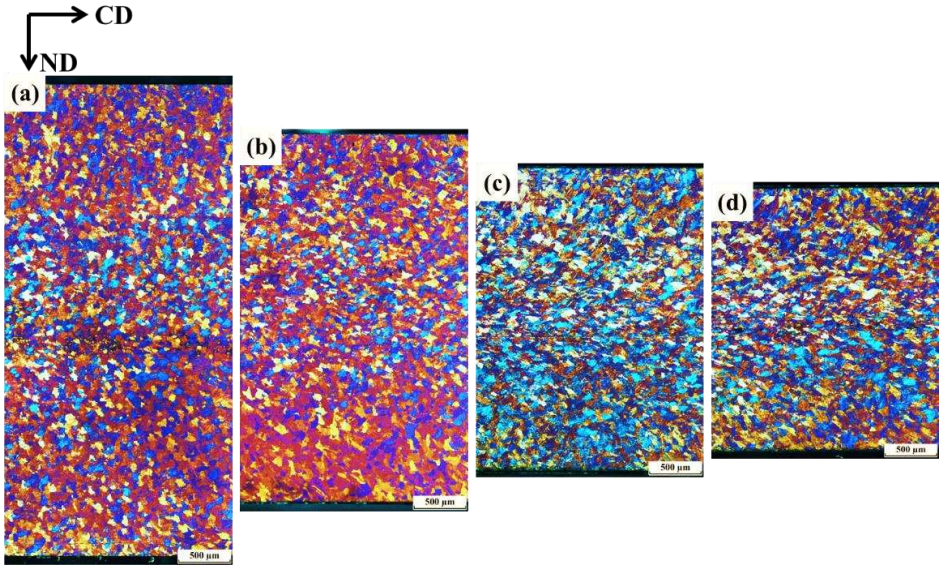

Figure 4. 7 Polarized image of as-cast strips from transverse direction; (a) 2.6 m/min, (b) 3.3 m/min, (c) 4.0 m/min and (d) 4.7 m/min.

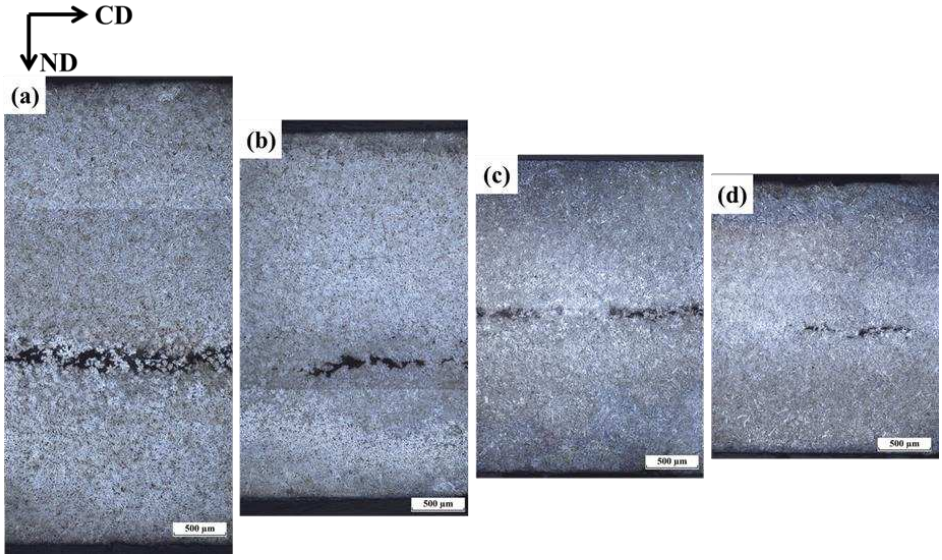

Figure 4. 8 Optical micrographs of homogenized strips from transverse direction; (a) 2.6 m/min, (b) 3.3 m/min, (c) 4.0 m/min and (d) 4.7 m/min.

phase as can be seen in Fig. 4.8. The cross sectional images of homogenized strips under polarized light are presented in Fig. 4.9. There was no significant change in microstructure after homogenization as the degree of deformation during the casting was not enough to trigger a noticeable level of recrystallization. On the other hand, the effect of homogenization heat treatment was visible under SEM which is shown in Fig. 4.10. It is clear that the bright Y/Zn rich region that spread over the Mg12YZn in Fig. 4.5 is hardly noticeable after the homogenization treatment. Instead, the amount of Y and Zn contained in the α-Mg increased, indicating that these elements dissolved into the matrix during the heat treatment.

4.1.3 Mechanical properties of cast strips

To see the effect of casting speed on mechanical properties of the as-cast strips, tensile test was conducted and the stress vs. strain curves are plotted in Fig. 11 and the results are summarized in Table 4. The highest yield strength was observed in the strip cast at 4.7 m/min which had the yield strength of 250.6 MPa. This is due to the fast solidification of the strip and higher degree of deformation which resulted in the finer microstructure and higher degree of work hardening. The yield strength continually decreased along with the casting speed and the strip cast at 2.6 m/min had the lowest yield strength of 194.2 MPa due to the rather slow solidification rate and less deformed microstructure. The casting speed did not have much of an impact on tensile strength and the strips showed similar UTS. The highest tensile strength was found in the strip cast at 4.7 m/min showing 282.9 MPa, and the strip cast at 2.6 m/min had the lowest strength which was 270.9 MPa. The change in casting speed also had an effect on the ductility of the strips. However, it must

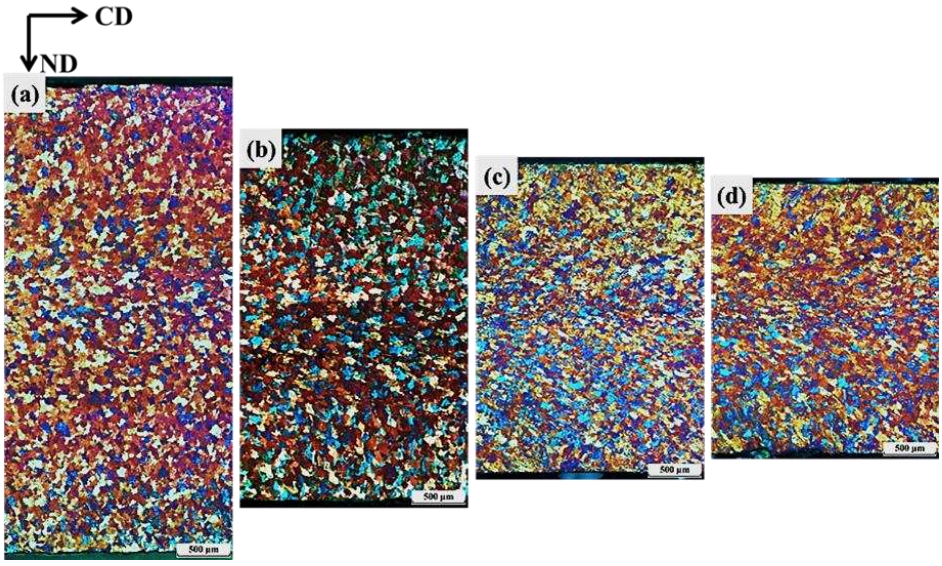

Figure 4. 9 Polarized images of homogenized strips from transverse direction; (a) 2.6 m/min, (b) 3.3 m/min, (c) 4.0 m/min and (d) 4.7 m/min.

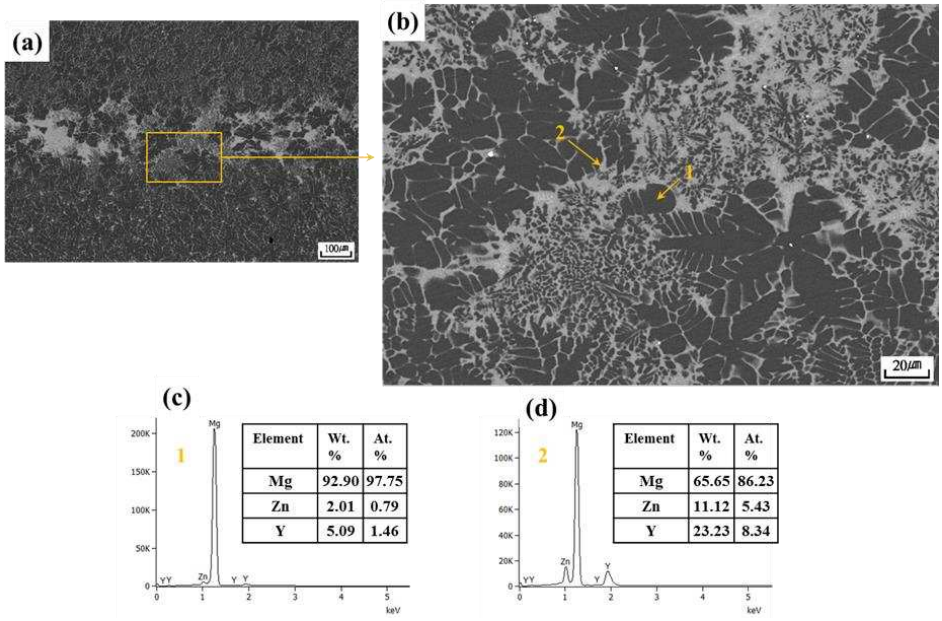

Figure 4. 10 (a, b) SEM-BSE images at the center region of homogenized strip cast at 2.6 m/min, and (c, d) EDS analysis.

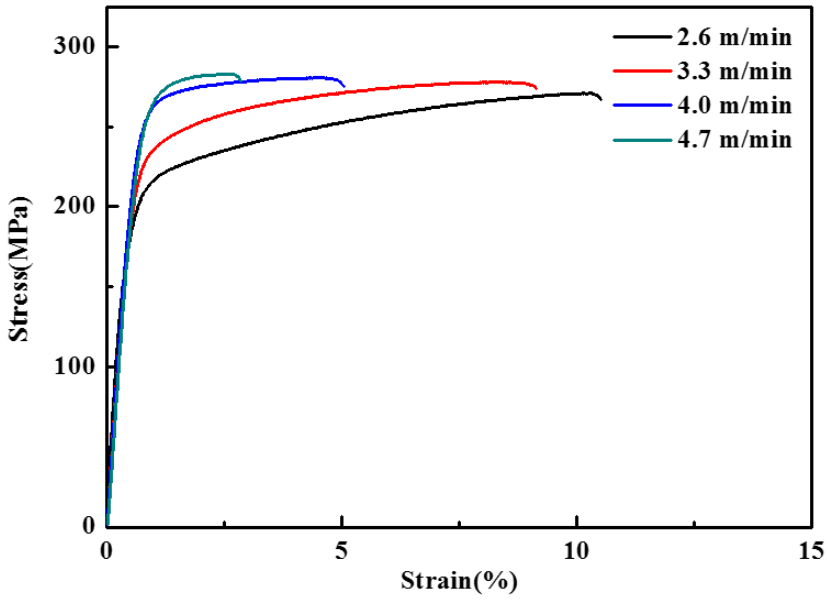

Figure 4. 11 Stress-strain curves of as-cast strips.

Table 4 Tensile properties of as-cast strips.

Casting Speed (m/min)	Y.S. (MPa)	U.T.S. (MPa)	Elong. (%)	Unif. El. (%)	S.H.E. n
2.6	194.2	270.9	9.9	9.7	0.142
3.3	218.9	277.7	8.5	7.6	0.115
4.0	247.9	280.6	4.3	3.9	0.077
4.7	250.6	282.9	2.1	1.9	0.089

be noted that the cast strips had different thickness, and accordingly, the tensile specimen for each casting speeds had different cross sectional area. Thus, the elongation values shall not be used for comparison of ductility between the strips whereas the YS and UTS are generally understood to be independent of specimen thickness [10]. Nevertheless, the YS values show obvious difference between the strips which suggests that the strips cast at higher casting speed had higher degree of deformation which resulted in more work hardening and higher YS. As mentioned in the earlier section, casting thicker strip resulted in longer solidification zone and shorter deformation zone due to the slower solidification and hence less deformed state. It is also possible that the roll separation force and roll torque were not enough to deform the thick strips. From the strain hardening behavior, it also seems reasonable to assume that the strips cast at faster speeds indeed have lower ductility due to the more work-hardened states.

4.1.4 Corrosion properties of cast strips

Corrosion of metallic materials largely depends on its thermodynamic tendency to participate in the electrochemical reactions with surroundings. The thermodynamic stability of the material can be determined by measuring open circuit potential against reference electrodes. To obtain the steady-state potential value of the as-cast Mg-2Y-1Zn (at. %) strips, OCP was measured and the results are shown in Fig 4.12. For all tested samples, the potentials shift towards nobler values within the first moments of exposure, indicating passivation behavior. The passivation is most likely attributed to an initial formation and growth of passive oxide film on the surface. The curves demonstrate that all of the strips reached a steady state at about 600 s after the

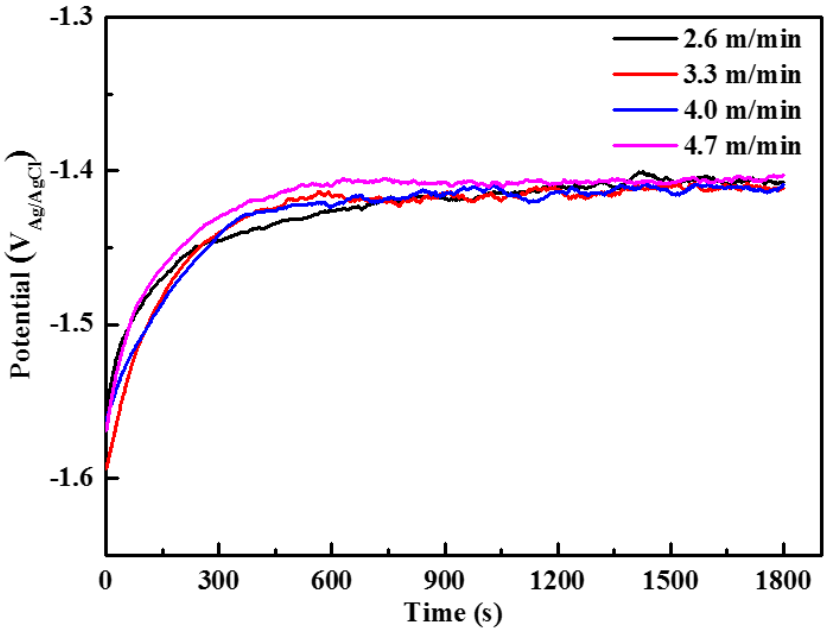

Figure 4. 12 OCP curves of as-cast strips in 3.5 wt. % NaCl solution.

exposure and remain mostly unchanged until the end of the measurements. It shows that the casting speed does not have a significant impact on the OCP values indicating that the surface of the strips have similar thermodynamic stability under the tested solution. However, it should be noted that the actual corrosion rate and the kinetics can not be determined by the OCP alone. To further evaluate the electrochemical properties, cathodic and anodic polarization curves were recorded for each strips as shown in Fig. 4.13 and the results are summarized in Table 5. The polarization curves were not symmetrical and all of the curves showed a similar trend in the tested solution. In the polarization measurement of magnesium alloys, the cathodic curves are assumed to represent the hydrogen evolution through reduction of the water molecules, while the anodic curves represent the dissolution of magnesium meaning that the characteristics of the strips were almost identical. As can be seen from Table 5, the E_{corr} values followed the trend similar to that of OCP which was not largely affected by the casting speed in general. It is also worth mentioning that the corrosion potential E_{corr} did not equal the OCP values. The corrosion potential showed up to 68 mV higher potential compared to the OCP value, indicating that there was a change in surface condition during the polarization measurement due to the formation of corrosion product. The corrosion current densities (i_{corr}) and cathodic Tafel constant (b_c) were determined by Tafel-extrapolation using the cathodic branch and the corrosion potential (E_{corr}), as the anodic branch did not demonstrate Tafelian behavior which contains linear region. From Table 5, it was found that the i_{corr} increases with faster casting speeds suggesting the strip cast at 4.7m/min has the highest corrosion rate. The microstructures of the alloys after the electrochemical tests were examined by optical microscope and SEM for better understanding.

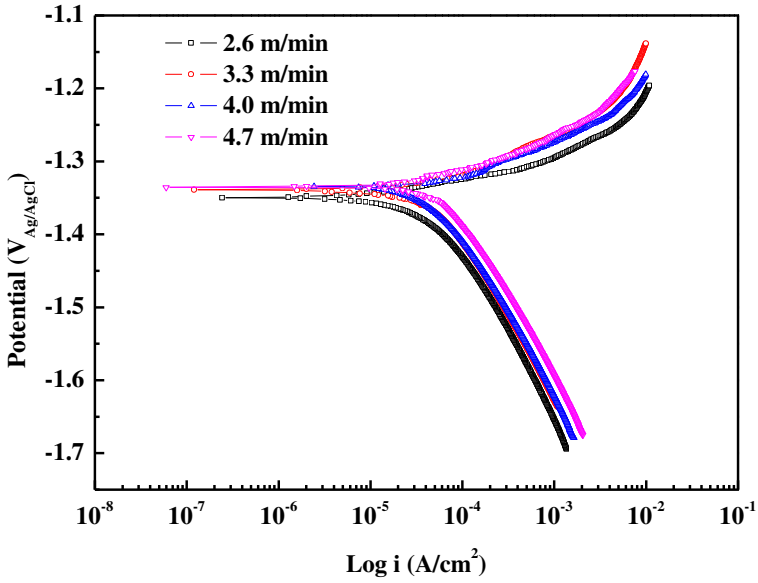

Figure 4. 13 Polarization curves of as-cast strips in 3.5 wt. % NaCl solution.

Table 5 Electrochemical properties of as-cast strips measured in 3.5 wt. % NaCl solution.

Casting speed (m/min)	OCP ($V_{Ag/AgCl}$)	i_{corr} ($\mu A/cm^2$)	E_{corr} ($V_{Ag/AgCl}$)	b_c (mV dec^{-1})	P_i (mm/year)
2.6	-1.408	49.67	-1.351	283.2	1.13
3.3	-1.411	56.23	-1.338	303.6	1.28
4.0	-1.405	75.62	-1.337	308.6	1.73
4.7	-1.402	80.94	-1.347	325.1	1.85

Figure 4.14 shows the surface and cross-sectional microstructure of the as-cast strip after 0.5 hour of immersion without the corrosion product. It can be seen that, the corrosion proceeds along the inter-dendritic precipitates between the α-Mg matrix suggesting galvanic corrosion between the two phases. The overall surface the α-Mg of seems relatively intact whereas the crevices are formed between the α-Mg. Some traces of precipitates are visible in the crevices, but at this stage, it is still hard to determine which phase was dissolved preferentially. Figure 4.15 shows the SEM corrosion morphologies of as-cast strip after 1 hr of immersion. The entire surface of the strip was covered by gypsum flower-like corrosion products. These corrosion products were later confirmed to be $Mg(OH)_2$ as can be seen from XRD analysis in Fig. 4.16. No other corrosion product containing Y or Zn was detected by XRD scan. After removing the corrosion products (Fig. 4.15 (c, d)), it can be confirmed that it is actually the α-Mg matrix that has been preferentially corroded around the precipitates. At higher magnification, the dissolution of α-Mg is clear around the remaining precipitates. The degradation of α-Mg adjacent to the precipitates indicates that the precipitate is electrochemically nobler phase acting as a galvanic corrosion site.

For clarification, the electrochemical potential distribution was monitored by SKPM mapping to examine the difference in potential between the precipitates and α-Mg (Fig. 4.17). In this mode of operation, the differences in intensity represent relative potential difference between the AFM tip (Cr-Au in this study) and the local surface potential. Dark spots indicate a small Volta potential difference whereas bright spots represent a large difference relative to the cantilever tip. The potential map revealed that the second phase (dark

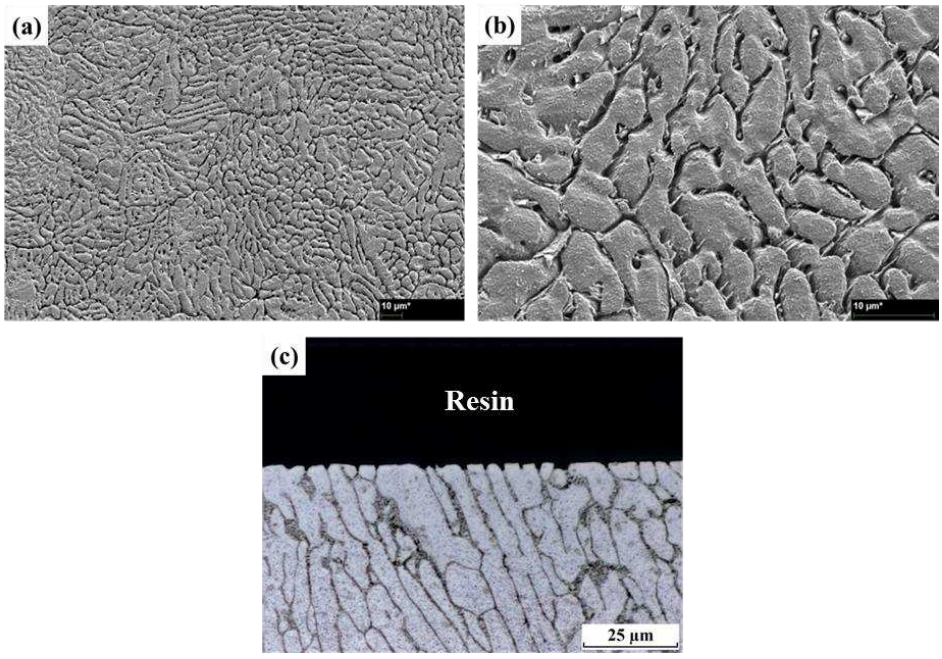

Figure 4. 14 (a, b) Surface SEM images and (c) cross sectional optical micrograph of as-cast strip after 0.5 hr immersion in 3.5 wt. % NaCl solution without corrosion products.

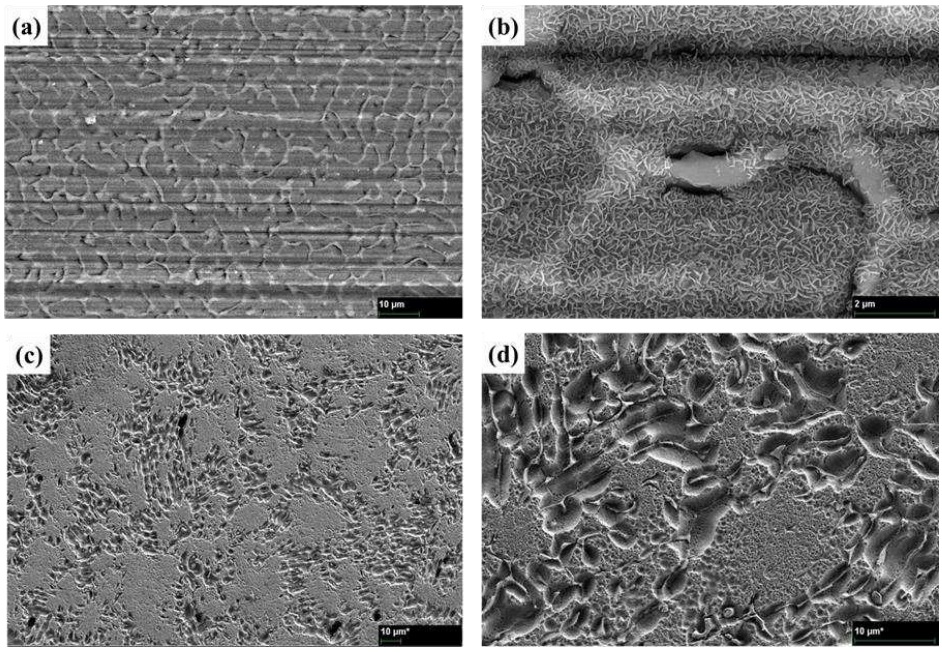

Figure 4. 15 SEM images of as-cast strip after 1 hr of immersion in 3.5 wt. % NaCl solution; (a, b) with corrosion products, and (c, d) after removing the products

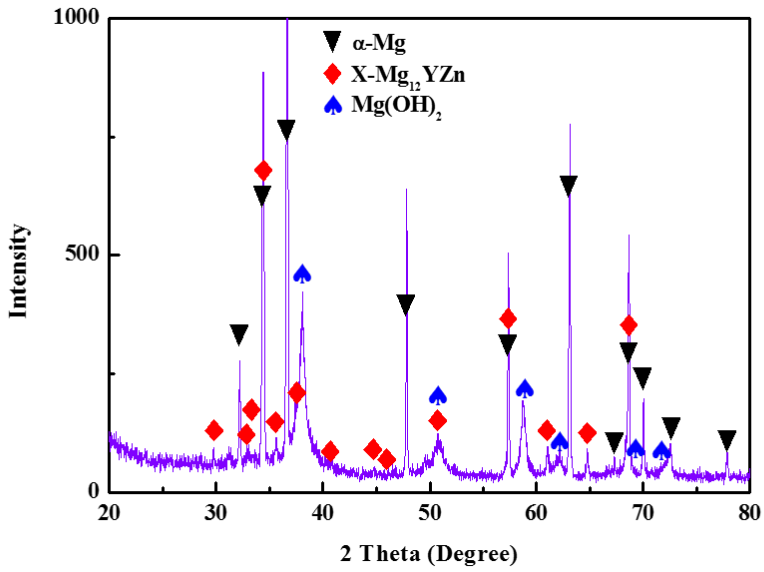

Figure 4. 16 XRD peaks of as-cast strips after 1 hr immersion in 3.5 wt. % NaCl.

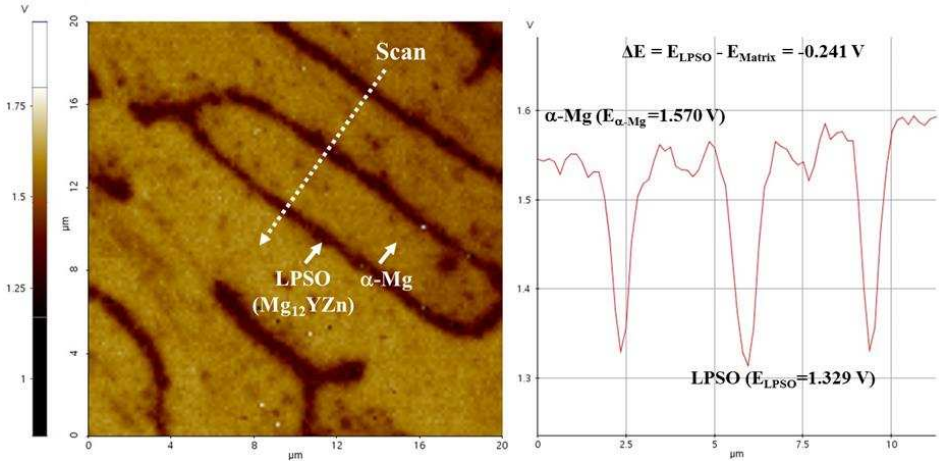

Figure 4. 17 SKPM surface potential distribution of as-cast strip.

region) has higher Volta potential than the α-Mg matrix (bright region), indicating the precipitate is electrochemically nobler than the α-Mg. The potential difference between the two phase were measured to be up to 450 mV, suggesting the interface acts as an active micro-galvanic corrosion site due to the large potential difference. The SKPM results provide an evidence for the corrosion initiation at the precipitates that was found in corrosion morphology observation. It could also explain the higher corrosion density observed in the strips cast at faster speeds. The as-cast microstructure (Fig. 4.6) showed that the increase in casting speed resulted in finer dendritic structure, which provides more contact area between the precipitates and the α-Mg matrix. Considering the fact that the corrosion initiates at the interface of the two phases, the increase in contact area is responsible for the higher i_{corr} found in the strips with higher casting speeds.

The immersion tests were conducted to further evaluate the corrosion properties. The hydrogen evolution rate and the corrosion rate of the as-cast samples are shown in Fig. 4.18. and Table 6. It shows that the hydrogen evolution rate and the corrosion rate increases in the order of $4.7 < 4.0 \leq 3.3 < 2.6$ m/min, indicating that the strip cast at faster speeds had better corrosion resistance. The immersion test results contradicts with the electrochemical test results which showed the opposite trend. The macroscopic images (Fig. 4.19) taken after the immersion tests show that the corrosion mainly occurred around the central part of the strip. The central parts of the strips were more prone to corrosion since the strips had segregation regions at the mid-thickness section which could have led to macro-galvanic corrosion between the surface and the cross sectional part of the strips. As the strips cast at lower speeds had larger

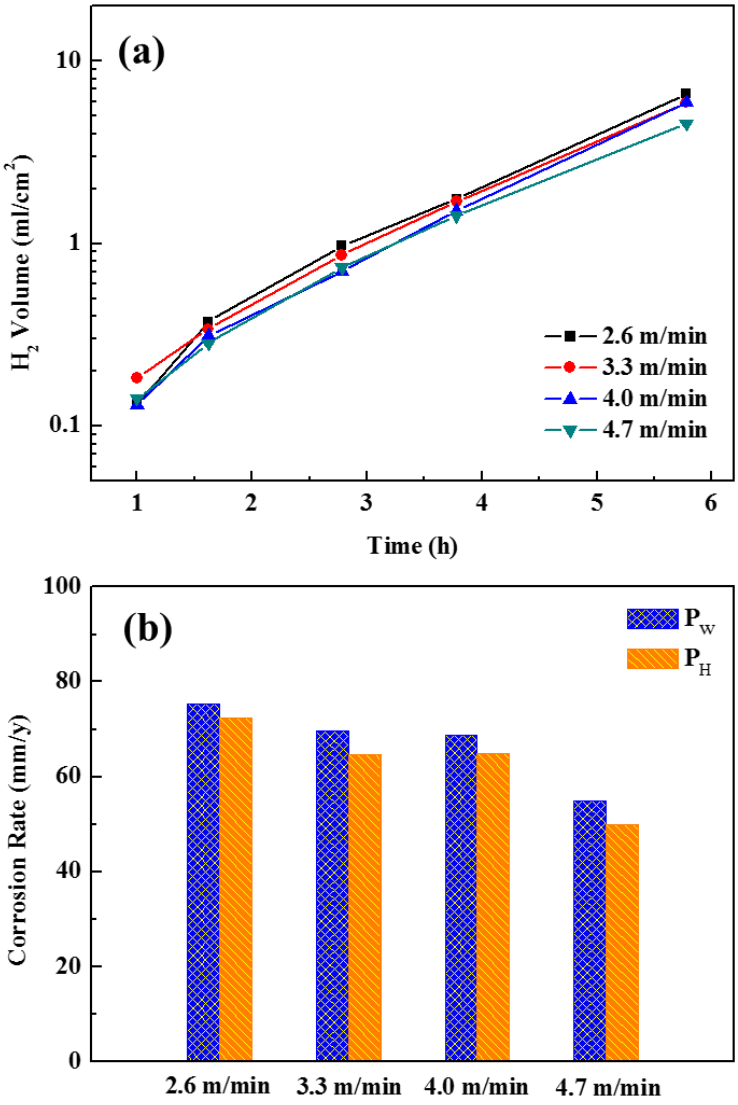

Figure 4. 18 (a) Hydrogen evolution rates and (b) corrosion rates of as-cast strips in 3.5 wt. % NaCl solution.

Table 6 Corrosion rates of as-cast strips based on weight loss and hydrogen evolution.

Casting speed (m/min)	Corrosion rate (mm/year)	
	P_W	P_H
2.6	75.3	72.3
3.3	69.6	64.7
4.0	68.8	64.9
4.7	55.0	50.2

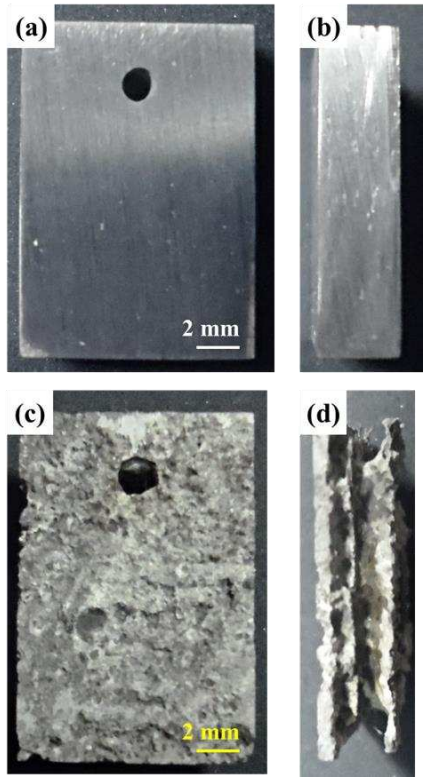

Figure 4. 19 Macroscopic images of as-cast strip specimen (a, b) before immersion test and (c, d) after immersion test.

cross sectional area, it resulted in higher corrosion rate even though it had better corrosion resistance at the surface.

4.2 Hot-rolling of TRC strips

4.2.1 Microstructure

The optical micrographs of as-rolled Mg-2Y-1Zn (at.%) sheets preheated at 400 ^{o}C and 500 ^{o}C (3.3-P400, 3.3-P500) are represented in Fig. 4.20. The as-rolled sheets had elongated structures towards the rolling direction for all casting and rolling conditions. The as-cast strips had a large fraction of area covered by the secondary phase that appears as the dark continuous lines which extends across the rolling direction. It is hard to distinguish the grain boundaries clearly due to the amount of secondary phase present at lower preheating temperature (3.3-P400), but deformed grain structures are visible from the samples preheated at higher temperatures (3.3-P500). It seems that these secondary phase spread between the grains and along the grain boundaries. It was hard to confirm the sign of active dynamic recrystallization (DRX) as can be seen from the coarse elongated grains, although the rolling temperature was sufficiently high for other Mg alloys to undergo DRX. The majority of grains were more than 25 μm in size and the fine recrystallized grains were hardly visible. It is assumed that high amount of Y content suppressed DRX due to retarded grain boundary motion and increased the recrystallization temperature [11].

The optical micrographs of as-polished 3.3-P400 and 3.3-P500 are also presented in Fig. 4.21 for better visualization of the secondary phase

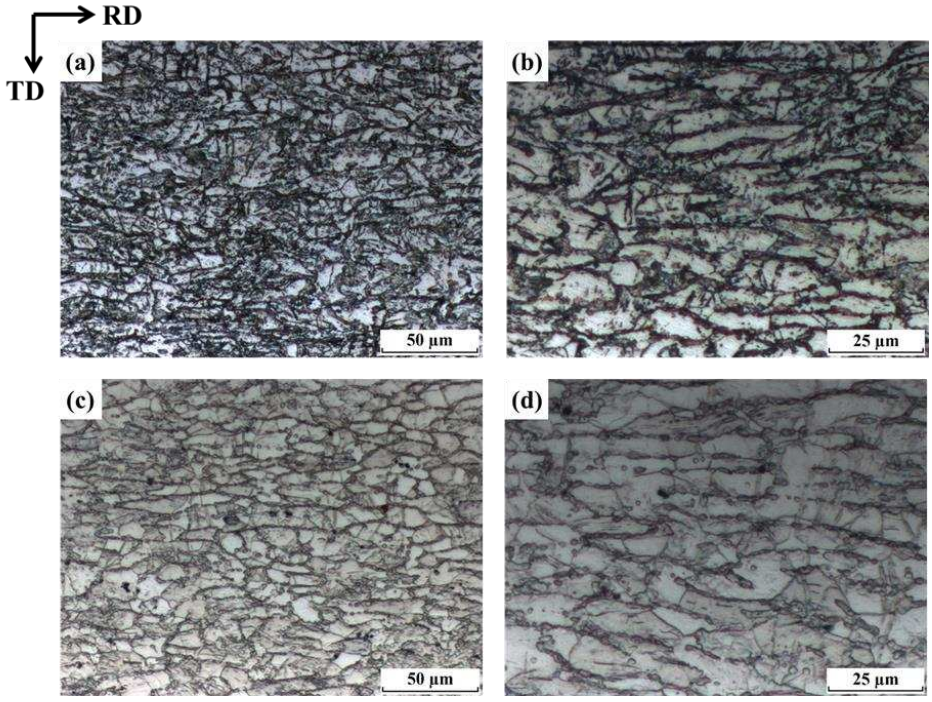

Figure 4. 20 Optical micrographs of as-rolled sheets from normal direction; (a, b) 3.3-P400 and (c, d) 3.3-P500.

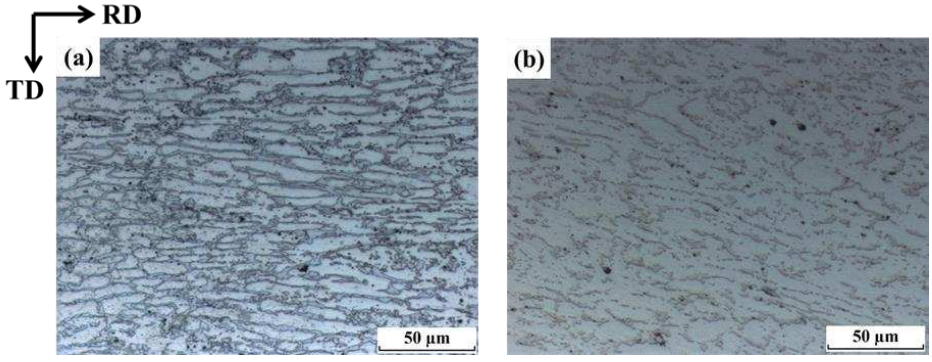

Figure 4. 21 Optical micrographs of polished as rolled (a) 3.3-P400 and (b) 3.3-P500.

distribution. It is obvious that these secondary phases originates from the dendritic structure that was visible in the as-cast alloy. The amount of secondary phase gradually decreased as the preheating temperature was increased. From Fig. 4.21, it is noticeable that these precipitates become more discontinuous which implies that some of the precipitates were dissolved into the matrix during the preheating. Figure 4.22 and 4.23 shows the SEM images and the EDS results of as-rolled sheets 3.3-P400 and 3.3-P500. The as-rolled sheets consisted of three phases, which were α-Mg, $Mg_{12}YZn$, and $Mg_{24}Y_5$ based on the EDS results. The secondary phase that spread across the rolling direction was identified to be $Mg_{12}YZn$ as can be seen from the EDS analysis in Fig. 4.22 and the bright fine particles in both P400 and P500 were found to be $Mg_{24}Y_5$. The discontinuity of secondary phase at higher preheating temperature is also prominent in the SEM image and the EDS analysis suggests that some of the secondary phases dissolved into the α-Mg during higher preheating temperature, which can be confirmed by higher Y and Zn content in the 3.3-P500 compared to the 3.3-P400. Figure 4.24 shows the XRD results of the as-rolled sheets at each preheating temperatures. The XRD peaks suggests that α-Mg, $Mg_{12}YZn$, and $Mg_{24}Y_5$ are present similar to the EDS analysis results. As can be seen from XRD scan, the peak intensities that correspond to the $Mg_{12}YZn$ phase weaken in response to the increase in preheating temperature. The change in peak intensity also implies that some of the $Mg_{12}YZn$ dissolved into the Mg matrix which agrees with the EDS results. The peaks for $Mg_{24}Y_5$ did not show a noticeable change in intensity over the preheating temperature range, which indicates the high thermal stability of the secondary phase.

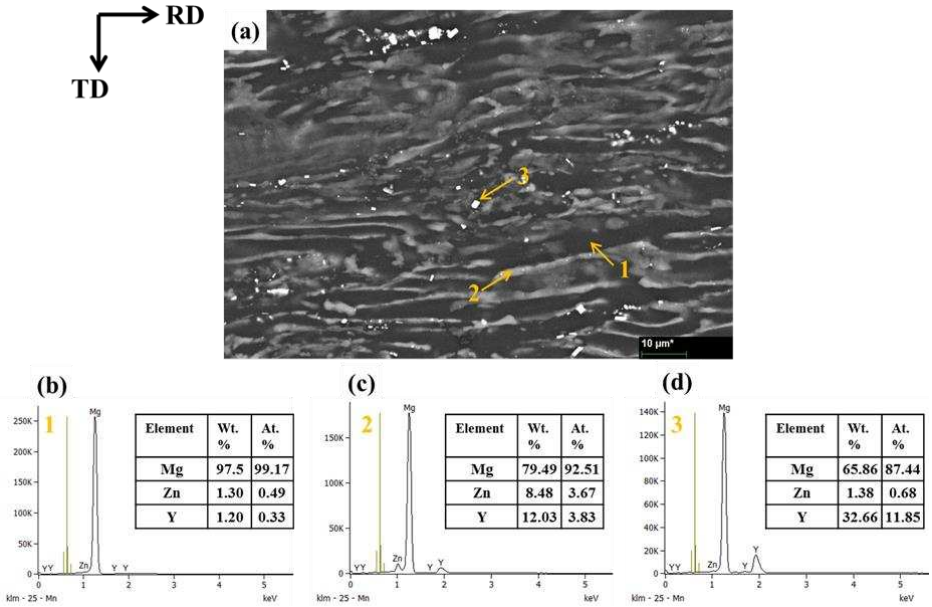

Figure 4. 22 (a) SEM-BSE image of 3.3-P400 from normal direction and (b, c, d) EDS analysis.

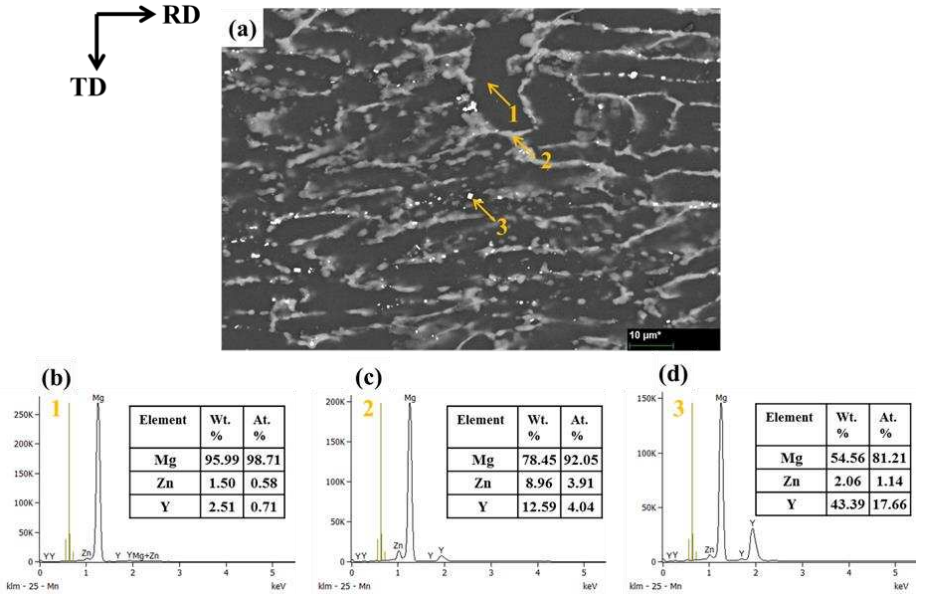

Figure 4. 23 (a) SEM-BSE image of 3.3-P500 from normal direction and (b, c, d) EDS analysis.

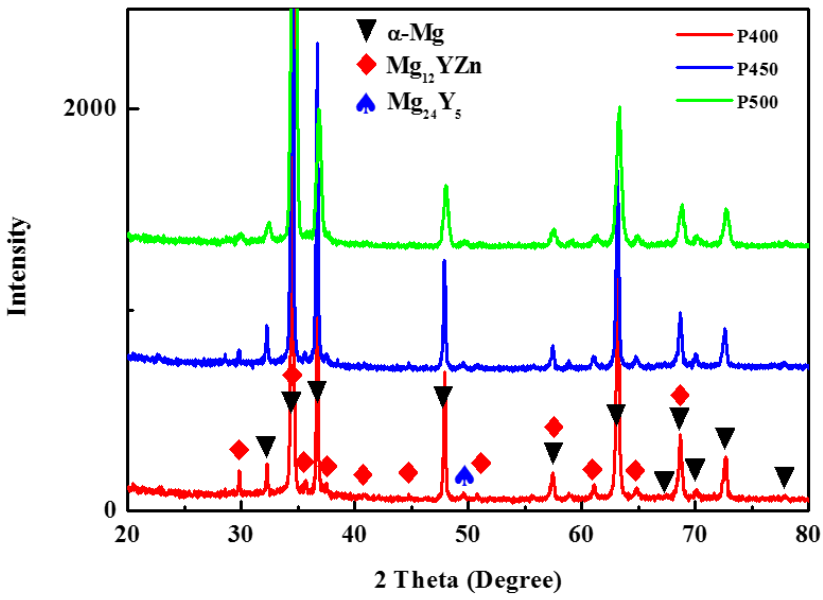

Figure 4. 24 XRD peaks of as-rolled sheets.

The hot-rolled strips were annealed at different temperatures to see the effect of annealing treatment on microstructural change and mechanical properties. The rolled strips were first annealed at 300 ^{o}C for 1 hr, but the change in microstructure and mechanical properties were almost negligible. When the annealing temperature was increased to 350 ^{o}C, the YS and UTS suddenly decreased in all samples.

Figure 4.25 represents the optical micrographs of the hot-rolled sheets preheated at 500 ^{o}C and annealed at 350 ^{o}C (3.3-P500A350) for 1 hr. The distribution of secondary phase remains almost unchanged and the deformed elongated grain structure is still visible even after annealing. However, some fine recrystallized grains of about up to 5 μm are visible at higher magnification. The recrystallized grains are mostly clustered around the second phase particles suggesting that the precipitates acted as the nucleation sites for recrystallization.

The samples were further annealed at higher temperatures for the sake of better corrosion properties that will be discussed later this chapter. The sample annealed at 500 ^{o}C (3.3-P500A500) is shown in Fig 4.26. At this annealing temperature, almost all the grains have recrystallized and grain size was in range of 5-15 μm. The grain size was relatively small considering the high annealing temperature. It seems that the precipitates between the grains inhibited further grain growth of the recrystallized grains. In almost all grains, a lamellar morphology was observed. These were initially considered to be annealing twins but the BSE image revealed that these samples contain lamellar LPSO phase as can be seen from Fig. 4.26 (a). When the annealing temperature was raised to 550 ^{o}C, significant grain growth occurred (Fig. 4.27).

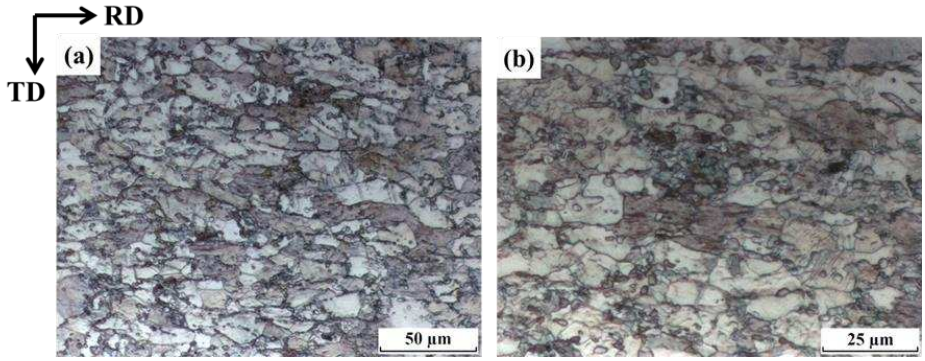

Figure 4. 25 Optical micrographs of 3.3-P500A350 from normal direction.

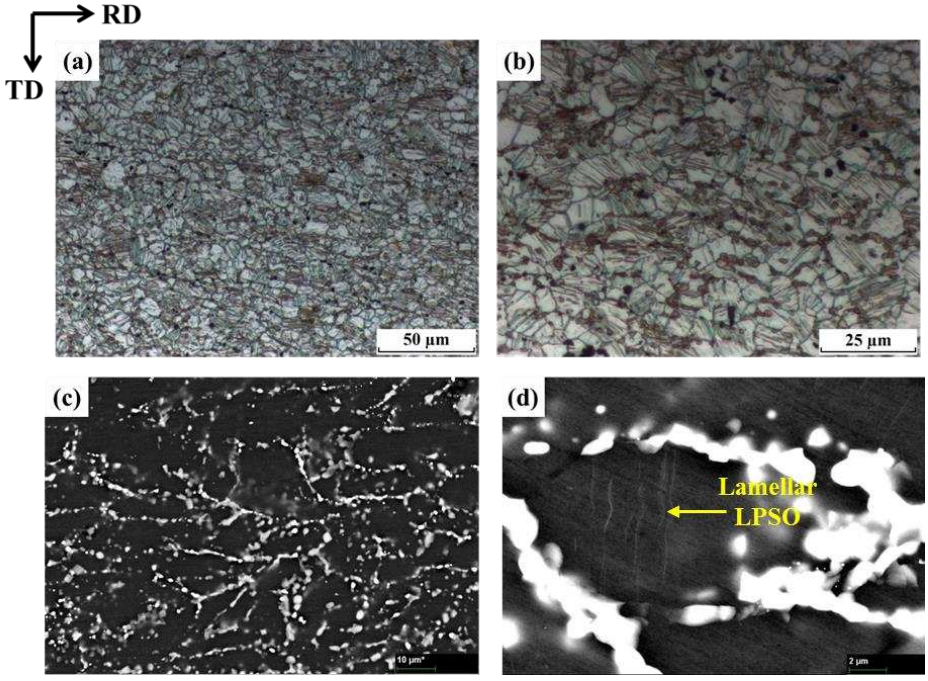

Figure 4. 26 (a, b) Optical micrographs and (c, d) SEM-BSE images of 3.3-P500A500 from normal direction.

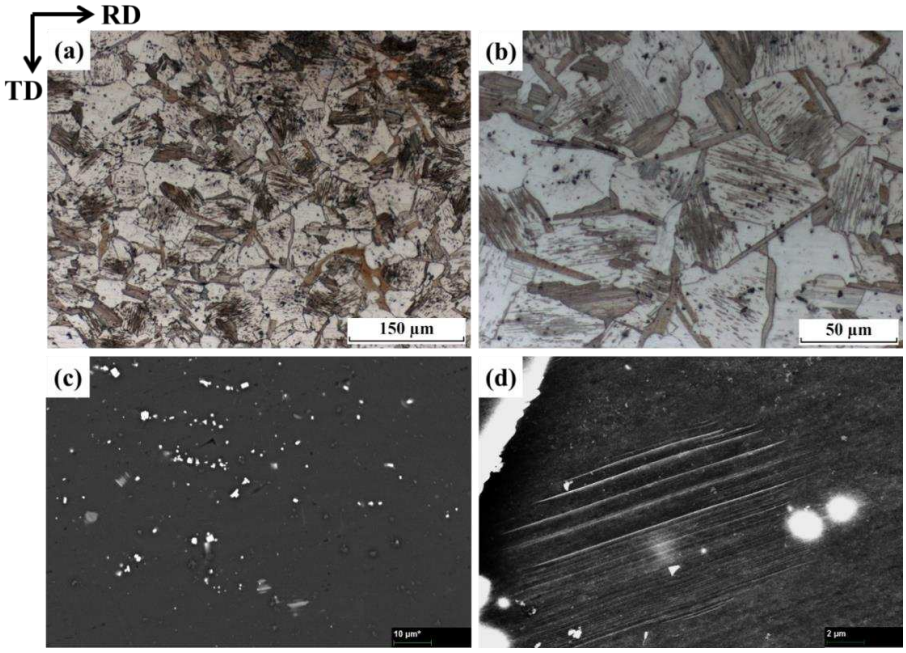

Figure 4. 27 (a, b) Optical micrographs and (c, d) SEM-BSE images of 3.3-P500A500 from normal direction.

The average grain size was measured to be 50 μm. The inter-dendritic LPSO phase that was visible since the as-cast condition was no longer observed as the sample was heated above its complete dissolution temperature. Instead, the lamellar LPSO was observed across the grains and intra-granular coagulated LPSO was also visible which were formed during the cooling [12].

4.2.2 Mechanical properties

The tensile properties of as-rolled Mg-2Y-1Zn (at.%) strips at room temperature are listed in Table 7 according to their casting speeds and preheating temperatures. The highest yield strength (YS) and ultimate tensile strength (UTS) was observed for the specimen cast at 3.3 m/min and hot-rolled with the preheating temperature of 500 ^{o}C (3.3-P500). On the other hand, the lowest YS and UTS was seen in the sample cast at 2.6 m/min and hot-rolled with the preheating of 500 ^{o}C (2.6-P500). The 2.6-P500 samples showed very brittle tensile behavior and reached the fracture point even before exhibiting any characteristic yield point in repeated trials. This might have originated from casting defects such as centerline segregation, which could not be removed even after the homogenization heat treatment. The strip cast at 2.6 m/min showed significant amount of centerline segregation compared to the other strips cast at higher speeds. In fact, the strip cast at 2.6 m/min showed poor elongation for all preheating temperatures as summarized in Table 7. In addition, the rich chemistry around the central part of the strip might have caused incipient melting during high temperature preheating and hot-rolling which could have introduced other forms of defects such as cracking. According to these factors, the 2.6-P500 showed very brittle behavior compared to other samples that were cast at higher speeds. Among the samples

Table 7 Tensile properties of as-rolled sheets.

Casting Speed (m/min)	Preheating (°C)	Y.S. (MPa)	U.T.S. (MPa)	Elong. (%)	Unif. El. (%)	S.H.E. n
2.6	400	324.1	358.5	1.7	1.6	0.115
	450	334.1	375.3	3.0	2.9	0.097
	500	-	329.8	-	-	-
3.3	400	318.4	359.1	6.2	4.9	0.094
	450	339.7	382.8	6.1	5.3	0.080
	500	349.2	393.4	7.0	5.6	0.081
4.0	400	319.6	354.4	5.8	4.7	0.071
	450	331.2	377.1	8.9	6.6	0.082
	500	338.0	381.0	7.3	6.5	0.081
4.7	400	311.5	344.2	3.5	3.4	0.078
	450	321.6	354.8	2.7	2.5	0.086
	500	332.3	375.7	7.3	5.8	0.082

that had noticeable yield point, the sample cast at 4.7 m/min and hot-rolled with the preheating temperature of 400^{o}C (4.7-P400) showed the lowest YS and UTS. The YS and UTS of as-rolled samples are also plotted according to their casting speeds and pre-heating temperatures in Fig 4.28. The data point for 2.6-P500 was excluded from the plot as it showed early fracture before acquiring a reliable data even after the repeated trials. According to the figures, both the YS and UTS at as-rolled state are inversely proportional to the casting speed. This contradicts with the tensile test results of as-cast alloys in which the higher casting speed resulted in higher YS and UTS. After the hot-rolling process, the samples cast at higher speeds tended to have lower YS and UTS although the difference was not significant. It is believed that the changes in strength are resulted by the total reduction ratio rather than the casting speed itself. The thickness of the as-cast strips increased as the casting speed was decreased which caused the highest total reduction ratio of the trip cast at 2.6 m/min and vice versa. Fukuda et al. reported that the strength was improved as the result of higher total reduction ratio due to the grain refinement and secondary phase distribution in case of Mg-8Al-1Zn-1Ca (AZX811) alloy [13]. Even though there was no obvious change in microstructure between the samples cast at different speeds in this study, the YS and UTS showed an increasing trend according to the increase in total reduction ratio. On the other hand, the effect of preheating temperature on the YS and UTS was more prominent as can be seen in both Fig and Fig. The samples hot-rolled at higher preheating temperatures showed higher YS and UTS throughout all casting speeds consistently. For each casting speeds, the alloy sheets preheated at 500 ^{o}C (P500) showed the highest YS and UTS followed by the alloys rolled with the preheating of 450 ^{o}C (P400) and lastly 400 ^{o}C (P400). LPSO type alloys

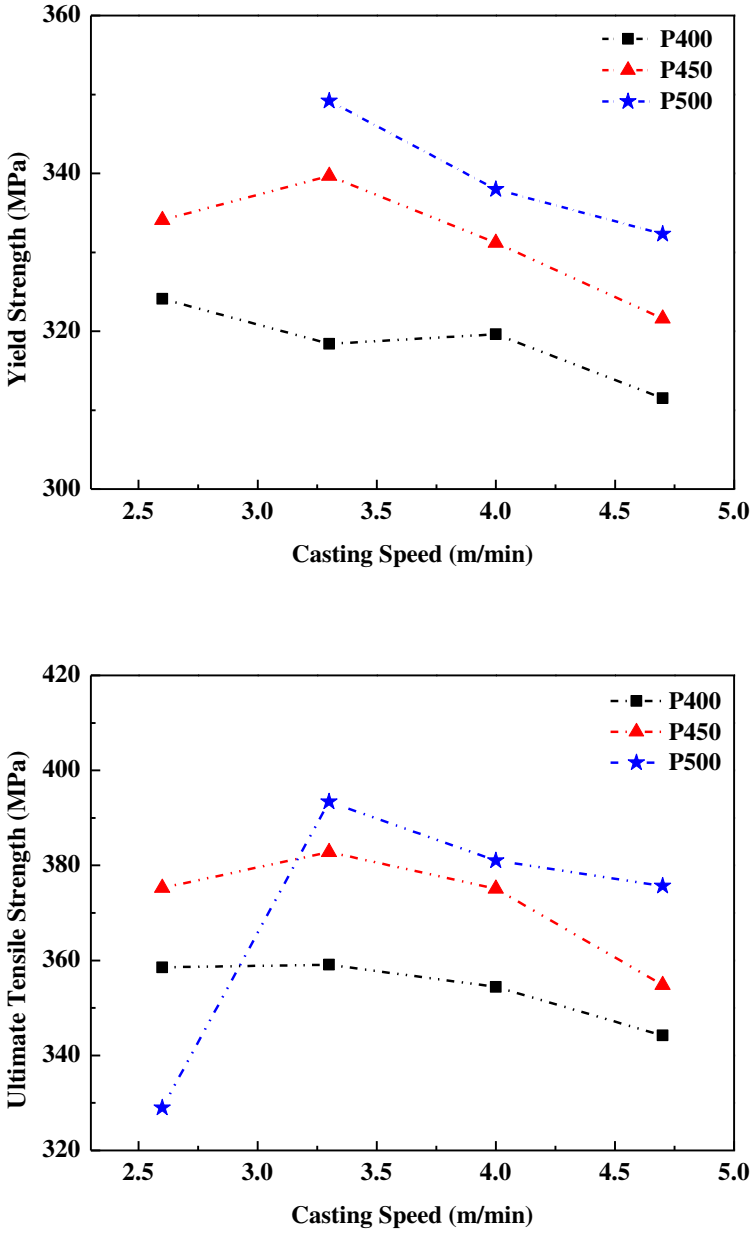

Figure 4. 28 (a) YS and (b) UTS of as-rolled sheets in accordance with the casting speeds and preheating temperatures.

are reported to have a large variation in their mechanical properties depending on the process temperature [14]. Su et al. reported the change in microstructure and mechanical property of Mg-2Y-1Zn (at. %) alloy, in which the alloy showed a better strength at higher preheating temperature in certain temperature range due to the repeated dissolution of the $Mg_{12}YZn$ phase [15]. As confirmed earlier in Fig. 4.20, the main difference between the alloys rolled at 400 ^{o}C (2.6-P400) and 500 ^{o}C (2.6-P500) is their distribution of secondary phases, mainly the $Mg_{12}YZn$. This trend was also observed regardless of the casting speeds and all of the alloys hot-rolled with higher preheating temperature contained less secondary phases compared to the strips hot-rolled at 400 ^{o}C. The amount of Y and Zn contained in the α-Mg was the highest in the alloys rolled with the preheating of 500 ^{o}C followed by 450 ^{o}C and then the lowest amount found for the 400 ^{o}C. It is considered that the dissolution of the secondary phase into the matrix at higher preheating temperatures and higher solute concentration in α-Mg led to solid solution strengthening similar to the reports of Su et al.[15]. Su observed the increase in hardness of hot-rolled Mg-2Y-1Zn (at. %) alloy as the $Mg_{12}YZn$ phase gradually dissolved into the α-Mg. It is also possible that the variation in strength comes from the distribution of secondary phase itself. It is commonly understood that finely dispersed secondary phase around the grain boundaries hinders dislocation motion and act as an effective strengthening constituent [14]. In that sense, the coarse continuous network of $Mg_{12}ZnY$ phase found in the alloys hot-rolled at 400 ^{o}C could have a negative effect on the tensile properties. Yang et al. found that the coarse continuous $Mg_{12}ZnY$ phase act as a crack initiation site in the Mg-4Y-1.2Mn-1Zn (wt. %) alloy [16]. As shown in Fig. 4.21, the amount of $Mg_{12}ZnY$ phase decreases with the increase in preheating temperature and becomes

quasi-continuous structure. The microstructure observation suggests that finer discontinuous secondary phase was more effective in terms of alloy strengthening as plotted in Fig 4.28.

The tensile properties of hot-rolled alloys annealed at 350 ^{o}C for 1hr are listed in Table 8. It is observed that both the YS and UTS decreased compared to the as-rolled state listed in Table 7, while gaining the ductility in general. Although there seemed to be no significant change in microstructure after the annealing (Fig 4.25), it seems reasonable to attribute the decrease in strength and increase in ductility to be the result of partial recrystallization and recovery during the annealing process considering the high thermal stability of the second phase. In Fig 4.29, the YS and UTS of the samples annealed at 350 ^{o}C for 1hr are plotted according to their casting speeds and pre-heating temperature. It can be identified that the effect of preheating temperature on the strength of hot-rolled sheets is still obvious even after the annealing treatment. The samples preheated at higher temperatures had higher YS and UTS regardless of the casting speeds as can be seen from the figures. On the other hand, the relationship between the casting speeds and the strengths was more incoherent after the annealing compared to the as-rolled condition. Both the YS and UTS showed fluctuation and there was no clear trend between the casting speeds and the strengths. The UTS plot in particular became almost flat after the annealing treatment.

The as-rolled sheets were processed through high temperature annealing to see whether it makes further improvement in corrosion properties. Only the samples 3.3-P500 were examined during the process as the effect of casting speeds and the preheating temperature was considered to be insignificant after

Table 8 Tensile properties of hot-rolled sheets annealed at 350 °C.

Casting Speed (m/min)	Preheating (°C)	Y.S. (MPa)	U.T.S. (MPa)	Elong. (%)	Unif. El. (%)	S.H.E. n
2.6	400	237.6	323.3	12.0	11.8	0.129
	450	286.1	347.1	10.5	8.8	0.103
	500	327.3	361.9	-	0.9	-
3.3	400	280.4	330.5	3.4	3.1	0.112
	450	294.6	344.6	11.4	7.4	0.088
	500	318.6	366.3	7.9	6.5	0.082
4.0	400	268.3	330.0	16.0	10.0	0.104
	450	293.9	349.5	14.2	8.5	0.089
	500	308.9	359.3	10.5	6.3	0.083
4.7	400	240.6	300.5	6.2	6.0	0.114
	450	289.9	345.6	8.3	7.0	0.091
	500	303.1	349.2	5.8	5.0	0.085

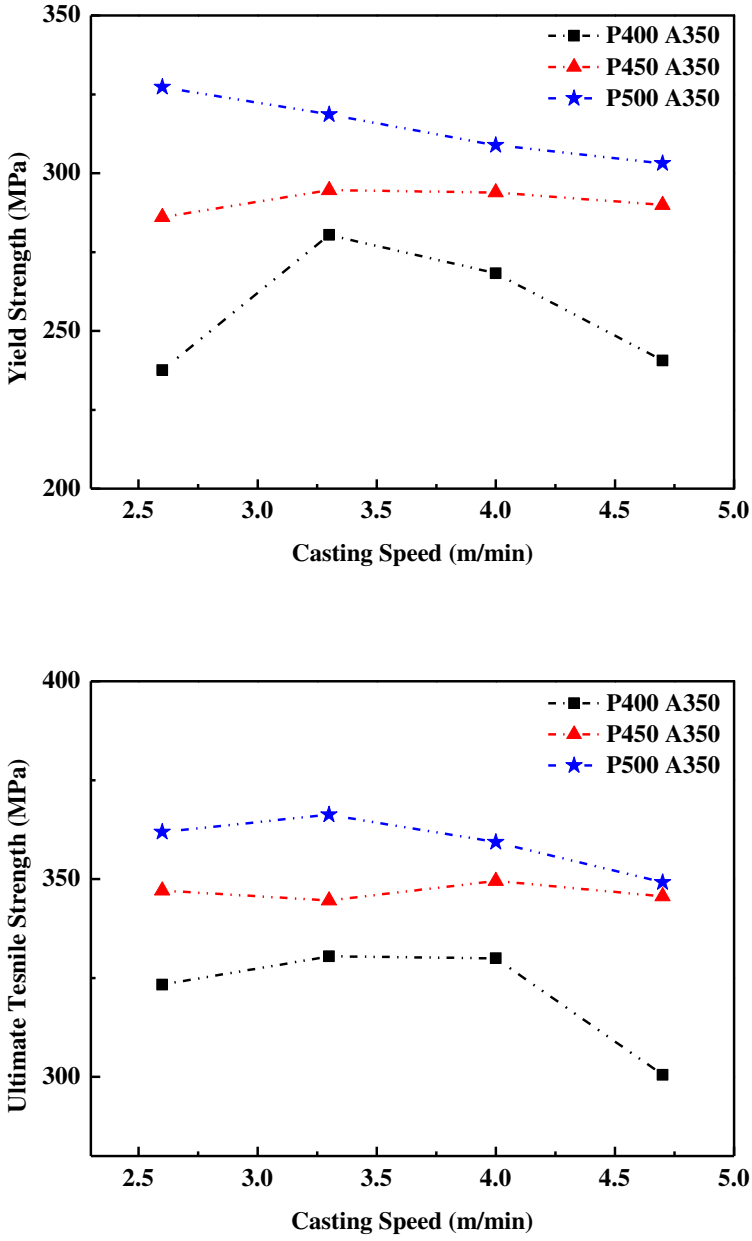

Figure 4. 29 (a) YS and (UTS) of hot-rolled sheets annealed at 350 ^{o}C in accordance with the casting speeds and preheating temperatures.

these high annealing temperatures. The stress-strain curves of samples annealed at 500 ^{o}C and 550 ^{o}C (3.3-P500A500, 3.3-P500A550) are plotted in Fig. 4.30. with the corresponding curves of 3.3-P500 and 3.3-P500A350 for comparison. It is evident that both YS and UTS were deteriorated as a result of the high temperature annealing (Table 9). In case of the 3.3-P500A500, the drop in YS was particularly large as the grains almost fully recrystallized and the dislocations were removed. The dissolution of the precipitates is also responsible for the decrease in strength. In return, the ductility was improved to a large degree as a result of recovered grains and finer precipitates. At the annealing temperature of 550 ^{o}C, the YS further decreases due to the excessive grain growth. On the other hand, it retained relatively good UTS considering the degree of grain growth.

4.2.3 Corrosion properties

The results of electrochemical test for the as-rolled sheets are shown in Table 10. The similar OCP values were observed throughout the preheating temperatures and the casting speeds although the as-rolled samples showed clear change in microstructure depending on their preheating temperature. This was not expected as the as-rolled sheets had different amount of precipitate that has the nobler electrochemical potential compared to the Mg-matrix. The electrochemical potential also largely depends on a distribution and shape of the secondary phase particles which could have affected this phenomenon. The polarization curves of the as-rolled samples are shown in Fig. 4.31. The corrosion potential E_{corr} showed increased values compared to the OCP for all tested specimens indicating rapidly changing surface environment. Again, the processing parameters did not show much of an impact on the corrosion

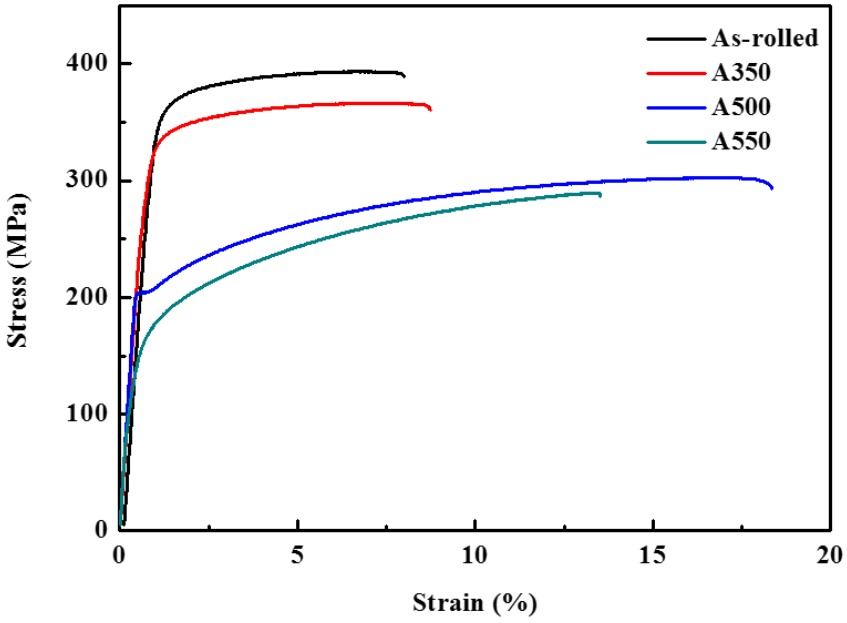

Figure 4. 30 Stress-strain curves of 3.3-P500 with different annealing conditions.

Table 9 Tensile properties of 3.3-P500 with different annealing conditions.

Casting Speed (m/min)	Preheating (°C)	Annealing (°C)	Y.S. (MPa)	U.T.S. (MPa)	Elong. (%)	Unif. El. (%)	S.H.En
3.3	500	As-rolled	349.2	393.4	7.0	5.6	0.081
		350	318.6	366.3	7.9	6.5	0.082
		500	203.9	302.3	17.7	16.1	0.198
		550	162.1	289.3	12.6	12.5	0.253

Table 10 Electrochemical properties of as-rolled sheets in 3.5 wt. % NaCl solution.

Casting speed (m/min)	Preheating (°C)	OCP ($V_{Ag/AgCl}$)	i_{corr} ($\mu A/cm^2$)	E_{corr} ($V_{Ag/AgCl}$)	b_c (mV dec^{-1})	P_i (mm/year)
2.6	400	-1.473	763.15	-1.330	418.52	17.43
	450	-1.481	579.46	-1.338	391.42	13.24
	500	-1.475	414.47	-1.331	358.24	9.47
3.3	400	-1.482	799.64	-1.346	412.96	18.27
	450	-1.477	654.63	-1.336	396.23	14.95
	500	-1.468	472.02	-1.330	397.11	10.79
4.0	400	-1.476	819.97	-1.333	405.98	18.73
	450	-1.475	666.84	-1.335	401.04	15.23
	500	-1.464	469.58	-1.323	396.89	10.72
4.7	400	-1.485	850.37	-1.350	406.95	19.43
	450	-1.476	708.18	-1.336	403.17	16.18
	500	-1.483	512.01	-1.340	403.19	11.69

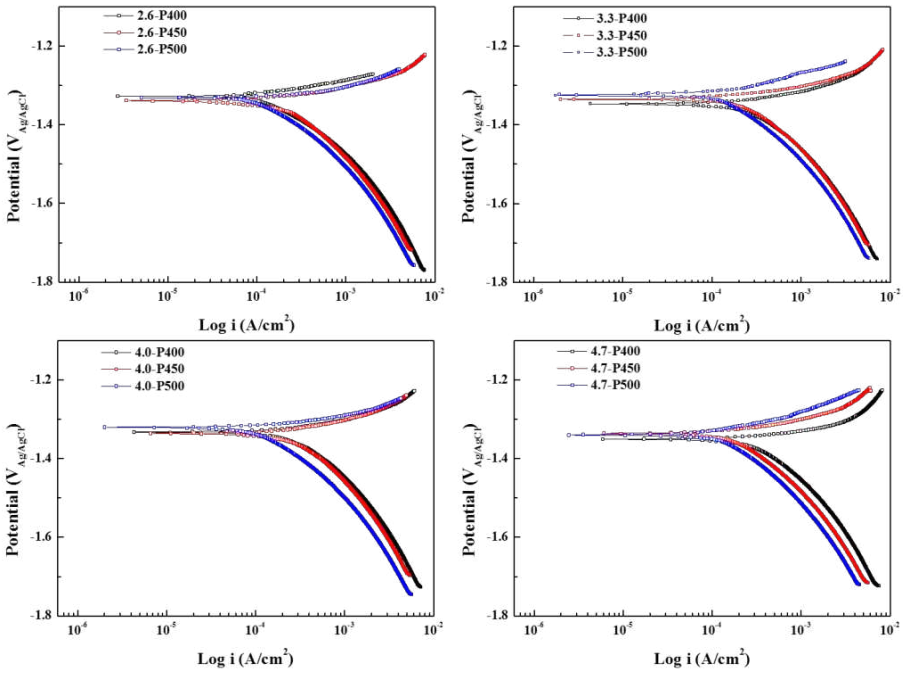

Figure 4. 31 Polarization curves of as-rolled sheets in 3.5 wt. % NaCl solution; (a) 2.6 m/min, (b) 3.3 m/min, (c) 4.0 m/min and (d) 4.7 m/min.

potential. On the other hand, the change in i_{corr} was rather large as can be seen from Table 10. The corrosion current density increased in the order of P500 < P450 < P400 for all casting speeds indicating the samples hot-rolled at higher preheating temperatures have lower corrosion rate. It is obvious the amount of precipitates affected the i_{corr}, which act as a corrosion initiation site. The amount of precipitates found in the samples rolled at higher preheating temperature was less, which led to a decrease in precipitates/matrix interface for galvanic corrosion.

The actual corrosion rates of the as-rolled sheets were measured by immersion test and the results are shown in Fig 4.32. It is noticeable that there is a significant change in corrosion rate compared to the as-cast state. The change in actual corrosion rate was much larger than that of corrosion current density. The corrosion rates calculated by weight loss and hydrogen evolution were both surprisingly high compared to the values reported for this alloy [9]. The corrosion rate increased in the order of P500 < P450 < P400 whereas the casting speeds seems to have very minor effect at this stage. As can be seen from Table 11, the highest corrosion rate was found for the alloy 4.7-P400 which corresponded to P_w of 840.1 mm/year and P_H of 758.7 mm/year. On the other hand, 2.6-P500 had the lowest corrosion rate Pw and PH of 475.2 mm/year and 443.4 mm/year respectively. The general corrosion tendency was in good agreement with the electrochemical tests except for the fact that the alloy actually had much faster corrosion rate compared to the estimated corrosion rate. It should be noted that calculated corrosion rate based on i_{corr} often does not match with actual corrosion rate in case of Mg alloys as the electrochemical test only provides instantaneous measurement [17]. The

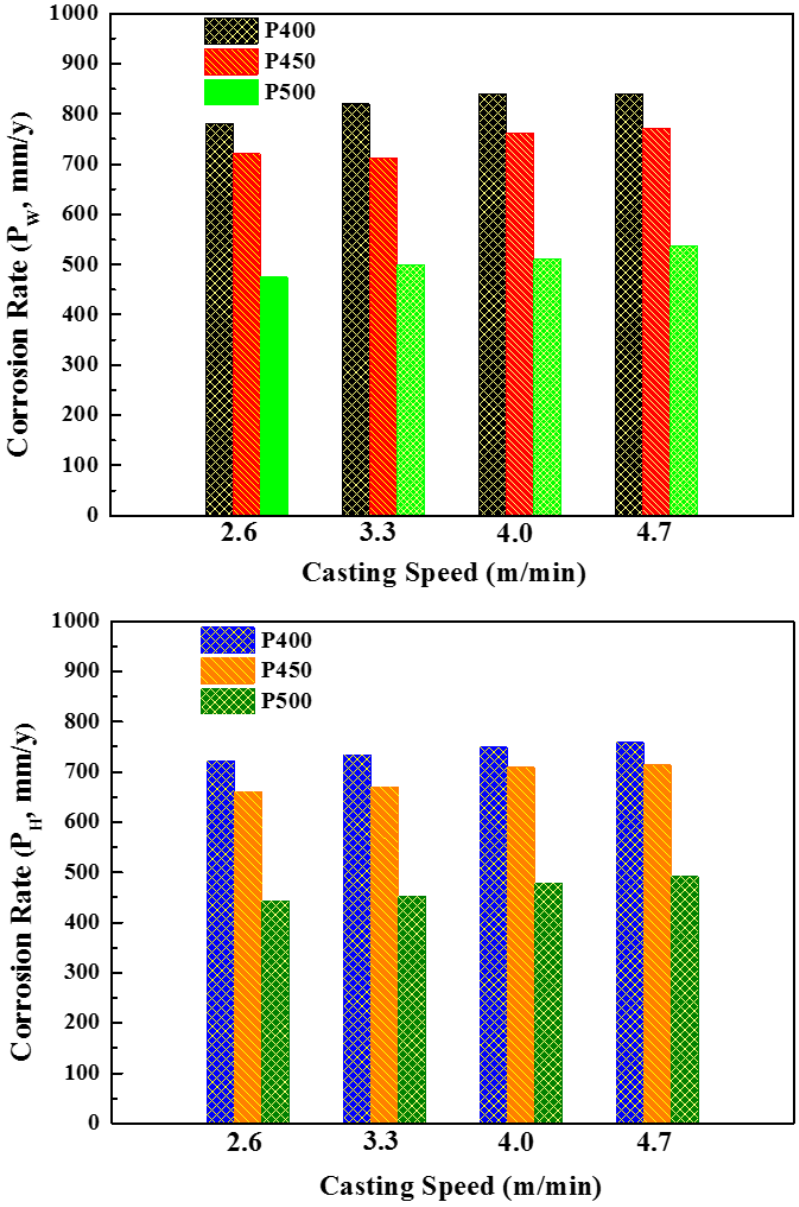

Figure 4. 32 Corrosion rates of as-rolled sheets in 3.5 wt. % NaCl solution based on (a) weight loss and (b) hydrogen evolution.

Table 11 Corrosion rates of as-rolled sheets in 3.5 wt. % NaCl solution based on (a) weight loss and (b) hydrogen evolution.

Casting speed (m/min)	Preheating (°C)	Corrosion rate (mm/year)	
		P_W	P_H
2.6	400	781.9	721.5
	450	721.1	661.5
	500	475.2	443.4
3.3	400	819.5	734.4
	450	712.5	669.8
	500	498.4	452.2
4.0	400	839.8	749.2
	450	761.6	709.2
	500	510.5	478.6
4.7	400	840.1	758.7
	450	771.4	713.5
	500	536.5	492.4

majority of uncoated Mg alloys do not corrode uniformly and the polarization measurements rather provide a indicative of the severity of the corrosion. The extreme corrosion rate of the as-rolled alloy could be attributed to its corrosion behavior. The macroscopic images of corroding as-rolled sample (3.3-P400) in the tested solution are shown in Fig 4.33. The alloy shows exfoliation-type corrosion behavior which is quite rare for Mg alloys. The exfoliation corrosion is a form of inter-granular corrosion reported to occur mainly on cold-rolled Al alloys [18]. In exfoliation corrosion, the corrosion proceeds along the deformed grain boundaries parallel to the surface and corrosion products formed along the boundaries lift up the surface grains. In Mg alloys, the grains boundaries are usually cathodically protected [19]. However, the continuous secondary phase along the grain boundaries are believed to be the reason for this type of corrosion. As can be seen from Fig 4.33 (c), the flake-like corrosion products were continuously formed on the surface. The crack propagation of these corrosion products kept revealing fresh surface to corrosive environment accelerated the corrosion rate. Figure 4.34 shows the cross sectional BSE image of as-rolled (3.3-P400) sample after the immersion test. It can be seen that most precipitates are incorporated inside the corrosion products without dissolution and the EDS mapping (Fig. 4.34 (b, c)) shows some unreacted Mg falls apart even before it corrodes. The corrosion products were very loose and mostly fell apart during the sample preparation. The surface corrosion morphologies of the as-rolled samples after removing the corrosion products are shown in Fig. 4.35. It can be seen that the corrosion is proceeding layer-by-layer leaving thin uncorroded area.

The corrosion behavior of the samples annealed at 350 ^{o}C was also assessed by

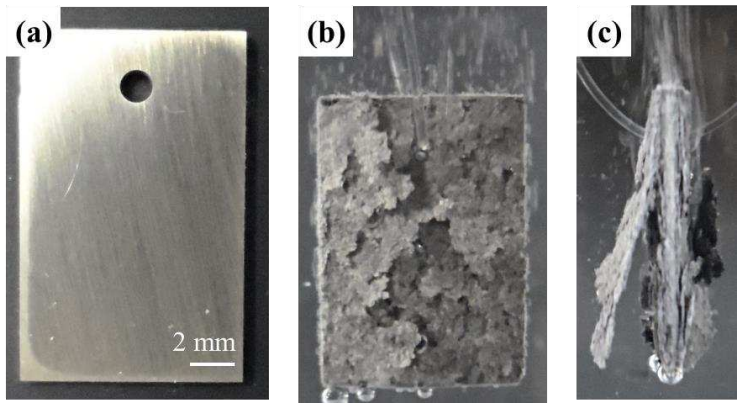

Figure 4. 33 Macroscopic images of 3.3-P400 specimen (a) before immersion and (b, c) during immersion.

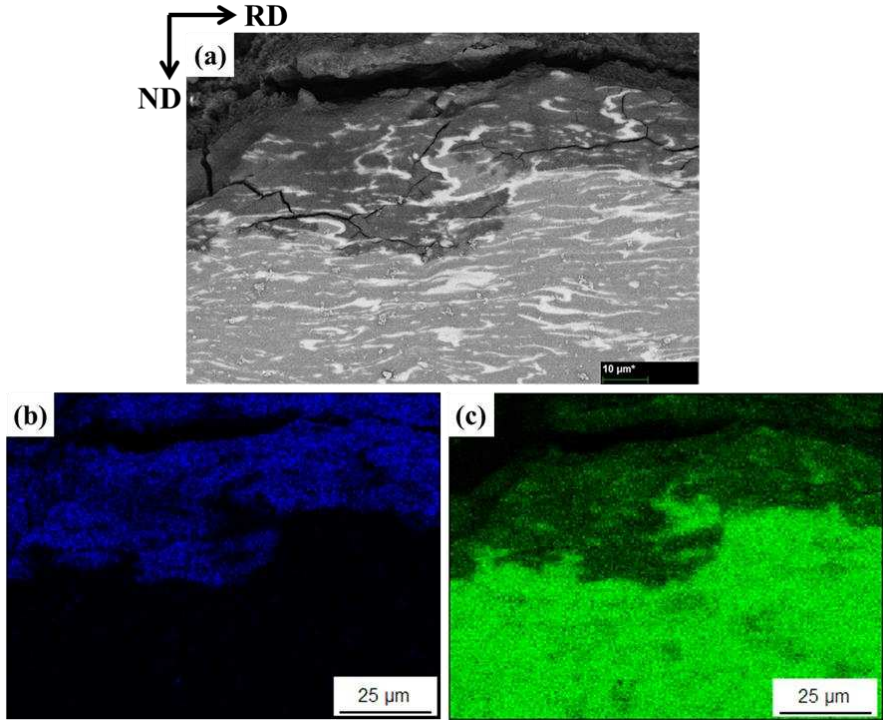

Figure 4. 34 (a) SEM-BSE image of corroded 3.3-P400 and EDS elemental mapping of (b) oxygen and (c) magnesium.

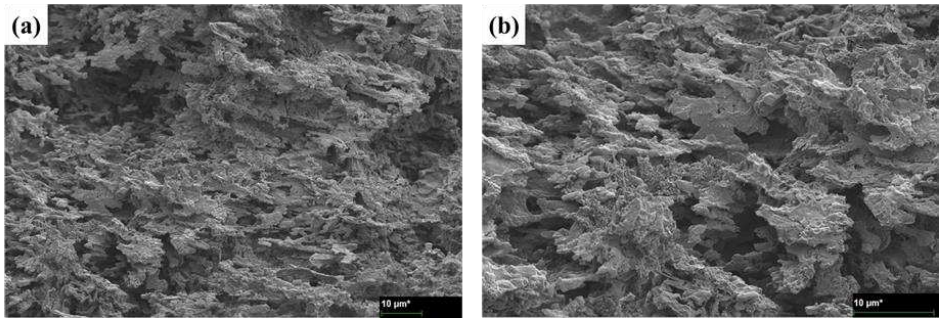

Figure 4. 35 (a, b) SEM images of 3.3-P400 from normal direction after removing the corrosion products.

the same experimental methods used for the as-rolled samples. The results of OCP and polarization measurement are summarized in Table 12 and plotted in Fig. 4.36. For the electrochemical tests, only the strip cast at 3.3 m/min was tested as the effect of casting speeds on corrosion properties was relatively small after the hot-rolling compared to the effect of preheating temperatures. The OCP values for the annealed samples (A350) shows no significant change compared to the measured value at as-rolled state and the values were about the same for all preheating temperatures. This was expected, as the microstructure of the alloy remained relatively unchanged after the annealing as can be seen from Fig 4.25. The polarization measurement result shows that there was a slight increase in E_{corr} similar to the as-rolled sheets. The order of E_{corr} value was again irrelevant to the preheating temperatures. However, the decrease in i_{corr} value was observed in all tested samples. The drop was especially large in case of the sample preheated at 400 ^{o}C (3.3-P400 A350) compared to the as-rolled state.

The corrosion rate based on hydrogen evolution and weight loss method after the immersion tests are shown in Fig. 37 and Table 13. The corrosion rates were much lower than the as rolled state (Fig. 4.32) for all tested samples which agrees with the decrease in i_{corr} in the polarization measurement. The corrosion rates increased in the order of P500 < P450 < P400 although the increment was much smaller compared to the as-rolled state. The effect of casting speeds is hardly noticeable. As discussed earlier, the decrease in corrosion rate was more pronounced for the P400 samples. The samples no longer exhibit the exfoliation-type of corrosion after annealing. Morishige et al. reported that the exfoliation corrosion is not easy to occur at annealed state due

Table 12 Electrochemical properties of hot-rolled sheets annealed at 350 ^{o}C.

Preheating (^{o}C)	Annealing (^{o}C)	OCP ($V_{Ag/AgCl}$)	i_{corr} ($\mu A/cm^2$)	E_{corr} ($V_{Ag/AgCl}$)	b_c (mV dec^{-1})	P_i (mm/year)
400	350	-1.471	534.86	-1.333	401.56	12.20
450		-1.478	496.52	-1.333	392.07	11.33
500		-1.469	414.98	-1.332	382.30	9.46

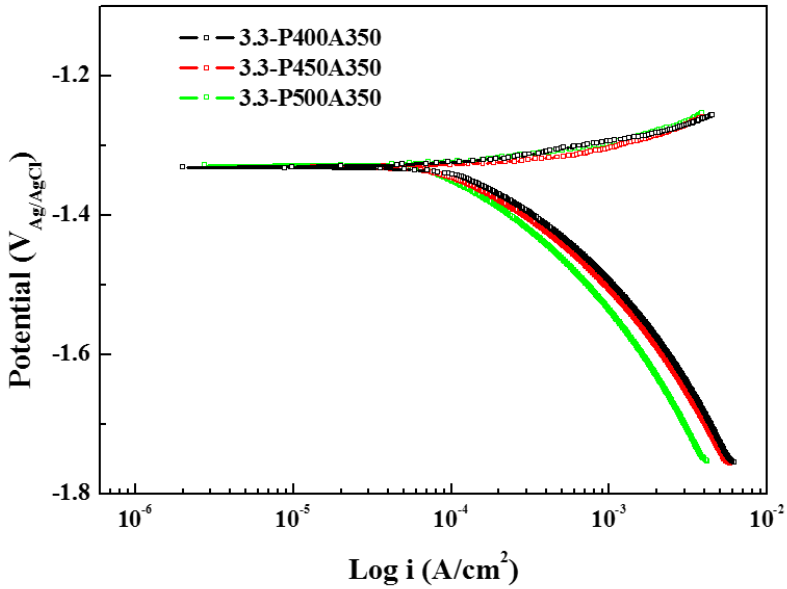

Figure 4. 36 Polarization curves of hot-rolled sheets annealed at 350 ^{o}C in 3.5 wt. % NaCl solution.

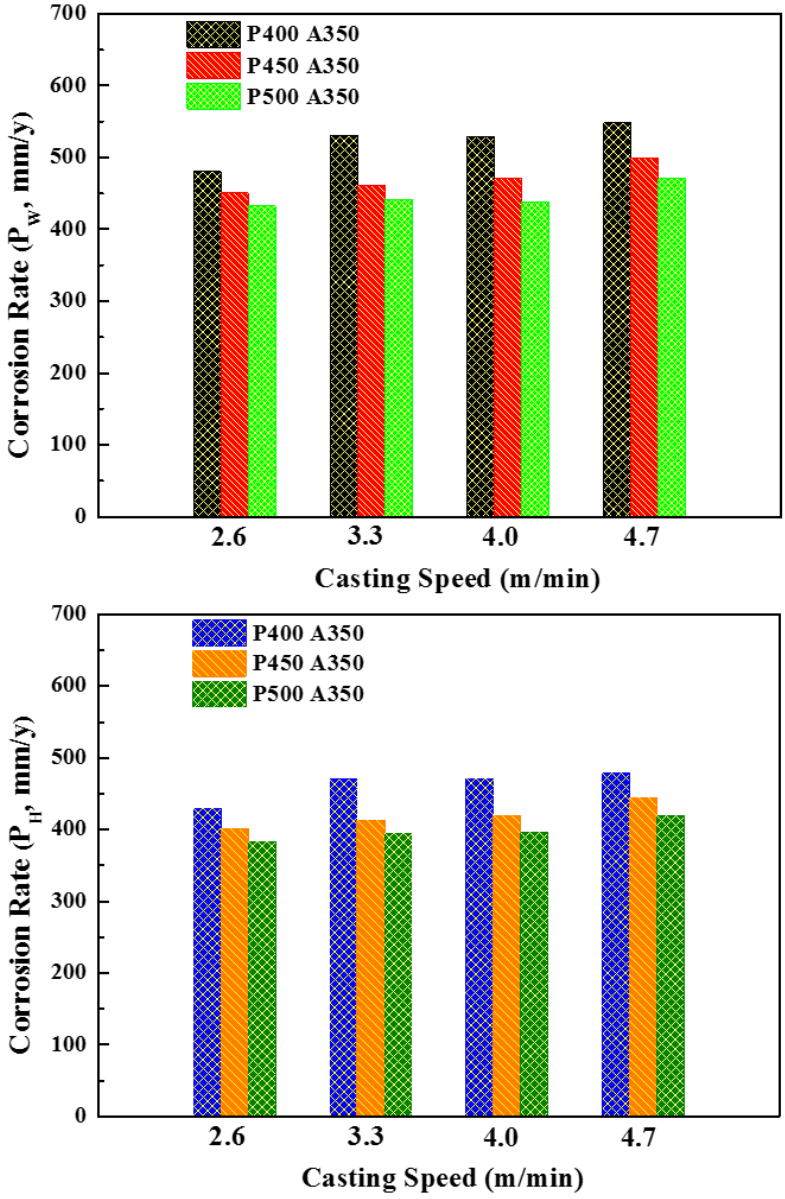

Figure 4. 37 Corrosion rates of hot-rolled sheets annealed at 350 ^{o}C in 3.5 wt. % NaCl solution based on (a) weight loss and (b) hydrogen evolution.

Table 13 Corrosion rates of hot-rolled sheets annealed at 350 ^{o}C in 3.5 wt. % NaCl solution based on (a) weight loss and (b) hydrogen evolution

Casting speed (m/min)	Preheating (^{o}C)	Corrosion rate (mm/year)	
		P_W	P_H
2.6	400	480.5	429.6
	450	450.7	401.1
	500	432.5	382.9
3.3	400	530.2	469.8
	450	461.8	413.3
	500	441.4	394.8
4.0	400	529.8	471.2
	450	470.4	419.6
	500	438.8	395.5
4.7	400	548.2	478.8
	450	498.9	444.5
	500	470.5	418.7

to the removal of residual stress through the thickness direction [20].

Although the annealing at 350 ^{o}C showed a marked decrease in corrosion rates, the values obtained up to this point are still too high compared to the numbers reported by the others [21]. The hot-rolled samples were put into further high temperature annealing to find out whether it produce better corrosion properties close to the reported values. The results of electrochemical test for the hot-rolled samples annealed at 500 ^{o}C and 550 ^{o}C (A500, A550) are shown in Fig. 4.38 and summarized in Table 14. The experiments were conducted with the sample cast at 3.3 m/min as the samples showed the best mechanical properties overall and the effect of casting speed in corrosion properties was relatively insignificant. As can be seen from Table 14, the measured OCP for A500 samples are still in very close range with the previously mentioned samples suggesting similar corrosion susceptibility. However, the measured i_{corr} was much smaller than the samples annealed at 350 ^{o}C. The decreased current densities most likely originates from the reduced second phase. It should be also noted that the corrosion current density difference in accordance with the preheating temperatures are now much smaller due to the comparable amount of precipitates between the samples. As previously discussed, the large electrochemical potential difference between the precipitates and the α-Mg initiates galvanic corrosion and the reduced interface between the two phases resulted in lower i_{corr}. It is also possible that the homogeneous microstructures of recrystallized grains formed more uniform passive films that inhibits the corrosion attack. When the annealing temperature was raised to 550 ^{o}C, the OCP finally shows a difference. The OCP shifted towards negative potential, which means that the samples are now even more thermodynamically unstable

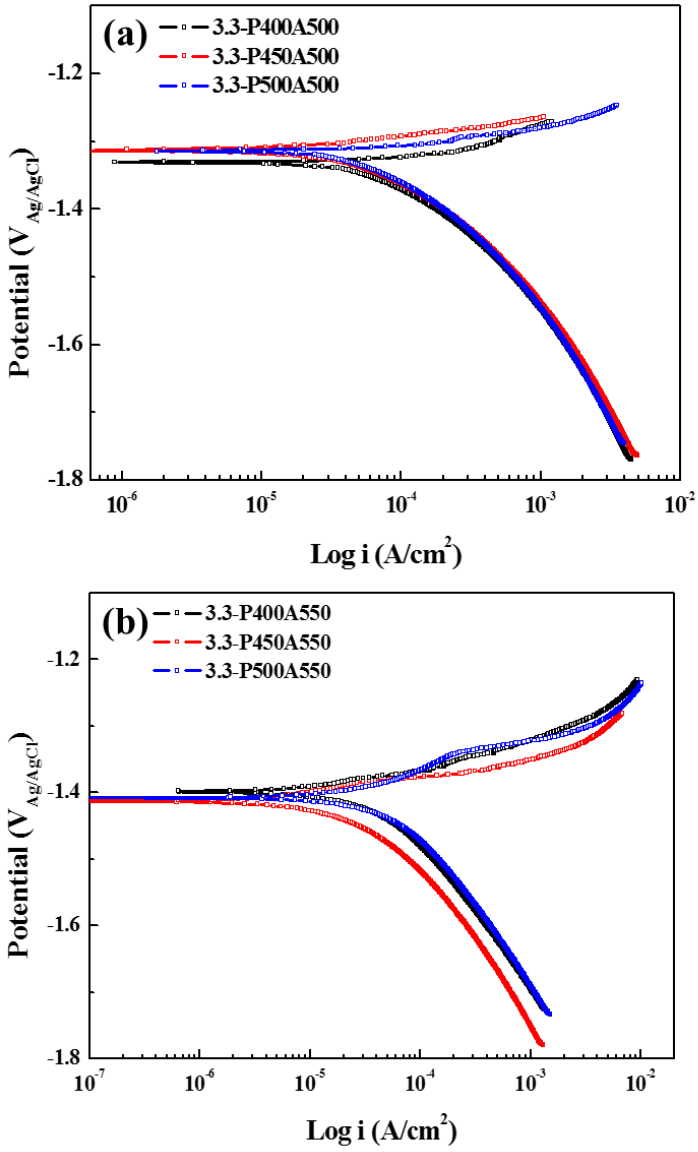

Figure 4. 38 Polarization curves of hot-rolled sheets annealed at (a) 500 ^{o}C and (b) 550 ^{o}C in 3.5 wt. % NaCl solution.

Table 14 Electrochemical properties of hot-rolled sheets annealed at (a) 500 ^{o}C and (b) 550 ^{o}C in 3.5 wt. % NaCl solution.

Preheating (°C)	Annealing (°C)	OCP ($V_{Ag/AgCl}$)	i_{corr} ($\mu A/cm^2$)	E_{corr} ($V_{Ag/AgCl}$)	b_c (mV dec^{-1})	P_i (mm/year)
400	500	-1.461	327.37	-1.328	402.26	7.48
450		-1.454	282.53	-1.313	379.93	6.46
500		-1.457	280.81	-1.314	382.46	6.42
400	550	-1.484	74.025	-1.401	286.70	1.69
450		-1.486	60.448	-1.412	245.16	1.38
500		-1.479	67.245	-1.407	260.05	1.54

and prone to corrosion. Also, the change in polarization behavior can be seen from Fig. 4.38 (b). There were clear breakdown potentials (E_b) in all preheating temperatures. The corrosion densities decreased to about 50% of the A500, due to the reduced cathodic kinetics.

The corrosion rate of A500 and A550 alloys based on hydrogen evolution rate and weight loss during the immersion tests are shown in Fig. 4.39 and Fig. 4.40 and the results are summarized in Table 15. As expected, the corrosion rate decreased in the A500, although not to the extent suggested by the large change in i_{corr} from the electrochemical tests. It seems reasonable to assume that the annealing temperature of 500 ^{o}C does not allow further dissolution of the precipitates and the corrosion kinetics is still dominated by the micro-galvanic couple between the precipitates and the matrix. However, there are drastic changes in corrosion rate when the annealing temperature is raised to 550 ^{o}C. The lowest corrosion rate measured for A550 was P_w of 6.8 mm/year and P_H of 5.8 mm/year (3.3-P450 A550). At this state, the corrosion rates of the samples were almost equalized and all the tested condition showed very low corrosion rated compared to the previous results. Obviously, this is due to the dissolution of precipitates that were forming strong galvanic couple with the matrix.

The corrosion morphologies of the annealed samples (A350, A500, A550) were compared to see the degradation behavior of the alloys. Figure 4.41. shows the surface morphologies of corroded samples after 3 hr of immersion. The surfaces of the 3.3-P400A350 (Fig. 4.41 (a,b) and the 3.3-P500A500 (Fig. 4.41 (c,d)) were covered with rose-like corrosion products. The corrosion products were very loosely attached with porous structure. On the other hand,

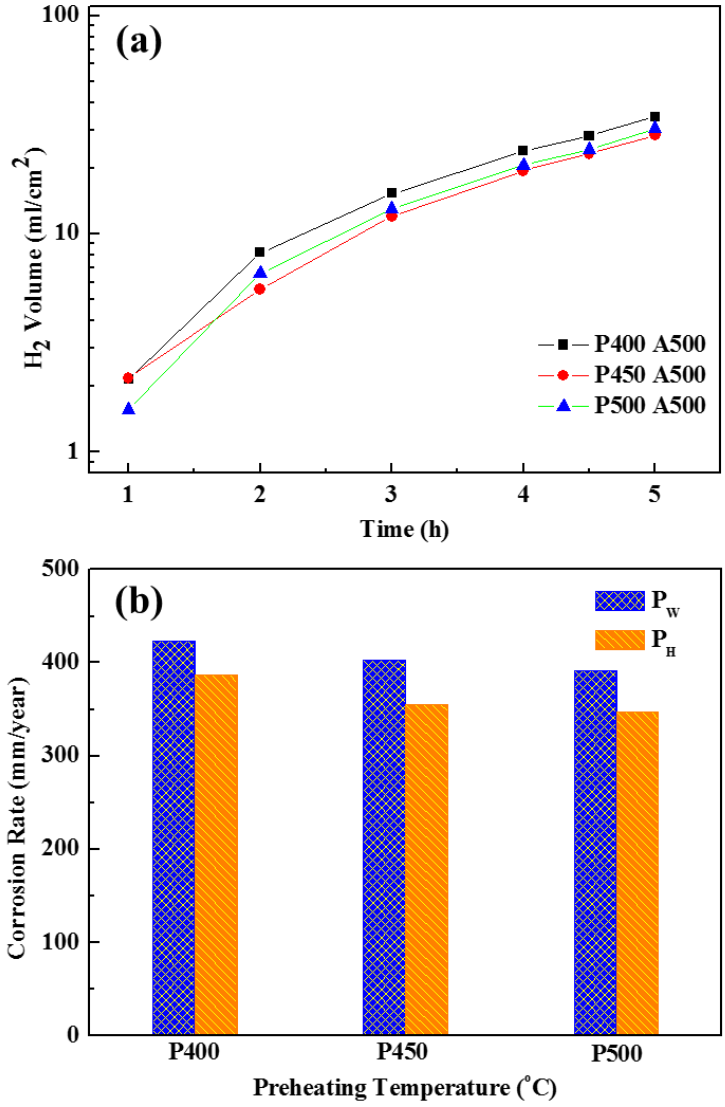

Figure 4. 39 (a) Hydrogen evolution and (b) corrosion rates of hot-rolled sheets annealed at 500 °C in 3.5 wt. % NaCl solution.

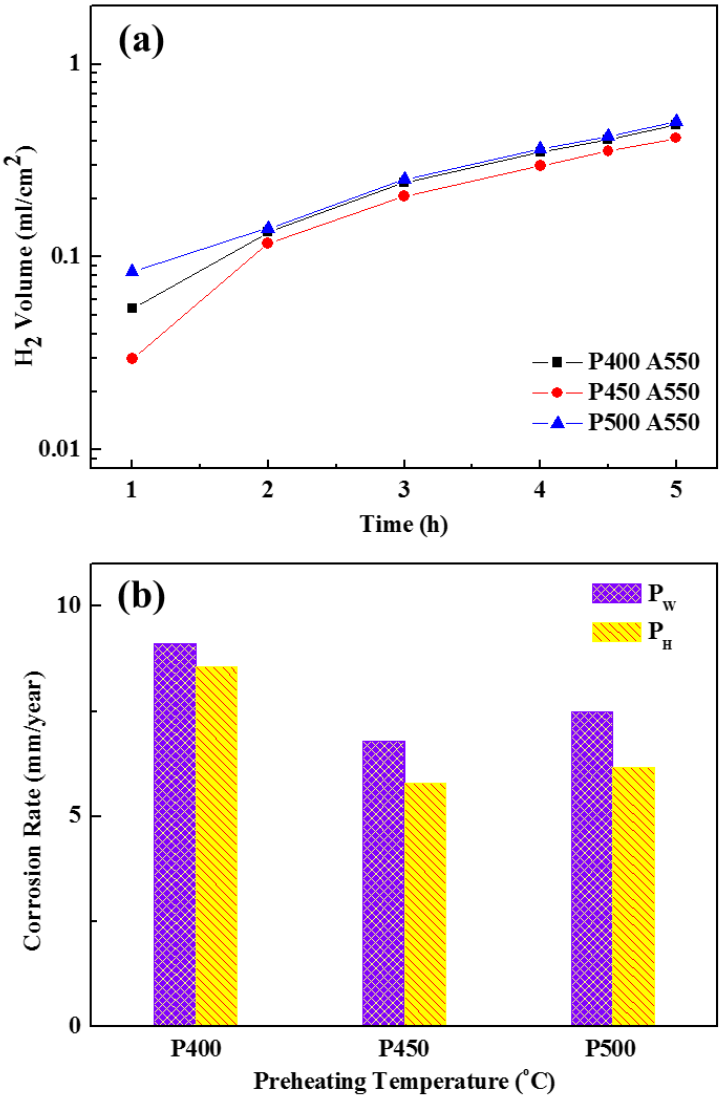

Figure 4. 40 (a) Hydrogen evolution and (b) corrosion rates of hot-rolled sheets annealed at 550 °C in 3.5 wt. % NaCl solution.

Table 15 Corrosion rates of hot-rolled sample annealed at 500 ^{o}C and 550 ^{o}C in 3.5 wt. % NaCl solution.

Casting speed (m/min)	Preheating (^{o}C)	Annealing (^{o}C)	Corrosion rate (mm/year)	
			P_W	P_H
3.3	400	500	423.12	387.33
	450		402.52	355.87
	500		392.05	347.51
	400	550	9.12	8.56
	450		6.80	5.83
	500		7.51	6.17

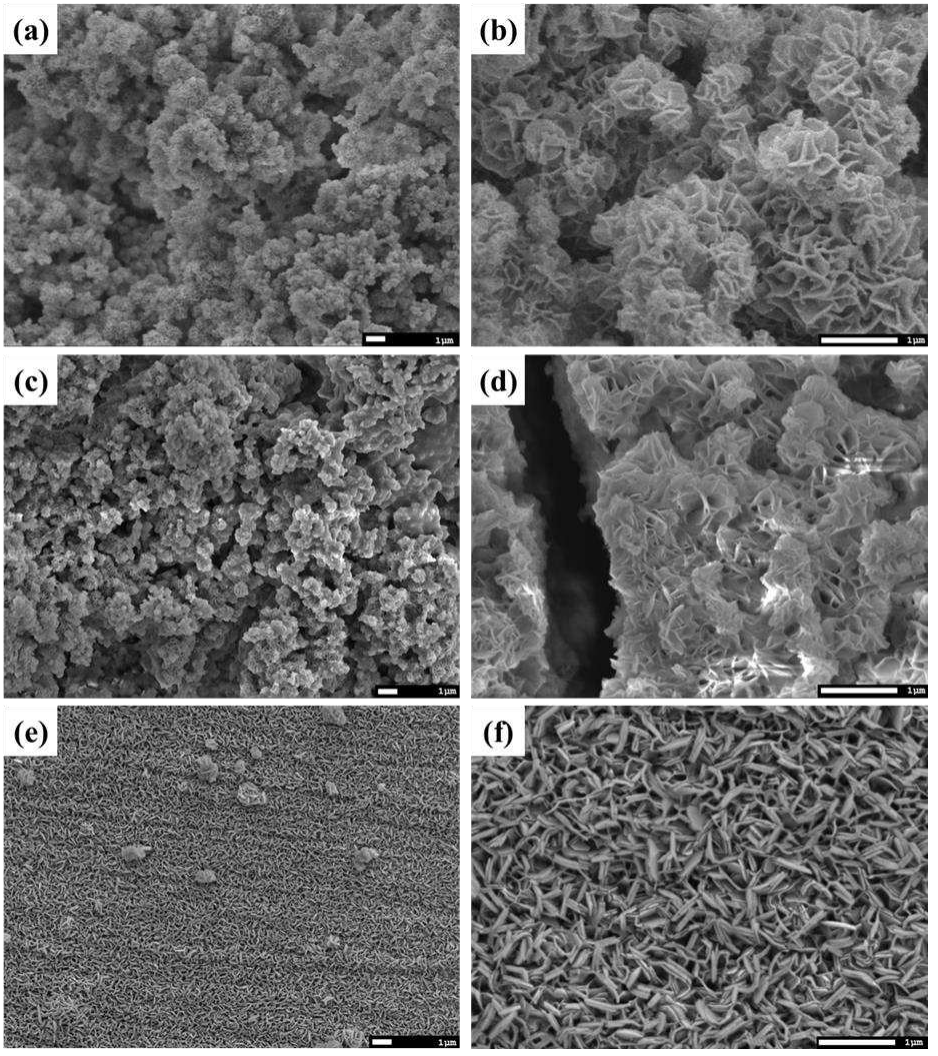

Figure 4. 41 SEM images of annealed samples after immersion tests from normal direction; (a) P400A350, (b) P500A500 and (c) P500A550.

the corrosion products formed on the 3.3-P500A550 (Fig. 4.41 (e,f)) had gypsum flower-like morphology similar to the corrosion products observed in the as-cast samples. These corrosion products were much dense and more compact compared to the 3.3-P400A350 and 3.3-P500A500, which could have provided better protection from the corrosive environment. The corrosion morphologies after removing the corrosion products are shown in Fig. 4.42. It can be seen that the corrosion proceeds along the precipitates in the 3.3-P400A350, which is also visible in the cross-sectional image in Fig. 4.43. The surface obtained for the 3.3-P400A500 had globular morphologies. The lightly etched cross-sectional image revealed that the corrosion progresses grain by grain (Fig. 4.43 (b)). The grains rapidly corroded once the grain boundaries are damaged and the matrix was revealed to the corrosive environment. On the other hand, the corroded surface of 3.3-P500A550 (Fig. 4.42 (e,f), Fig. 4.43 (c)) shows uniform corrosion morphology and the surface was smooth even at high magnification. There was no sign of localized corrosion due to the absence of the secondary phase which proves its good corrosion resistance.

4.3 Hot-rolling of solution heat-treated strips

As discussed in earlier chapters, the hot-rolled strips showed poor corrosion resistance of more than P_w = 800 mm/year despite having a good mechanical property. This was mainly due to the inter-dendritic precipitates ($Mg_{12}YZn$) present prior to the hot-rolling, which eventually developed into the inter-granular precipitates causing severe micro-galvanic corrosion with the α-Mg. The previous studies on Mg-2Y-1Zn (at. %) alloy demonstrated its excellent mechanical property as well as a reasonable corrosion rate [21]. The TRC cast

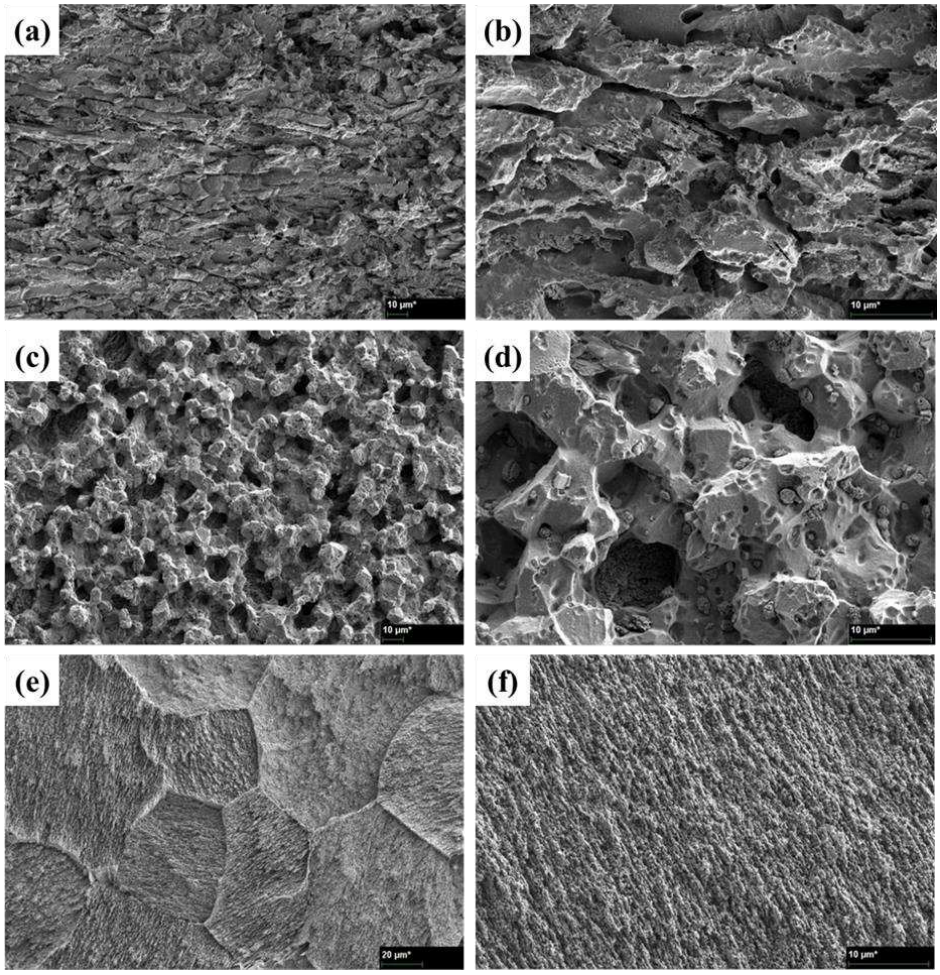

Figure 4. 42 SEM images of annealed samples after immersion tests without corrosion products from normal direction; (a) P400A350, (b) P500A500 and (c) P500A550.

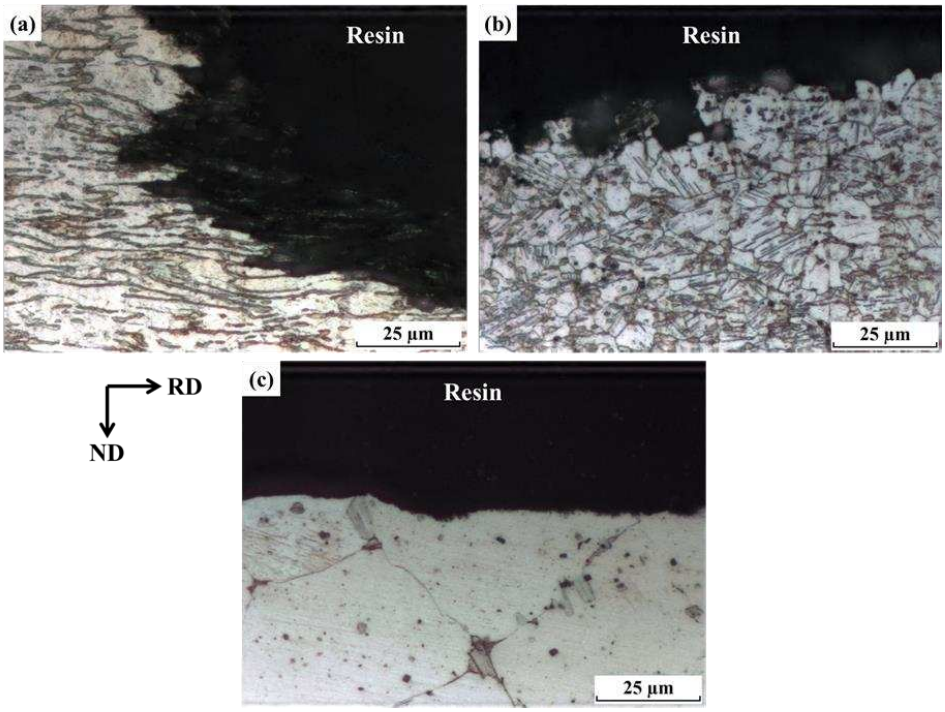

Figure 4. 43 Cross sectional micrographs of the annealed samples after immersion tests without corrosion products; (a) P400A350, (b) P500A500 and (c) P500A550.

and hot-rolled samples in this study also exhibited a comparable corrosion rate of P_w = 6.8 mm/year at high temperature annealed condition but the strength deteriorated significantly due to the excessive grain growth and lack of second phase particles. Thus, an alternative processing route was attempted to find the optimum process parameters in terms of both mechanical and corrosion properties.

4.3.1 Microstructure

The optical micrograph of solution heat treated and furnace cooled TRC strip from the normal direction are shown in Fig. 4.44. All the experiments in this chapter was conducted with the strip cast at 3.3 m/min since it had the best mechanical property. It can be seen from the figure that the inter-dendritic phase are no longer visible and the fine lamellar phase is formed across the grains. The lamellar phase is most likely the lamellar LPSO which has been observed in the previous section. The microstructures of as-rolled strips from the normal direction are shown in Fig. 4.45. The lamellar LPSO phase is still covering most of the sample although some absent areas were observed randomly. The grain size was hard to determine by the optical microscope due to the lamellar phase but some recrystallized grains with different lamellae orientation were clearly visible in some area Fig. 4.45 (b). The BSE image of as-rolled sample (Fig. 4.46) shows that the bulk precipitates are also present around the lamellae. These precipitates were confirmed to be the $Mg_{12}YZn$ by the EDS analysis (Fig. 4.46 (e)). Prior to the hot-rolling, these second phase were not visible indicating that these were formed by the repeated heating and cooling during the hot-rolling process. The lamellar phase was rich in Y and Zn compared to the matrix and as the atomic ratio is close to 1:1 (Fig 4.46 (d)), it

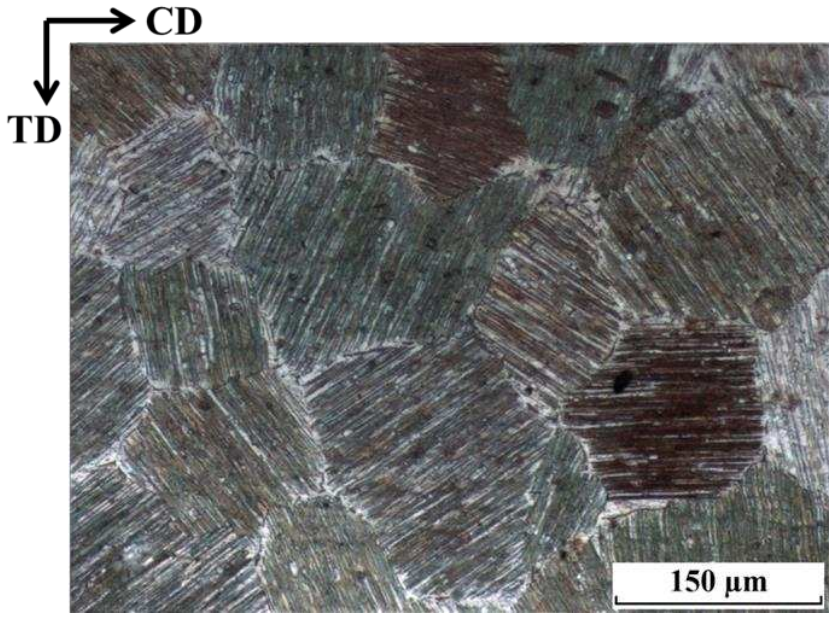

Figure 4. 44 Optical micrograph of solution heat-treated TRC strip from normal direction

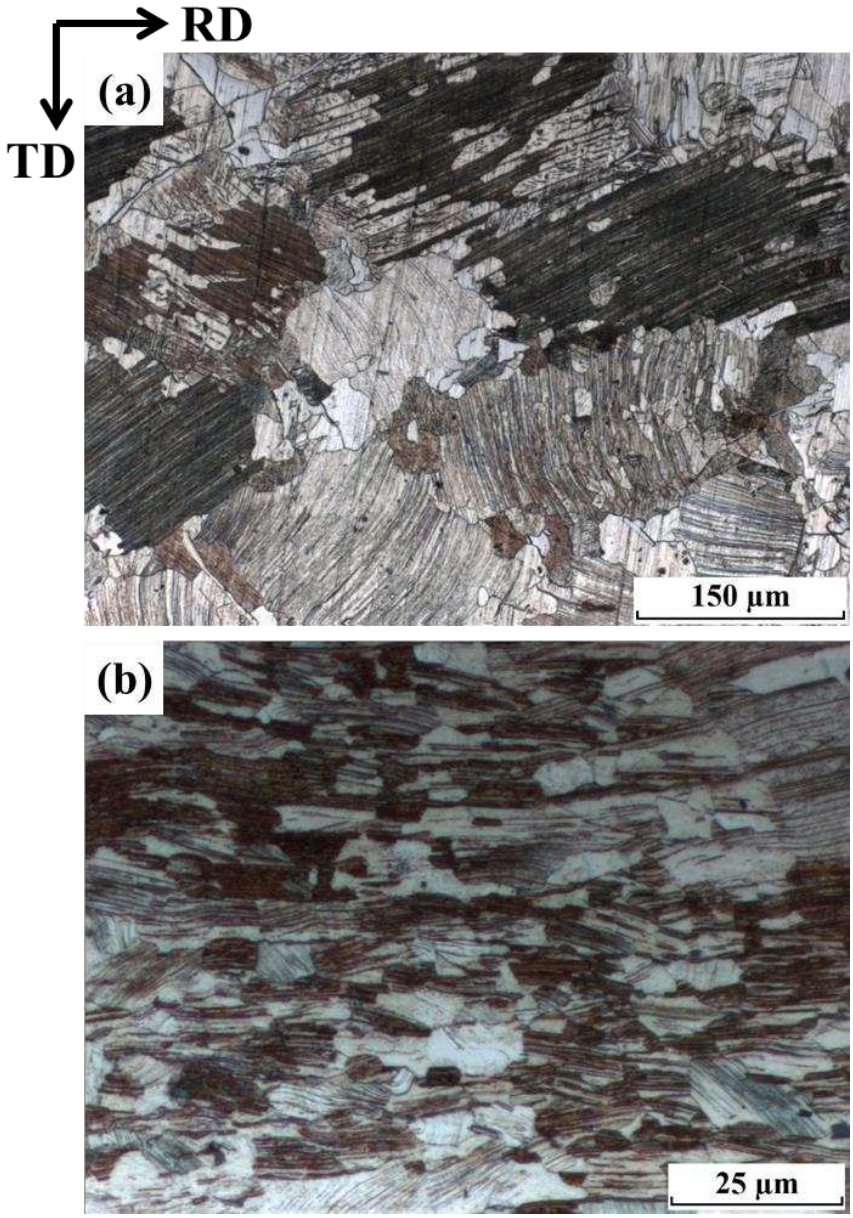

Figure 4. 45 (a) Optical micrographs of solution heat-treated and hot-rolled sheet (SH-P500) from normal direction and (b) recrystallized region.

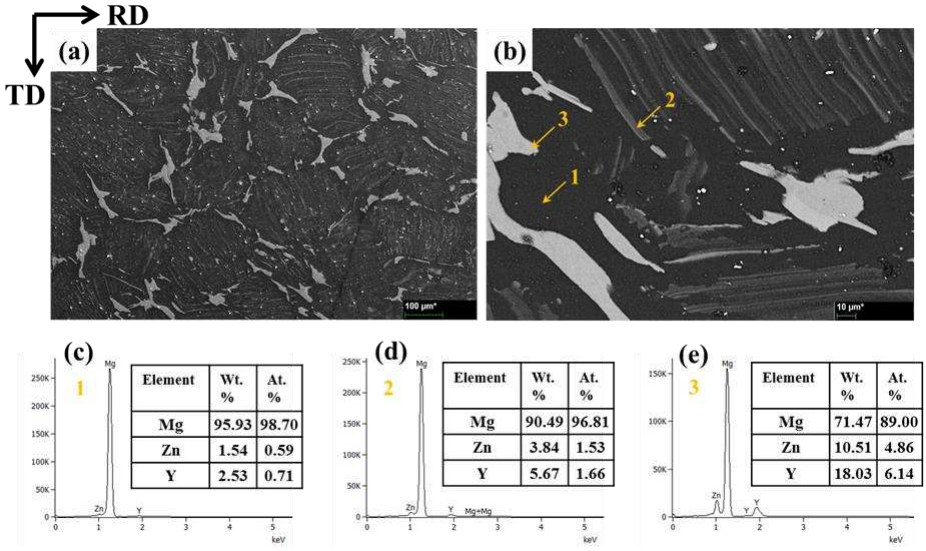

Figure 4. 46 (a, b) SEM-BSE images of solution heat-treated and hot-rolled sheet (SH-P500) and (c, d, e) EDS analysis.

is also believed to be the $Mg_{12}YZn$ phase as discussed in the previous chapter.

4.3.2 Mechanical properties

The stress-strain curves of solution heat-treated and hot-rolled samples (SH-P500, SH-P500A350) at room temperatures are shown in Fig. 4.47 and the tensile properties are summarized in Table 16. The tensile behavior and properties of homogenized and hot-rolled samples (P500, P500A350) are also plotted for comparison. The YS and UTS of the SH-P500 were slightly lower than that of P500. Although there was a large difference in microstructure, the strengths of the two samples turned out to be similar. The solution heat-treated samples however, did show a lower ductility due to the dense lamellar precipitates as reported by Xu et al [22]. After 1 hr of annealing at 350 ^{o}C, the ductility increased at the expense of strength and the curve almost coincide with the curve of P500A350. This most likely resulted from partial recovery although no significant change in microstructure was observed. Overall, the different hot-rolling processes did not show much of a difference in terms of mechanical properties. However, hot-rolling of solution heat-treated samples at other preheating temperature could have produced better mechanical properties, considering the precipitation of bulk $Mg_{12}YZn$ phase during the hot-rolling. The fine lamellar phase are reported to be more efficient in improving the strength and hot-rolling at lower preheating temperature might have prevented the dissolution of lamellar phase and the precipitation of bulk $Mg_{12}YZn$.

4.3.3 Corrosion properties

The corrosion behavior of the post solution heat-treated samples was analyzed by the electrochemical test and the immersion test. The results of

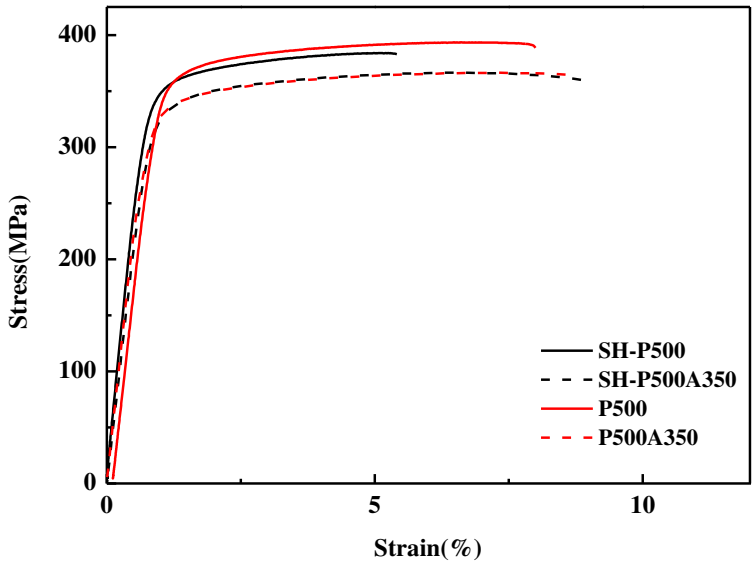

Figure 4. 47 Stress-strain curves of SH samples plotted with P500 and P500A350.

Table 16 Tensile properties of SH samples compared with P500 and P500A350.

Casting Speed (m/min)	Identifier	Y.S. (MPa)	U.T.S. (MPa)	Elong. (%)	Unif. El. (%)	S.H.E n
3.3	SH-P500	340.1	383.8	4.6	4.3	0.082
	SH-P500A350	320.9	365.8	8.5	6.6	0.084
	P500	349.2	393.4	7.0	5.6	0.081
	P500A350	318.6	366.3	7.9	6.5	0.082

electrochemical test are shown in Fig. 4.48 and summarized in Table 17. The OCP curves showed slow increase up to around 1500 s indicating the formation of surface films. The polarization curves of SH-P500A350 and SH-P500 are plotted in Fig 4.48. along with the P500 and P500A350 for comparison. Again, the i_{corr} was determined by the extrapolation of steepest part of the cathodic curves. The measured E_{corr} was about 80 mV higher than the OCP value for SH-P500 and SH-P500A350. The two samples showed similar polarization curves indicating their close corrosion behavior. The SH-P500A350 showed slightly higher i_{corr} due to the increased cathodic kinetic compared to the SH-P500A350. It is also apparent that the corrosion behavior greatly change compared to the P500 and P500A350. The cathodic slope decreased and the cathodic curve showed a large shift towards lower current densities which resulted in much lower i_{corr} for the solution heat-treated samples. On the other hand, the anodic branch showed little change over the different process.

The EIS spectra was also measured for the SH-P500 and SH-P500350 for better understanding of corrosion properties. The Nyquist plot is shown in Fig. 4.49 along with the P500 and P500A350 for comparison. All the plots comprised of a capacitive loop at mid-high frequency range followed by an inductive loop at low frequency region. The mid-high frequency loop is usually related to the charge transfer resistance and it can be seen from Fig. 4.49 that the SH-P500 and SH-P500A350 have much larger semicircle radius implying better corrosion resistance of SH samples. The low frequency regions indicate the presence of adsorbed surface ions and possible local corrosion taking place at the surface. The experimental data was fitted with simple

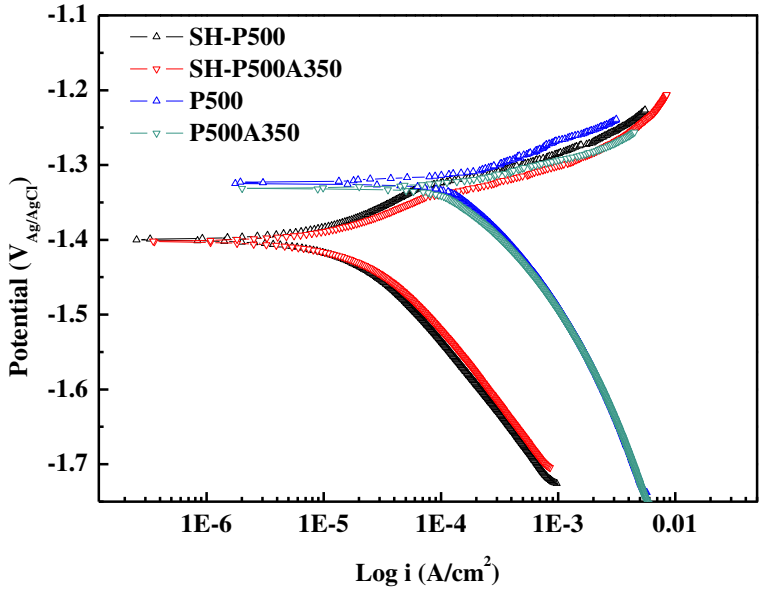

Figure 4. 48 Polarization curves of SH samples, P500, P500A350 in 3.5 wt. % NaCl solution.

Table 17 Electrochemical properties of SH samples, P500 and P500A350 in 3.5 wt. % NaCl solution

Casting speed (m/min)	Identifier	OCP ($V_{Ag/AgCl}$)	i_{corr} ($\mu A/cm^2$)	E_{corr} ($V_{Ag/AgCl}$)	b_c (mV dec^{-1})	P_i (mm/year)
3.3	SH-P500	-1.485	24.364	-1.400	207.55	0.56
	SH-P500A350	-1.489	28.853	-1.402	209.32	0.66
	P500	-1.468	472.02	-1.330	397.11	10.79
	P500A350	-1.437	414.98	-1.332	382.30	9.48

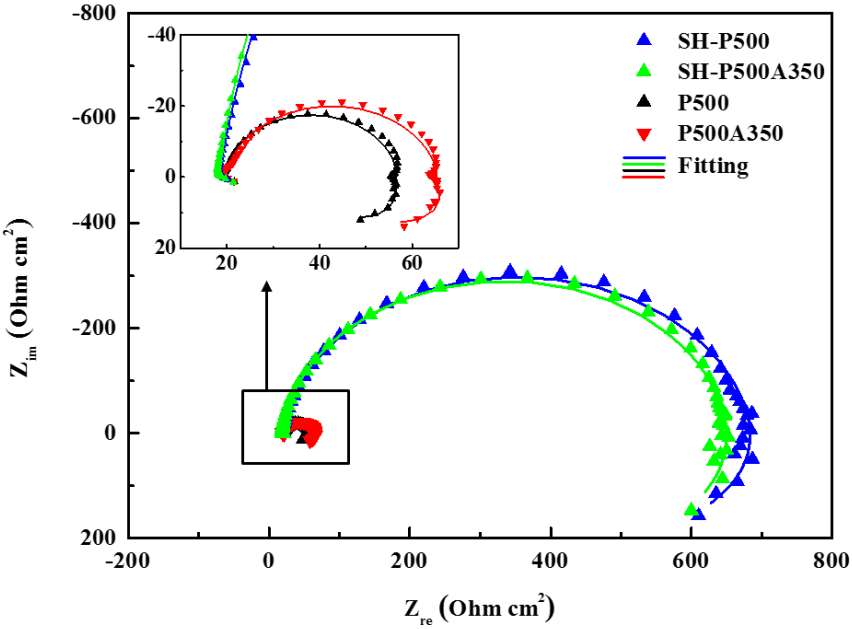

Figure 4. 49 Nyquist plots of SH samples, P500 and P500A350 in 3.5 wt. % NaCl solution.

equivalent circuit shown in Fig. 4.50 using ZSimpWin software and the fit result is shown in Table18. In the circuit, R_S represents the resistance of tested solution. CPE_{dl} stands for the electric double layer capacity, whereas R_{ct} represents the charge transfer resistance. The constant phase element (CPE_{dl}) was used instead of a capacitor to compensate the inhomogeneity of the system, which appear as depressed semicircles as a result of non-uniform and unstable electrode surface causing frequency dispersion during the measurement. The capacitance of CPE element is defined by the two elements Y_{dl} and n_{dl}. When $n_{dl} = 1$, CPE_{dl} behaves as a capacitor and as a resistor when $n_{dl} = 0$. An inductor and an associated resistor, denoted as L and R_L respectively, were also added to represent the inductive response at the low frequency region. In general, R_{ct} is related to a charge transfer rate and a surface film property that reflect the dissolution rate of the alloy. Compact or dense surface films have large R_{ct} whereas the CPE_{dl} defines the thickness of the films [4]. It can be seen from Table 18 that the solution heat-treated sample SH-P500 and SH-P500A350 have much higher R_{ct} compared to the homogenized sample. Thus, it can be inferred that the SH-P500 and SH-P500A350 would have much better corrosion resistance as a result of compact and thick surface films which is also in good agreement with the results from potentiodynamic polarization measurements.

The hydrogen evolution rates of immersed SH-P500 and SH-P500A350 are shown in Fig. 4.51. After 10 hr of immersion, the collected hydrogen was 0.482 ml/cm^2 and 0.754 ml/cm^2 for SH-P500 and SH-P500A350 respectively. The calculated corrosion rates based on hydrogen evolution rate and weight loss methods are shown in Fig. 4.52 and summarized in Table 19 for

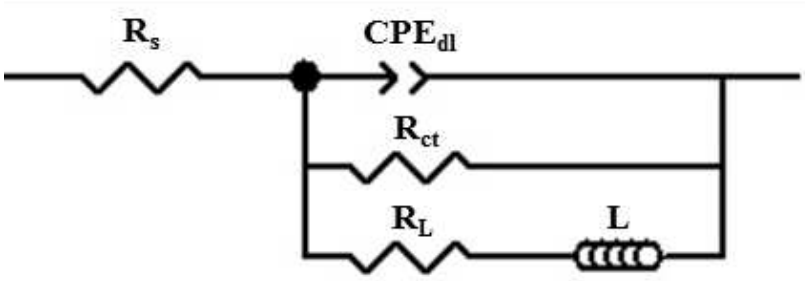

Figure 4. 50 Equivalent circuit model used to fit EIS spectra.

Table 18 Fitting results for the EIS spectra.

Casting speed (m/min)	Identifier	R_S ($\Omega \cdot cm^2$)	CPE_{dl}		R_{ct} ($\Omega \cdot cm^2$)	L ($H \cdot cm^2$)	R_L ($\Omega \cdot cm^2$)
			Y_{dl} ($\mu\Omega^{-1} \cdot cm^{-2} \cdot s^{-1}$)	n_{dl}			
3.3	SH-P500	18.31	14.15	0.94	672.8	5129	539.8
	SH-P500A350	18.41	13.85	0.93	650.4	4985	398.7
	P500	19.55	45.51	0.92	45.39	148.8	13.52
	P500A350	19.43	43.27	0.95	37.13	202.6	14.81

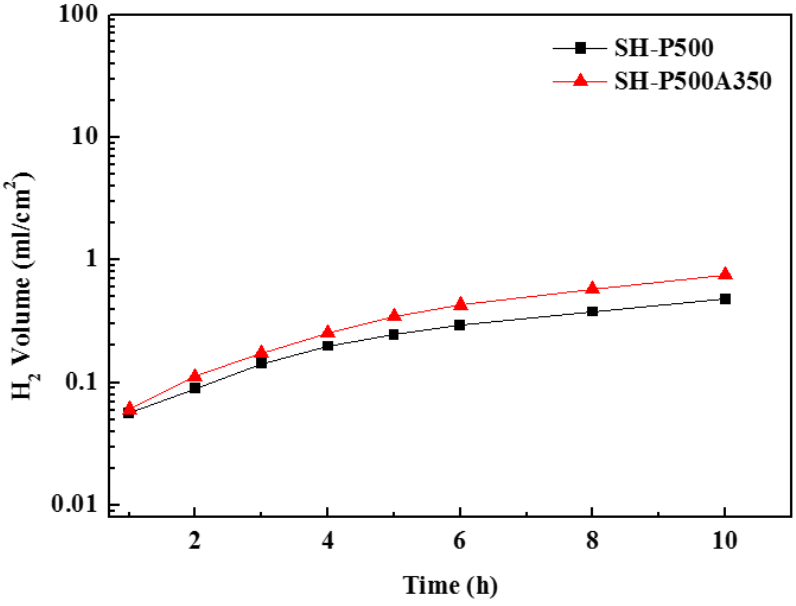

Figure 4. 51 Hydrogen evolution of SH samples in 3.5 wt. % NaCl solution.

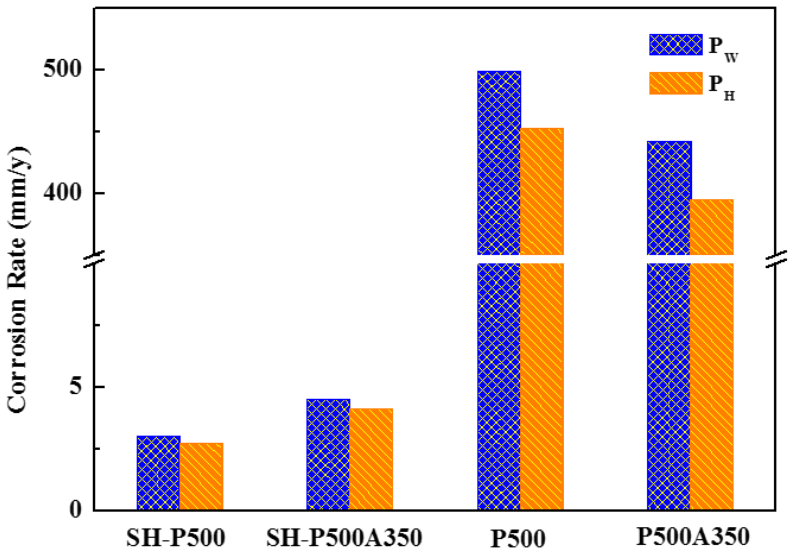

Figure 4. 52 Corrosion rates of SH samples, P500 and P500A350 based on weight loss and hydrogen evolution in 3.5 wt. % NaCl solution.

Table 19 Corrosion rates of SH samples, P500 and P500A350 based on weight loss and hydrogen evolution in 3.5 wt. % NaCl solution.

Casting speed (m/min)	Identifier	Corrosion rate (mm/year)	
		P_W	P_H
3.3	SH-P500	3.02	2.73
	SH-P500A350	4.51	4.13
	P500	498.4	452.2
	P500A350	441.4	394.8

comparison with P500 and P500A350. The SH-P500 showed slightly better corrosion resistance than the SH-P500A350 but this might be due to the short test period considering the fact that the electrochemical test suggests very similar corrosion behavior between these samples. On the other hand, it can be seen that the corrosion resistance was improved drastically compared to the P500 and P500A350 by the solution heat-treatment prior to the hot-rolling. That is more than 99% reduction in corrosion rate from 498.4 mm/year to 3.02 mm/year by P_w which is remarkable.

The surface potential distribution of SH-P500 was analyzed by SKPM mapping (Fig. 4.53). The result shows the potential difference between the precipitates (dark area) and the α-Mg (bright area). As mentioned earlier, the SKPM measures the potential difference between the samples surface and the cantilever tip (Cr-Au). Thus, the higher potential in the figure indicates less noble state which is the α-Mg in this case. It suggests these two phases still form a galvanic couple, as the precipitates are nobler than the α-Mg.

The corroded surface of SH-P500 after the immersion was examined by the SEM. The surface was covered with dense corrosion products after 3 hr of immersion as illustrated in Fig. 4.54. The higher magnification shows its gypsum flower-like morphology that is similar to the corrosion products formed on P500A550. The cross sectional image of corroded SH-P500 with and without the corrosion products are presented in Fig. 4.55 and Fig. 4.56. It can be seen that the corrosion is uniform across the surface although there is strong galvanic coupling between the precipitates and the α-Mg. Also, the EDS mapping (Fig. 4.55 (c,d)) shows that the oxygen layer or the corrosion product is denser and more compact than the P500 (Fig. 4.34 (b)), suggesting better

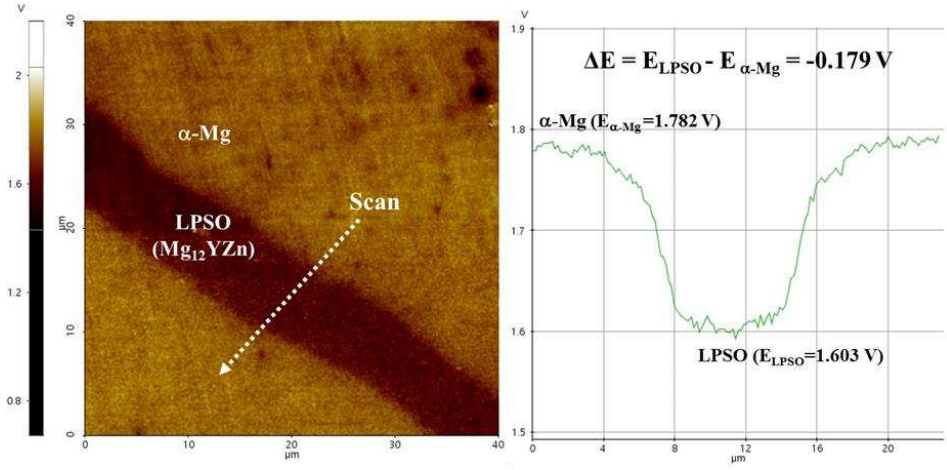

Figure 4. 53 SKPM surface potential distribution of SH-P500.

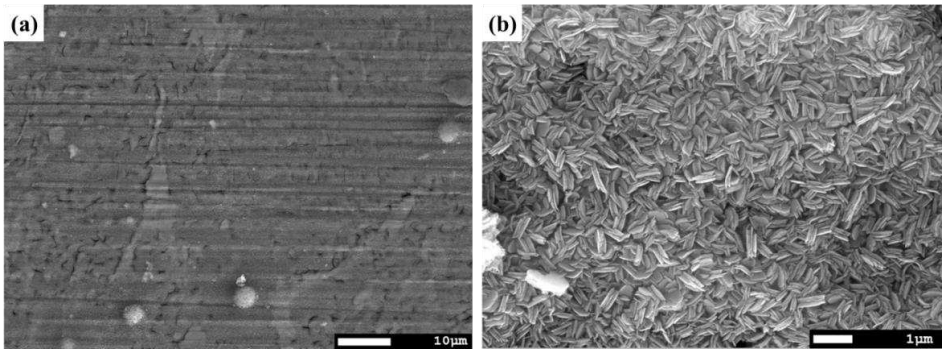

Figure 4. 54 (a, b) SEM images of SH-P500 after the corrosion tests in 3.5 wt.% NaCl solution with corrosion products.

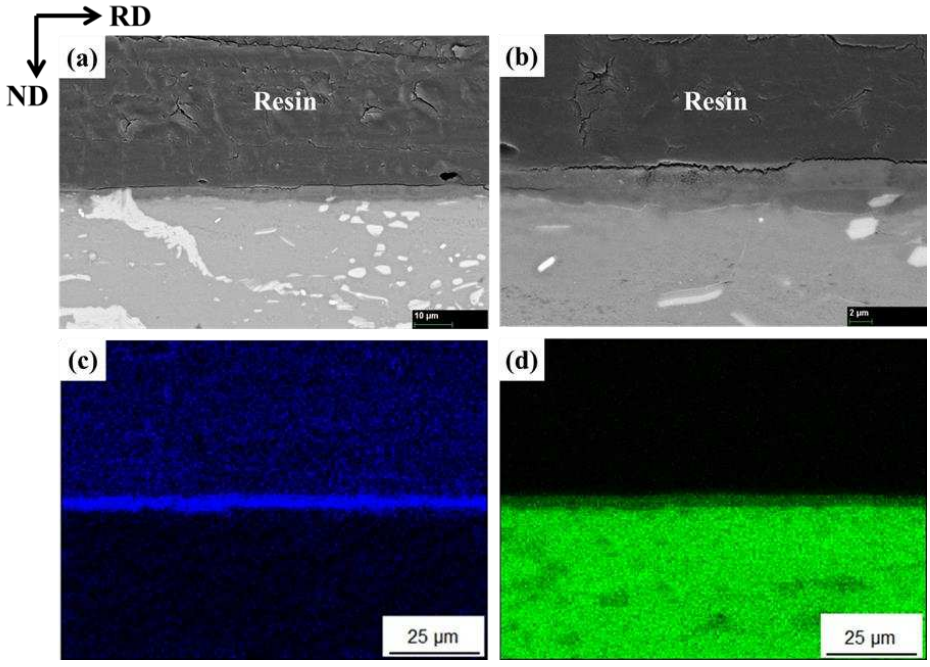

Figure 4. 55 (a, b) SEM-BSE cross sectional images of SH-P500 after the immersion in 3.5 wt. % NaCl solution and EDS elemental mapping of (c) oxygen and (d) magnesium.

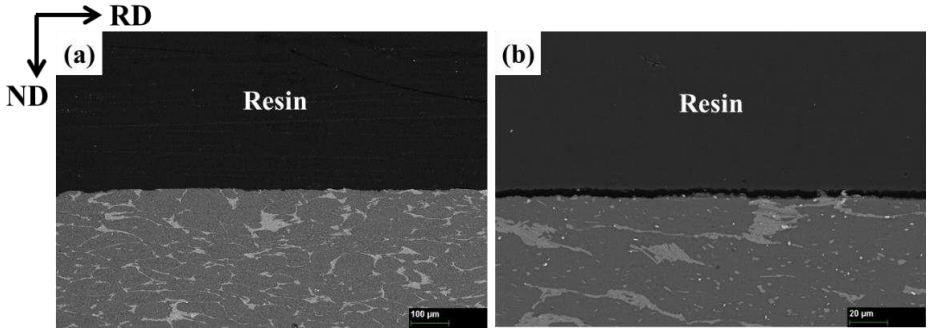

Figure 4. 56 (a, b) SEM-BSE cross sectional images of SH-P500 after the immersion in 3.5 wt. % NaCl solution after removing corrosion products.

protection from corrosive environment. The SEM images after removing the corrosion products are shown in Fig. 4.57. After 1 hr of immersion (Fig. 4.57 (a,b)), it can be seen that the corrosion is initiating around the bulk precipitates as well as the lamellar region. There was no sign of aggressive pitting corrosion unlike the homogenized and hot-rolled samples. When the immersion time reaches 3 hr, the sample reveals its unique corrosion morphology (Fig. 4.57 (c,d)). It seems that the corrosion proceeds along the Y/Zn rich lamellar leaving a thin layered structure. This is also visible from the samples after 10 hr of immersion, in which the sample surface remains relatively smooth compared to the homogenized samples (Fig. 4.57 (d,f)). The sample also showed different corrosion morphologies leaving crater-like or lamellar trace depending on the oriented direction of the lamellar phase.

From the observation, the superior corrosion resistance of the solution heat-treated samples is attributed to the formation of dense oxide/hydroxide film on the surface. It is apparent that such films would provide a better protection from the solution compared to the loose porous layer observed in homogenized samples. The better protection of the films can be also confirmed from the EIS data in which the SH-P500 and SH-P500A350 showed much higher charge transfer resistance than the P500 and P500350. It is believed that the formation of the stable protective layer is related to more homogeneous distribution of Y/Zn rich phases that consists the lamellar structure inside the grains.

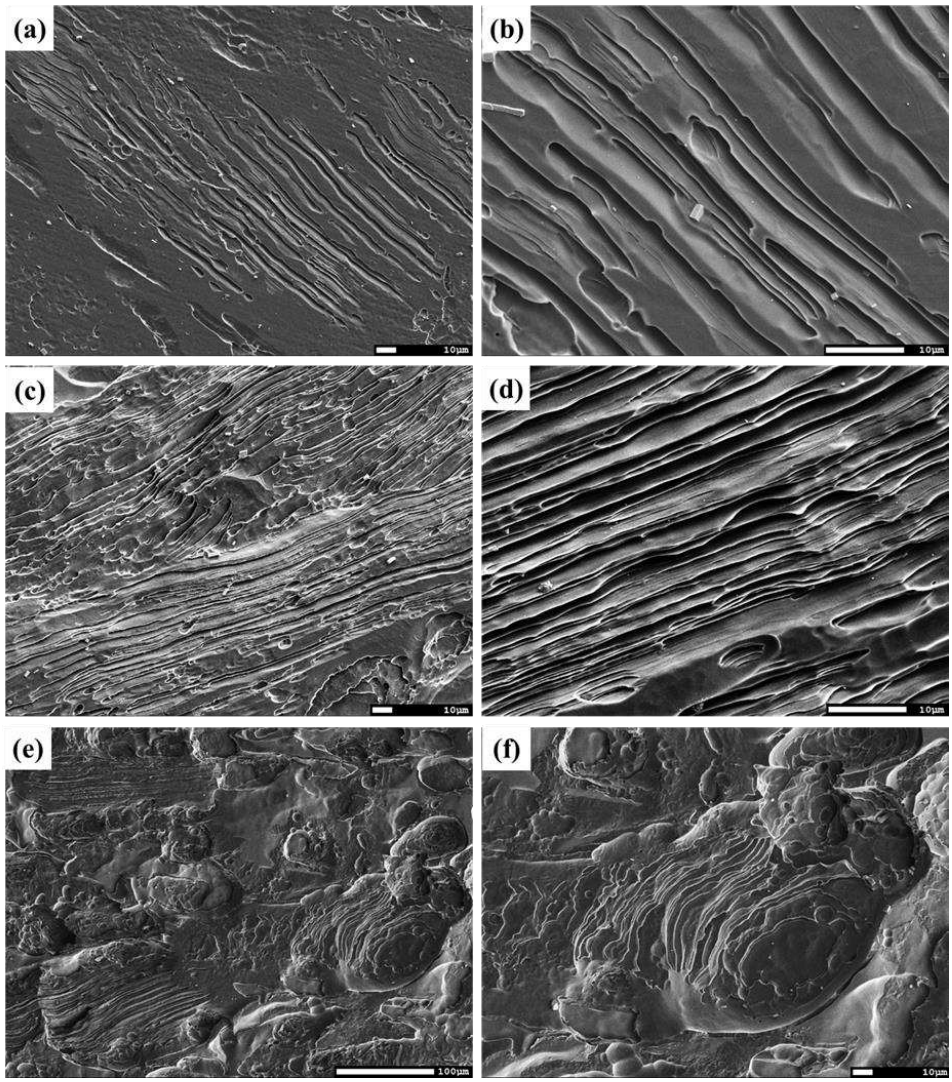

Figure 4. 57 SEM surface images of SH-P500 after (a) 1 hr, (b) 3 hr and (c) 10 hr of immersion in 3.5 wt. % NaCl solution without corrosion products.

Chapter 5

Data Analysis

The mechanical and corrosion properties of solution treated and hot-rolled strips were compared with the literature to see the position of TRC cast Mg-2Y-1Zn alloy. Also, the same experimental procedure was carried out for a gravity cast Mg-2Y-1Zn alloy to find the feasibility of the study.

5.1 Comparison with gravity cast alloy

Fig. 5.1 shows the as-cast microstructure of the gravity cast (GC) Mg-2Y-1Zn (at. %) alloy. The grain size ranged roughly from 200 μm and up to 1 mm. The cast alloy had typical dendritic structure common to Mg alloy ingots. The intermetallic phase was identified to be the $Mg_{12}YZn$ phase by the SEM-EDS (Fig. 5.2). The solution heat-treated microstructure of the gravity cast alloy is shown in Fig. 5.3. The grain size remains almost unchanged while the lamellar phase can be observed across the grains that were oriented according to the crystallographic orientation of the grains similar to the TRC cast and solution treated alloy. However, in case of the gravity cast alloy, the original inter-dendritic $Mg_{12}YZn$ phase is still visible which suggests that the transformation into the lamellar phase is still not complete. This is possibly related to the as-cast dendrite structures of the two alloys. The TRC cast alloy had much finer intermetallic phase compared to the GC cast alloy, and the transformation into the lamellar phase required shorter time. The hot-rolled microstructure (Fig. 5.4) shows elongated lamellar structure broken down into smaller clusters of lamellae. Recrystallized grains were observed near the deformed inter-dendritic phase and in the absence of the lamellae. Also, the lamellae observed

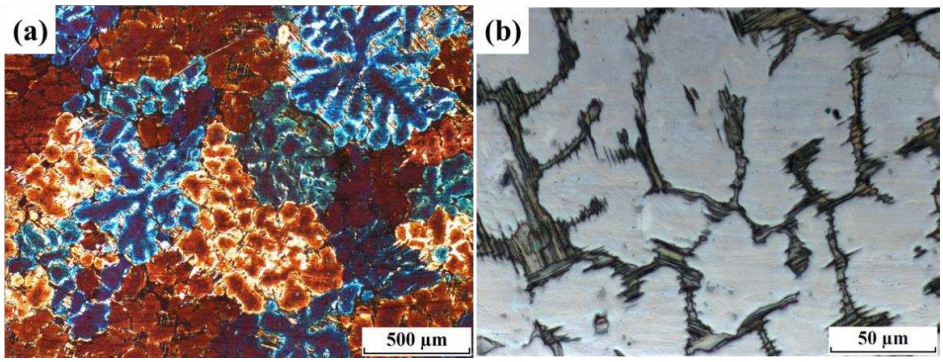

Figure 5. 1 (a), (b) Optical micrographs of as-GC Mg-2Y-1Zn alloy.

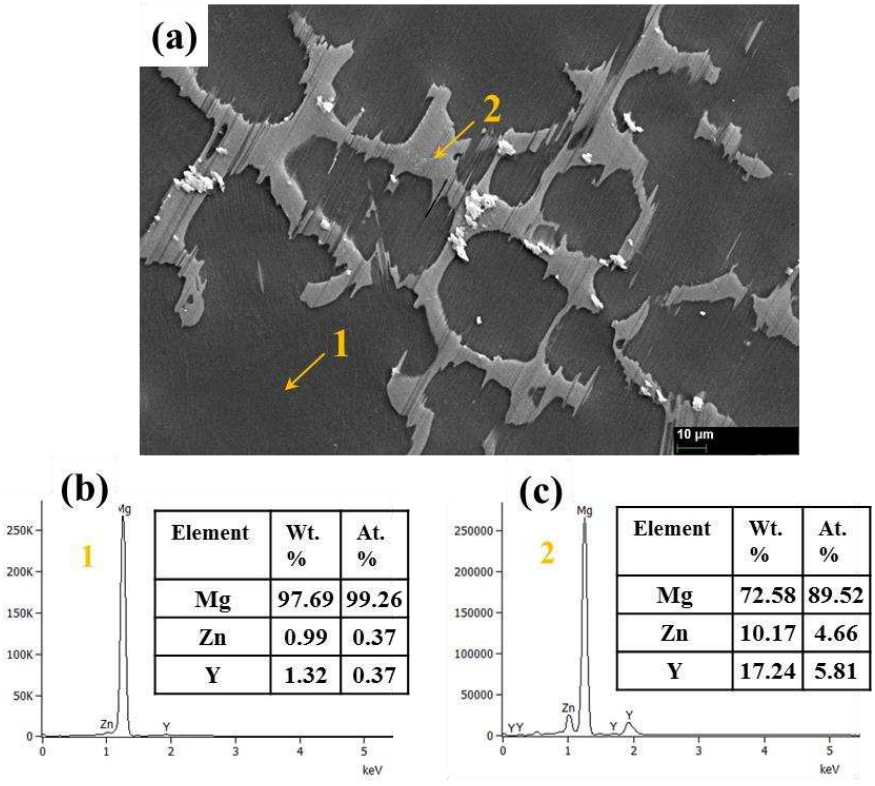

Element	Wt. %	At. %
Mg	97.69	99.26
Zn	0.99	0.37
Y	1.32	0.37

Element	Wt. %	At. %
Mg	72.58	89.52
Zn	10.17	4.66
Y	17.24	5.81

Figure 5. 2 (a) SEM micrograph of as-GC alloy and (b, c) corresponding EDS point analysis.

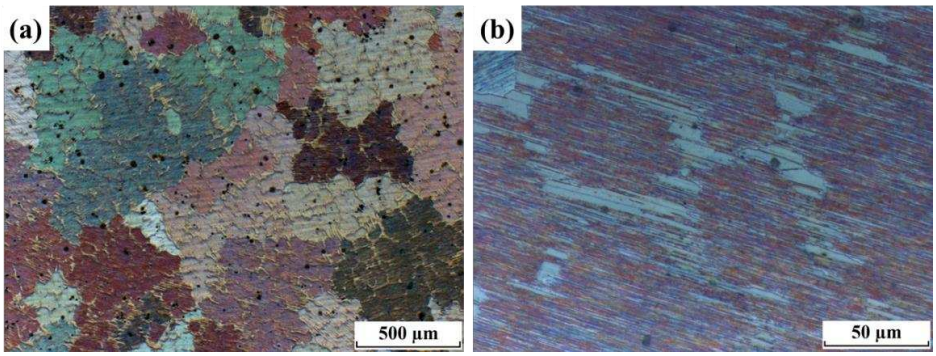

Figure 5. 3 (a), (b) Optical micrographs of GC and solution heat-treated (SH) alloy.

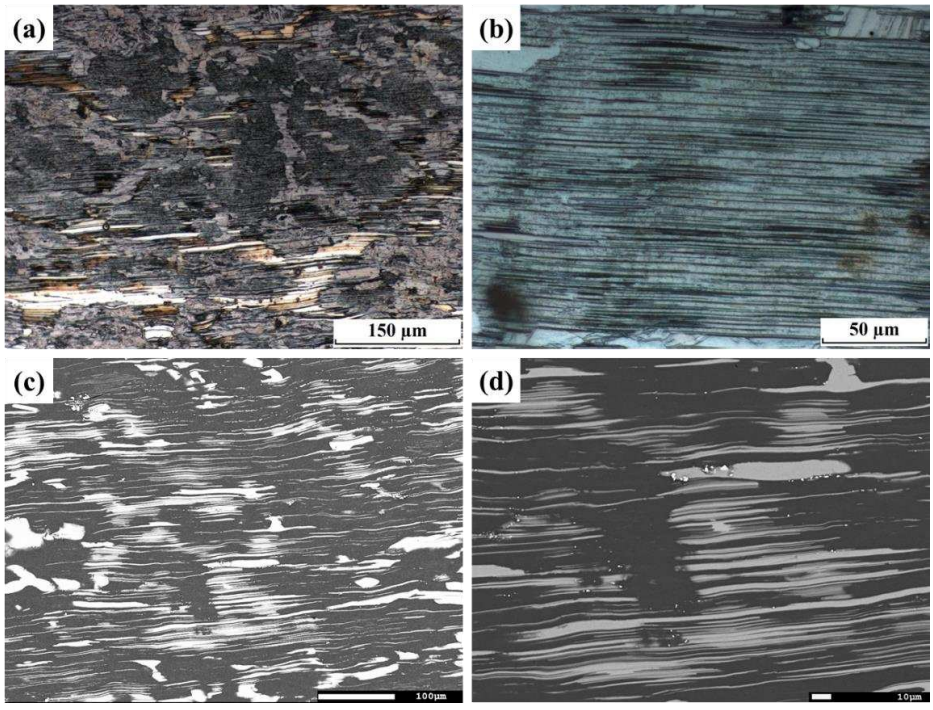

Figure 5. 4 (a, b) Optical micrographs and (c, d) SEM-BSE images of solution heat-treated and hot-rolled GC alloy (GC-SH-P500).

in GC sample seems to be thicker and coarser compared to the TRC sample as can be seen from Fig. 5.4 (c, d).

The stress-strain curve of the as-rolled GC cast alloy (GC-SH-P500) is plotted in Fig. 5.5 along with the curve of as-rolled TRC cast alloy (TRC-SH-P500) for comparison. It can be seen that the GC alloy fails in a very brittle manner and shows lower YS. This is attributed to the pores and other casting defects seen from the GC alloy prior to the hot-rolling which caused early failure. Another reason could be the smaller clusters of lamellar phase in TRC alloy which indicates that TRC alloy has smaller grain size overall even after the hot-rolling due to the finer initial microstructure.

The polarization behavior of the as-rolled GC alloy (GC-SH-P500) is shown in Fig. 5.6 along with the as-rolled TRC alloy and the electrochemical properties are summarized in Table 20. The measured OCP of the two alloys were close to each other indicating similar corrosion susceptibility. However, the E_{corr} value turned out to be quite different from the polarization test. There was a large shift in cathodic branch and more active cathodic reaction of the GC sample resulted in higher E_{corr} as well as the i_{corr} which suggests that the GC alloy has higher corrosion rate. The difference between the two alloys are also visible from the EIS spectra (Fig. 5.7). The shape of the semicircles closely resemble each other but the TRC sample shows larger semicircle in mid-high frequency range indicating better corrosion resistance which is also shown as the R_{ct} value from the fitted data in Table 21. The higher R_{ct} value of TRC sample implies lower dissolution rate of the electrode and better protective ability of the film.

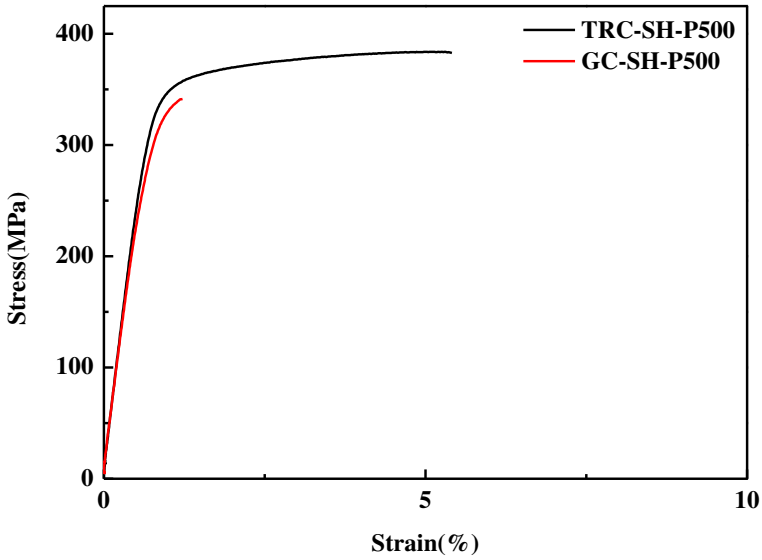

Figure 5. 5 Stress-strain curves of TRC-SH-P500 and GC-SH-P500.

Table 20 Tensile properties of TRC-SH-P500 and GC-SH-P500.

Identifier	Y.S. (Mpa)	U.T.S. (MPa)	Elong. (%)	U.E. (%)	S.H.E. n
TRC-SH-P500	338.1	383.8	4.6	4.3	0.083
GC-SH-P500	312.8	340.8	-	0.5	0.242

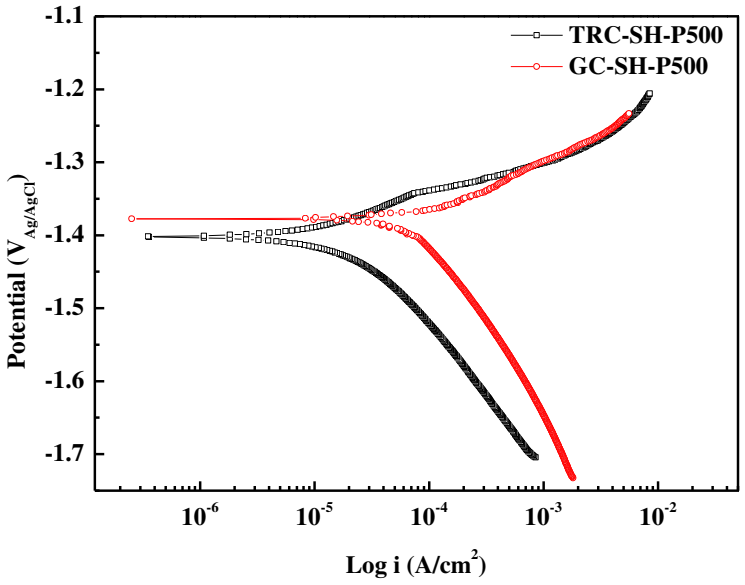

Figure 5. 6 Polarization curves of TRC-SH-P500 and GC-SH-P500.

Table 21 Electrochemical properties of TRC-SH-P500 and GC-SH-P500.

Identifier	OCP ($V_{Ag/AgCl}$)	i_{corr} (A/cm^2)	E_{corr} ($V_{Ag/AgCl}$)	b_c (mV)	Pi (mm/year)
TRC-SH-P500	-1.485	24.364	-1.400	207.55	0.56
GC-SH-P500	-1.491	162.736	-1.378	280.25	3.70

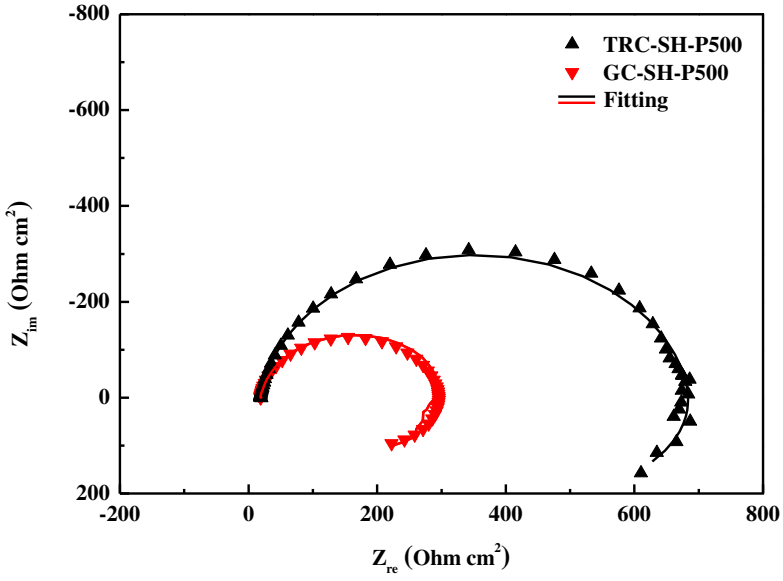

Figure 5. 7 EIS spectra of TRC-SH-P500 and GC-SH-P500 in 3.5 wt.% NaCl.

Table 22 Fitted EIS spectra for TRC-SH-P500 and GC-SH-P500.

Identifier	R_S ($\Omega \cdot cm^2$)	CPE_{dl}		R_{ct} ($\Omega \cdot cm^2$)	L ($H \cdot cm^2$)	R_L ($\Omega \cdot cm^2$)
		Y_{dl} ($\mu\Omega^{-1} \cdot cm^{-2} \cdot s^{-1}$)	n_{dl}			
TRC-SH-P500	18.31	14.15	0.94	672.8	5129	539.8
GC-SH-P500	18.72	26.82	0.94	278.2	850.4	114.6

The hydrogen evolution of GC-SH-P500 and TRC-SH-P500 in 3.5 wt.% NaCl saturated with $Mg(OH)_2$ are shown in Fig. 5.8, and the calculated corrosion rates based on evolved hydrogen and weight loss are summarized in Table 22. The result of immersion tests also agrees with the electrochemical tests and the TRC samples showed much better corrosion resistance.

Fig. 5.9 shows the corrosion morphologies of GC samples after removing the corrosion products. Similar to the TRC samples, the corrosion propagation along the lamellae phase can be identified after 1 hr of immersion due to the galvanic corrosion. After 10 hr of immersion, it can be seen that the corrosion progression is different depending on the location. The sample shows relatively uniform corrosion across the oriented lamellar structure but it seems that the inter-dendritic phase within the lamellar is corroded preferentially (Fig. 5.9 (d)). Also, the lamellae showed different corrosion rate depending on its orientation as can be seen from Fig. 5.9 (e). The higher corrosion rate in GC sample could be attributed to the large clusters of lamellae and the inter-dendritic phase within the lamellae that led to less homogeneous structure and surface film formation. Another possible reason could be the coarser lamellae in GC sample which caused less uniform corrosion and showed rough morphology compared to the TRC sample as can be seen from Fig. 5.10.

Overall, the TRC cast and hot-rolled Mg-2Y-1Zn showed better mechanical properties and corrosion resistance owing to the fine lamellar structure. It was found that the alloy can be cast more efficiently and also requires less time for the preferred microstructure

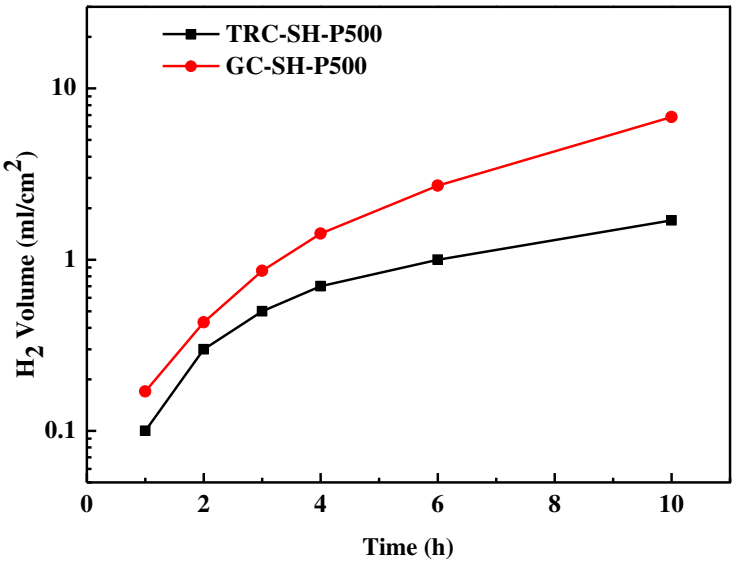

Figure 5. 8 Hydrogen evolution of TRC-SH-P500 and GC-SH-P500 in 3.5 wt.% NaCl.

Table 23 Calculated corrosion rates of TRC-SH-P500 and GC-SH-P500 in 3.5 wt.% NaCl.

Identifier	Corrosion rate (mm/year)	
	P_W	P_H
TRC-SH-P500	3.02	2.73
GC-SH-P500	42.11	38.04

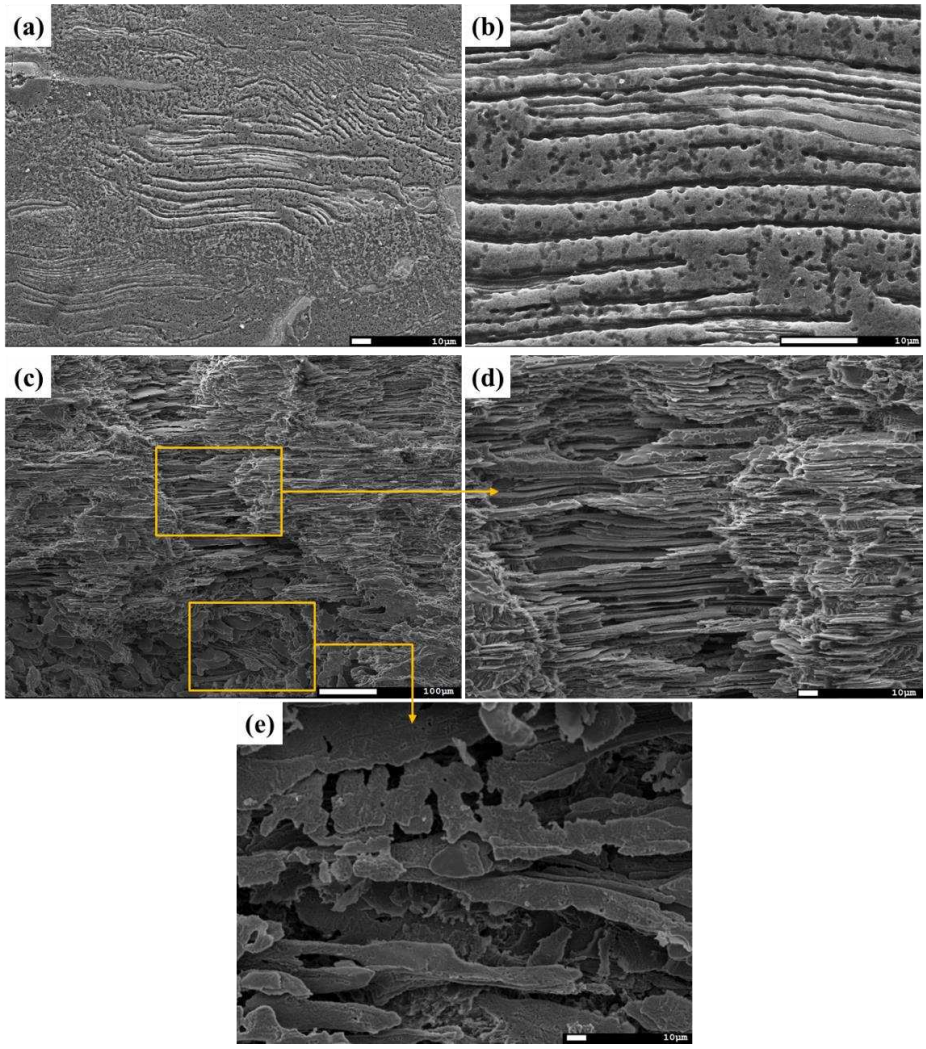

Figure 5. 9 SEM corrosion morphologies of GC-SH-P500 after (a, b) 1 hr and (c, d, e) 10 hr of immersion in 3.5 wt.% NaCl solution.

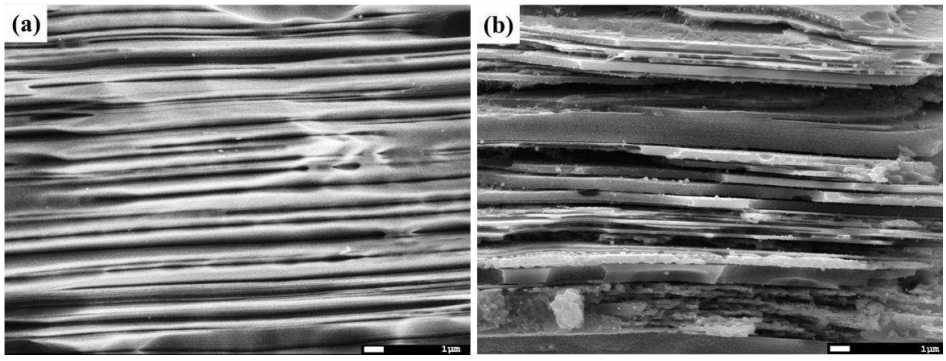

Figure 5. 10 SEM corrosion morphologies at the lamellae of (a) TRC-SH-P500 and (b) GC-SH-P500 after 10 hr immersion in 3.5 wt.% NaCl solution.

5.2 Comparison with the literature

The mechanical properties of studied alloy are compared with other LPSO alloys from the literature and listed in Table 24. It shows that the mechanical properties of TRC cast and hot-rolled Mg-2Y-1Zn (at. %) alloy are comparable to or better than the properties of Mg-2Y-1Zn alloy and other LPSO types of alloys that has been ingot cast and extruded. Moreover, the TRC cast and hot-rolled Mg-2Y-1Zn showed even better properties than the alloys that contain more rare-earth elements. These values suggest that an alloy with better mechanical properties can be produced more efficiently and economically by combining TRC and subsequent hot-rolling.

The position of yield strength and corrosion rate of the TRC cast as well as the hot-rolled Mg-2Y-1Zn alloys are compared with several LPSO type alloys and industrial Mg alloys and illustrated in Fig. 5.12. It can be seen that the TRC cast Mg-2Y-1Zn has better yield strength at the expense of corrosion rate compared to other ingot cast LPSO types of alloys. Once the alloy is hot-rolled, the corrosion rate drops to a reasonable level and shows a good combination strength and corrosion rate that are better than commercial Mg alloys processed by extrusion and ECAP. However, it should be noted that various corrosion mediums are used for these studies and the corrosion rate significantly depends on corrosion medium.

Table 24 Mechanical properties of selected LPSO type alloys.

Alloy (wt. %)	Y.S. (Mpa)	U.T.S. (Mpa)	Elong. (%)	Process	Reference
Mg-2Y-1Zn (at. %)	230	350	11	Extrusion	23
	285	390	15	Extrusion + ECAP	
Mg-2Y-1Zn (at. %)	-	320	11.2	Extrusion	24
Mg-6RY-4Zn (RY: Y rich MM)	216	327	10.9	Extrusion	25
	245	340	10.6	Extrusion + aging	
Mg-9RY-4Zn (RY: Y rich MM)	265	353	9.7	Extrusion	
	285	376	8.6	Extrusion + aging	
Mg-2.5Y-2.5Zn-1.6Ti-0.3Zr (at. %)	320	385	12	Extrusion	26
Mg-9Y-3Zn	-	303	-	Extrusion	27
Mg-9Y-3Zn-1Mn	237	320	11.5	Extrusion	28
Mg-9Y-3Zn-0.5Zr	-	340	16.2	Extrusion	29
Mg-7Y-5Sm-0.3Zr-0.5Zn	250	358	18.5	Extrusion	30
Mg-4.7Gd-3.4Y-1.2Zn-0.5Zr	255	322	-	Extrusion	31
Mg-6Gd-4Y-1Zn	232	342	7.4	Extrusion	32
Mg-6Gd-4Y-2Zn	208	329	5.7	Extrusion	
Mg-12Gd-2Er-1Zn-0.6Zr	243	344	13.4	Extrusion	33
Mg-8.2Gd-3.8Y-1.0Zn-0.4Zr	228	323	8.6	Extrusion	34
Mg-12Dy-1.1Ni	275	336	13.7	Extrusion	35
Mg-2Y-1Zn (at. %)	340	384	4.6	Hot-rolling	This study

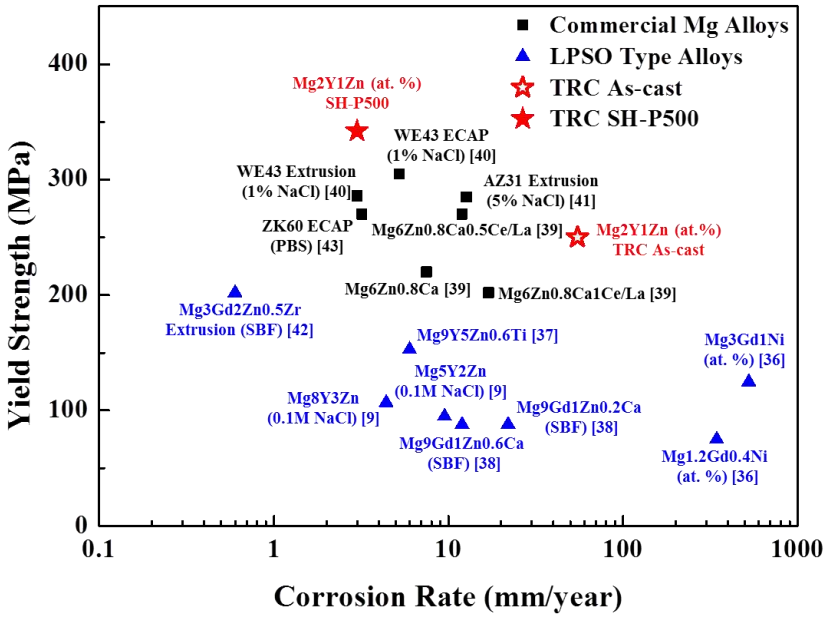

Figure 5. 11 Yield strength vs. corrosion rate of selected Mg alloys.

Chapter 6

Conclusion

The Mg-2Y-1Zn (at. %) alloy was cast by horizontal twin-roll strip casting (TRC) with different casting speeds (2.6, 3.3, 4.0, 4.7 m/min). The as-cast strips showed different surface appearance, mechanical properties, and corrosion properties according to the casting speeds. The main reason for different properties between the strips were their microstructure, degree of deformation and external/internal defects. The higher casting speed led to faster cooling and finer deformed microstructure, which resulted in better mechanical properties of the as-cast strip. On the other hand, the fine dendritic structure of the high-speed cast samples caused lower corrosion resistance on the surface due to the increased area for the galvanic reaction.

The strips hot-rolled at preheating temperatures of 400, 450, 500 ^{o}C showed different mechanical and corrosion behavior. The samples cast at lower speed exhibited better mechanical properties after the hot-rolling, which is most likely attributed to the high level of total reduction rate. The higher preheating temperature also led to higher strength due to solid solution strengthening and quasi-continuous second phase distribution resulting from the dissolution of precipitates. The strip cast at lower temperature had better corrosion resistance even after the hot-rolling although in general the corrosion rates were extremely high (~840.5 mm/year). The effect of pre-heating temperature was more significant also in terms of corrosion properties. The dissolved second phase during high temperature rolling resulted in reduced interface between the precipitates and the alpha which suppressed the galvanic corrosion.

The annealing temperatures (350, 500, 550 ^{o}C) of the hot-rolled strips also had a huge impact on alloy characteristics. The alloys retained reasonable strength up to the annealing temperature of 350 ^{o}C with improved ductility. Only partial recovery and recrystallization occurred at this temperature. The corrosion resistance was improved especially in the case of the samples hot-rolled with lower preheating temperatures, as the samples no longer showed exfoliation-type of corrosion due to the resolved internal stress. The increase in annealing temperature resulted in further decrease in strength but improved corrosion resistance. At the annealing temperature of 550 ^{o}C, the corrosion resistance was greatly improved to ~9.1 mm/year by the complete dissolution of the $Mg_{12}YZn$.

Hot-rolling of solution heat-treated strips was also attempted. The hot-rolled sheet comprised of bulk Mg12YZn, lamellar LPSO phase, and the α-Mg. This process yielded similar mechanical properties before and after the annealing but the corrosion resistance was significantly improved (3.02 mm/year). The main reason for the improved corrosion resistance was mainly due to the dense protective films formed on the surface.

The TRC cast and hot-rolled Mg-2Y-1Zn showed better overall properties than the gravity cast and hot-rolled alloy which indicates that the combination of TRC and hot-rolling is more industrially viable way of producing Mg-2Y-1Zn. The better mechanical and corrosion resistance compared to other commercial Mg alloys also suggests the possibility as a future structural material.

In regards of twin-roll casting, controlling the process parameters such as roll separation force, melt temperature, roll gap, casting speed is of great

importance in determining the quality of cast strips. In this study, only the change in casting speed was considered which influenced the mechanical and corrosion properties of the as-cast strips to a certain degree. Modifying other parameters could lead to even more change in as-cast property. However, the effect of casting speeds gradually diminished as the strips were further processed through hot-rolling and annealing. Therefore, it might be worth paying attention to the post-casting parameters in the future study. The idea is to develop optimal processing parameters through more systematically designed procedure with deeper understanding of the strengthening mechanism of the alloy as well as the corrosion mechanism. Up to this point, the reason for improved corrosion resistance in solution heat-treated samples is still not fully understood. The future study will involve deeper analysis on the strengthening mechanism and the corrosion principle of the alloy.

References

[1] Y. Kawamura, M. Yamasaki, “Formation and Mechanical Properties of Mg97Zn1RE2 Alloys with Long-Period Stacking Ordered Structure”, Materials Transactions, 48(2007), 2986-2992.

[2] T. Matsushita, K. Nakayama, H. Fukase, S. Osada, “Development and Commercialization of Twin Roll Strip Caster”, IHI Engineering Review, 42(2009), 1-9

[3] Y. Kawamura, K. Hayashi, A. Inoue, T. Masumoto, “Rapidly solidified powder metallurgy $Mg_{97}Zn_1Y_2$ alloys with excellent tensile yield strength above 600 MPa”, Materials Transactions, 42(2001), 1172-1176

[4] Y. Liu, D. Liu, C. You, M. Chen, “Effects of grain size on the corrosion resistance of pure magnesium by cooling rate controlled solidification”, Frontiers of Materials Science, 9(2015), 247-253

[5] Y. Jang, S. Kim, C. Yim, C. Lee, S. Kim, “Corrosion behavior of friction stir welded AZ31B Mg in 3.5% NaCl solution”, Corrosion Engineering, Science and Technology, 42(2007), 119-122

[6] D. Song, A. Ma, J. Jiang, P. Lin, D. Yang, J. Fan, “Corrosion behavior of equal-channel angular-pressed pure magnesium in NaCl aqueous solution”, Corrosion Science, 52(2010), 481-491

[7] N. Saikrishna, G. Kumar Reddy, B. Munirathinam, B. Ratna Sunil, “Influence of bimodal grain size distribution on the corrosion behavior of friction stir processed biodegradable AZ31 magnesium alloy”, Journal of Magnesium and Alloys, 4(2016), 68-76

[8] J. Zhang, J. Xu, W. Cheng, C. Chen, J. Kang, “Corrosion Behavior of Mg-Zn-Y Alloy with Long-period Stacking ordered Structures”, Journal of Materials Science and Technology, 28(2012), 1157-1162

[9] C. Li, D. Xu. Z. Zeng, B. Wang. L. Sheng, X. Chen, E. Han, “Effect of volume fraction of LPSO phases on corrosion and mechanical properties of Mg-Zn-Y alloys”, Materials & Design, 151(2017), 430-441

[10] W. Yuan, Z. Zhang, Y. Su, L. Qiao, W. Chu, “Influence of specimen thickness with rectangular cross-section on the tensile properties of structural steels”, Materials Science and Engineering A, 532(2012), 601-605

[11] J. Robson, “Effect of Rare-Earth Additions on the Texture of Wrought Magnesium Alloys: The Role of Grain Boundary Segregation”, Metallurgical and Materials Transactions A, 45(2014), 3205-3212

[12] H. Liu, J. Bai, K. Yan, J. Yan, A. Ma, J. Jiang, “Comparative studies on evolution behaviors of 14H LPSO precipitates in as-cast and as-extruded Mg-Y-Zn alloys during annealing at 773K”, Materials & Design, 93(2016), 9-18

[13] Y. Fukuda, M. Noda, T. Ito, K. Suzuki, N. Saito, Y. Chino, “Effect of Reduction in Thickness and Rolling Conditions on Mechanical Properties and Microstructure of Rolled Mg-8Al-1Zn-1Ca Alloy”, (2017), 1-9

[14] M. Noda, Y. Kawamura, “Thermal stability and Mechanical Properties of Extruded Mg-Zn-Y Alloys with Long-Period Stacking Order Phase”, Materials Science Forum, 653-656(2010), 611-614

[15] Z. Su, R. Li, J. An, Y. Lu, “Effect of Rolling Temperature on the Microstructures and Mechanical Properties of Mg97Zn1Y2 Magnesium Alloy”,

Journal of Materials Engineering and Performance, 19(2010), 70-76

[16] M. Yang. F. Pan, J. Shem, Y. Zhu, C. Qin, “Comparison about as-cast microstructures and mechanical properties of Mg-4Y-12Mn-0.9Sc and Mg-4Y-1.2Mn-1Zn (wt%) magnesium alloys”, Journal of Materials Science, 46(2011), 3094-3100

[17] Y. Zheng, “Magnesium Alloys as Degradable Biomaterials”, (2016)

[18] V. Sinyavskii, V. Kalinin, V. Gladyshev, Y. Yakimove, “Exfoliation co8rosion of aluminum alloys and their protection by coatings with metal-filled primers”, Protection of Metals, 41(2005), 36-46

[19] A. Makhlouf, “Intelligent Coatings for Corrosion Control”, (2015)

[20] T. Morishige, H. Doi, T. Goto, E. Nakamura, T. Takenaka, “Exfoliation Corrosion Behavior of Cold-Rolled Mg-14 mass% Li-1 mass% Al Alloy in NaCl Solution”, Materials Transactions, 54(2013), 1863-1866

[21] D. Xu, E. Han, Y. Xu, “Effect of long-period stacking ordered phase on microstructure, mechanical property and corrosion resistance of Mg alloys: A review”, 26(2016), 117-128

[22] C. Xu, T. Nakata, X. Qiao, M. Zheng, K. Wu, S. Kamado, “Effect of LPSO and SFs on microstructure evolution and mechanical properties of Mg-Gd-Y-Zn-Zr alloy”, Scientific Reports, 40846(2017)

[23] K. Yan, J. Sun, H. Liu, H. Cheng, J. Bai, X. Huang, “Exceptional mechanical properties of an $Mg_{97}Y_2Zn_1$ alloy wire strengthened by dispersive LPSO particle clusters”, Materials Letters, 242(2019), 87-90

[24] H. Liu, E. Xue, J. Bai, J. Zhou, Y. Sun, “Microstructures and Mechanical Properties of Mg-2Y-xZn (x=1,2,3 at%) Alloys, Rare Metal Materials and Engineering, 43(2014), 570-574

[25] Z. Leng, J. Zhang, T. Zhu, R. Wu, M. Zhang, S. Liu, J. Sun, L. Zhang, “Microstructure and mechanical properties of Mg-(6,9)RY-4Zn alloys by extrusion and aging”, Materials & Design, 52(2013), 713-719

[26] S. Wu, Z. Zhang, J. Zhang, C. Xu, X. Niu, W. Liu, “Effects of Phase Content and Evolution on the Mechanical Properties of Mg95Y2.5Zn2.5 and Mg93.1Y2.5Zn2.5Ti1.6Zr0.3 Alloys Containing LPSO and W Phases”, ADVANCED ENGINEERING MATERIALS, 19(2017)

[27] Y. Guo, Y. Wang, M. Zhang, Y. Zhang, D. Fang, Y. Wei, B. Liu, “Microstructure and mechanical behavior of Mg-Y-Zn alloys with respect to varying content of LPSO phase”, International Journal of MATERIALS RESEARCH, 109(2018), 944-950

[28] X. Zhang, Z. Wang, Y. Jiang, G. Sun, Z. Jiang, C. Che, G. Bi, J. Liu, W. Wang, D. Fang, “Strain Rate Dependence of Tensile Properties of Extruded Mg-9Y-3Zn-1Mn Alloy”, ADVANCED ENGINEERING MATERIALS, 20(2018), 1800123

[29] Q. Li, F. Ye, H. Zhou, J. Zhong, Z. Zhao, M. Wang, “Hot deformation behavior of Mg-9Y-3Zn-0.5Zr alloy”, Chinese Journal of Nonferrous Metals, 18(2008), 2012-1019

[30] S. Lyu, W. Xiao, G. Li, R. Zheng, C. Ma, “Achieving enhanced mechanical properties in Mg-Y-Sm-Zr alloy by altering precipitation behaviors

through Zn addition", MAEA, 746(2019), 179-186

[31] T. Chen, Z. Chen, J. Shao, R. Wang, L. Mao, C. Liu, "The role of long-period stacking ordered phases in the deformation behavior of a strong textured Mg-Zn-Gd-Y-Zr alloy sheet processed by hot-extrusion", 750(2019), 31-39

[32] R. Zhen, Y. Sun, X. Shen, Z. Ba, "Microstructures and Mechanical Properties of Mg-6gd-4y-xZn Alloys reinforced with LPSO Phases", Chinese Journal of Materials Research, 32(2018), 439-448

[33] K. Wen, K. Liu, Z. Wang, S. Li, W. Du, "Effect of microstructure evolution on mechanical property of extruded Mg-12Gd-2Er-1Zn-0.6Zr alloys", Journal of Magnesium and Alloys, 3(2015), 23-28

[34] C. Xu, M. Zheng, K. Wu, E. Wang, G. Fan, S. Xu, S. Kamado, X. Liu, G. Wang, X. Lv, "Influence of rolling temperature on the microstructure and mechanical properties of Mg-Gd-Y-Zn-Zr alloy sheets", MSEA, 559(2013), 615-622

[35] G. Bi, Y. Han, J. Jiang, Y. Li, D. Zhang, D. Qiu, M. Easton, "Microstructure and mechanical properties of an extruded Mg-Dy-Ni alloy", Materials Science and Engineering, 760(2019), 246-257

[36] Z. Han, K. Zhang, J. yang, R. Wei, C. Zhang, "Effects of volume fraction of Ni-containing LPSO phase on mechanical and corrosion properties of Mg-Gd-Ni alloys", Materials and Corrosion, 70(2019), 537-548

[37] P. Cheng, Y. Zhao, R. Lu, H. Hou, "Effect of the morphology of long-period stacking ordered phase on mechanical properties and corrosion behavior of cast Mg-Zn-Y-Ti alloy", Journal of Alloys and Compounds, 764(2018), 226-

[38]. Zhang, J. Dai, H. Yang, S. Liu, X. He, Z. Wang, “Influence of Gd and Ca on microstructure, mechanical and corrosion properties of Mg-Gd-Zn(-Ca) alloys”, 32(2017), 399-408

[39] L. Tong, Q. Zhang, Z. Jiang, J. Zhang, J. Meng, L. Cheng, H. Zhang, “Microstructure, mechanical properties and corrosion resistance of extruded Mg-Zn-Ca-xCe/La alloys”, Journal of the Mechanical Behavior of Biomedical Materials, 62(2016), 57-70

[40] K. Kutniy, I. Papirov, M. Tikhonovsky, A. Pikalov, S. Sivtzov, L. Pirozhenko, V. Shokurov, V. Shkuropatenko, “Influence of grain size on mechanical and corrosion properties of magnesium alloy for medical implants”, Materialwissenschaft und Werkstofftechnik, 40(2009), 242-246

[41] Y. Chino, T. Hoshika, M. Mabuchi, “Mechanical and Corrosion Properties of AZ31 Magnesium Alloy Repeatedly Recycled by hot Extrusion”, Materials Transactions, 47(2006), 1040-1046

[42] H. Yao, J. Wen, Y. Xiong, Y. Lu, F. Ren, W. Cao, “Extrusion temperature impacts on biometallic Mg-2.0Zn-0.5Zr-3.0Gd (wt%) wolid-solution alloy”, Journal of Alloys and Compounds, 739(2018), 468-480

[43] E. Mostaed, M. hashempour, A. Fabrizi, D. Dellasega, M. Bestetti, F. Bonollo, M. Vedani, “Microstructure, texture evolution, mechanical properties and corrosion behavior of ECAP processed ZK60 magnesium alloy for biodegradable applications”, Journal of the Mechanical Behavior of Biomedical Materials”, 37(2014), 307-322